

IVW - Schriftenreihe Band 72

Institut für Verbundwerkstoffe GmbH - Kaiserslautern

Hui Zhang

**Fracture of Nanoparticle Filled
Polymer Composites**

Bibliografische Information Der Deutschen Bibliothek

Die Deutsche Bibliothek verzeichnet diese Publikation in der Deutschen Nationalbibliografie; detaillierte bibliografische Daten sind im Internet über <<http://dnb.ddb.de>> abrufbar.

Bibliographic information published by Die Deutsche Bibliothek

Die Deutsche Bibliothek lists this publication in the Deutsche Nationalbibliografie; detailed bibliographic data is available in the Internet at <<http://dnb.ddb.de>>.

Herausgeber: Institut für Verbundwerkstoffe GmbH
Prof. Dr.-Ing. Alois K. Schlarb
Erwin-Schrödinger-Straße
TU Kaiserslautern, Gebäude 58
67663 Kaiserslautern
<http://www.ivw.uni-kl.de>

Verlag: Institut für Verbundwerkstoffe GmbH

Druck: Technische Universität Kaiserslautern
ZBT – Abteilung Foto-Repro-Druck

D 386

© Institut für Verbundwerkstoffe GmbH, Kaiserslautern 2007

Alle Rechte vorbehalten, auch das des auszugsweisen Nachdrucks, der auszugsweisen oder vollständigen Wiedergabe (Photographie, Mikroskopie), der Speicherung in Datenverarbeitungsanlagen und das der Übersetzung.

Als Manuskript gedruckt. Printed in Germany.

ISSN 1615-021X
ISBN 978-3-934930-68-1
ISBN 3-934930-68-9

Fracture of Nanoparticle Filled Polymer Composites

Beim Fachbereich für Maschinenbau und Verfahrenstechnik
der Technischen Universität Kaiserslautern
vorgelegte Dissertation
zur Erlangung des akademischen Grades

Doktor-Ingenieur (Dr.-Ing.)

von

M.Sc. Hui Zhang

aus Beijing, China

Tag der mündlichen Prüfung: 29. Mai 2006

Prüfungsvorsitzender: Prof. Dr.-Ing. Dieter H. Hellmann

1. Berichterstatter: Prof. Dr.-Ing. Dr. h.c. Klaus Friedrich

2. Berichterstatter: Prof. Dr. Zhong Zhang

Acknowledgements

The present work was completed between June 2002 and March 2006 at the Institute for Composite Materials (IVW GmbH), Technical University of Kaiserslautern, Germany.

First and foremost, I would like to express my special gratitude to Prof. Dr.-Ing. Dr.h.c. Klaus Friedrich and Prof. Dr. Zhong Zhang for their scientific support and constant interest in my work.

I am thankful to IVW for providing me with the opportunity of working in an outstanding environment. I would like to express appreciation to IVW staff and my colleagues of Division II for their thorough and friendly help with my work. Thanks are also extended to hanse chemie AG (Germany) for the donation of materials.

I would like to thank Dr. Li Song (Institute of Physics, Chinese Academy of Sciences) for his kind assistance on SEM inspections. Many thanks also to Mr. Stefan Schmitt for his AFM work. I wish also to thank Dr. Bernd Wetzel, Dr. Patrick Rosso and Mr. Schimmele for their kind help.

This work is dedicated in love to my wife Yun Wang for her patience and understanding. Lastly, I would like to convey my special thanks to my parents who encouraged me constantly.

Table of Contents

Acknowledgements.....	I
Table of Contents.....	II
Abstract/Kurzfassung.....	VI
List of Abbreviations and Symbols.....	X
1. State of the Art.....	1
1.1 Introduction.....	1
1.2 Recent Progress in Mechanical Properties of Nanocomposites.....	3
1.2.1 Nanoparticle-filled Composites.....	3
1.2.2 Carbon-nanotube-filled Composites.....	5
1.3 Compounding Techniques for Nanocomposites.....	7
1.3.1 Sol-gel Method.....	8
1.3.2 Melt Compounding.....	8
1.3.3 Other Methods.....	9
1.4 Toughening Mechanisms of Inorganic Rigid Particles.....	10
1.4.1 Thermoplastic Matrix.....	10
1.4.2 Thermosetting Matrix.....	12
1.4.2.1 Crack Deflection.....	12
1.4.2.2 Crack Pinning and Bowing.....	13
1.4.2.3 Particle Bridging.....	14
1.4.2.4 Microcracking.....	14
1.4.2.5 Plastic Deformation.....	15

2.	Aim of this Work.....	16
3.	Experimental Procedures.....	18
3.1	Materials and Sample Preparation.....	18
3.1.1	Thermosetting Composites.....	18
3.1.2	Thermoplastic Composites.....	20
3.2	Fracture Toughness.....	21
3.2.1	K_{IC} and G_{IC} for Brittle Materials.....	22
3.2.2	Essential Work of Fracture (EWF) for Ductile Materials.....	24
3.2.2.1	Concept of EWF.....	24
3.2.2.2	Partitioning of EWF.....	26
3.2.2.3	EWF Test.....	27
3.3	Other Mechanical Properties.....	28
3.3.1	Tensile and Flexural Tests.....	28
3.3.2	Microhardness Test.....	28
3.3.3	Charpy Impact Test.....	29
3.3.4	Dynamic Mechanical Thermal Analysis.....	29
3.4	Differential Scanning Calorimetry.....	30
3.5	Microstructure Characterization.....	30
3.5.1	Scanning Electron Microscopy.....	30
3.5.2	Transmission Electron Microscopy.....	30
3.5.3	Atomic Force Microscopy.....	31
3.5.4	Laserprofilometry.....	31
4.	In situ Epoxy Nanocomposites.....	32

4.1	Cycloaliphatic Epoxy Nanocomposites.....	33
4.1.1	Microstructure.....	33
4.1.2	Dynamic Mechanical Thermal Analysis.....	34
4.1.3	Various Mechanical Properties.....	38
4.1.4	Fractography.....	40
4.1.4.1	Three-Point-Bending Samples.....	40
4.1.4.2	Impact Samples.....	44
4.1.4.3	CT Samples.....	45
4.2	Bisphenol-F Epoxy Nanocomposites.....	47
4.2.1	Microstructure.....	47
4.2.2	Dynamic Mechanical Thermal Analysis.....	47
4.2.3	Various Mechanical Properties.....	49
4.2.3.1	Tensile Test.....	49
4.2.3.2	Impact Test.....	51
4.2.3.3	Fracture Test.....	52
4.2.3.4	Brief Summary.....	55
4.2.4	Fractography.....	57
4.2.4.1	Tensile Samples.....	57
4.2.4.2	CT Samples.....	61
5.	Thermoplastic Nanocomposites.....	67
5.1	Polyamide 66 Filled with Various Nanoparticles.....	68
5.1.1	Microstructure.....	68
5.1.2	Thermal Properties.....	68

5.1.3	Essential Work of Fracture.....	70
5.1.4	Temperature Dependence of EWF Parameters.....	73
5.1.5	COD Analysis.....	75
5.1.6	Fractography.....	77
5.2	Polypropylene Filled with Nanoparticles and Carbon Nanotubes.....	82
5.2.1	Microstructure.....	82
5.2.2	Thermal Properties.....	82
5.2.3	Tensile Properties.....	83
5.2.4	Essential Work of Fracture of Nanoparticle Filled PP Composites.....	84
5.2.4.1	Fracture Behaviors.....	84
5.2.4.2	Fractography.....	87
5.2.5	Notched Impact Resistance of Nanotube Filled PP Composites.....	88
5.2.5.1	Temperature Dependent Impact Resistance.....	88
5.2.5.2	Fractography and Fracture Mechanisms.....	92
6.	Summary and Outlook.....	97
7.	Literatures.....	102
8.	List of Publications.....	117

Abstract

In recent years, nanofiller-reinforced polymer composites have attracted considerable interest from numerous researchers, since they can offer unique mechanical, electrical, optical and thermal properties compared to the conventional polymer composites filled with micron-sized particles or short fibers. With this background, the main objective of the present work was to investigate the various mechanical properties of polymer matrices filled with different inorganic rigid nanofillers, including SiO_2 , TiO_2 , Al_2O_3 and multi-walled carbon nanotubes (MWNT). Further, special attention was paid to the fracture behaviours of the polymer nanocomposites. The polymer matrices used in this work contained two types of epoxy resin (cycloaliphatic and bisphenol-F) and two types of thermoplastic polymer (polyamide 66 and isotactic polypropylene).

The epoxy-based nanocomposites (filled with nano- SiO_2) were formed *in situ* by a special sol-gel technique supplied by nanoresins AG. Excellent nanoparticle dispersion was achieved even at rather high particle loading. The almost homogeneously distributed nanoparticles can improve the elastic modulus and fracture toughness (characterized by K_{IC} and G_{IC}) simultaneously. According to dynamic mechanical and thermal analysis (DMTA), the nanosilica particles in epoxy resins possessed considerable "effective volume fraction" in comparison with their actual volume fraction, due to the presence of the interphase. Moreover, AFM and high-resolution SEM observations also suggested that the nanosilica particles were coated with a polymer layer and therefore a core-shell structure of particle-matrix was expected. Furthermore, based on SEM fractography, several toughening mechanisms were considered to be responsible for the improvement in toughness, which included crack deflection, crack pinning/bowing and plastic deformation of matrix induced by nanoparticles.

The PA66 or iPP-based nanocomposites were fabricated by a conventional melt-extrusion technique. Here, the nanofiller content was set constant as 1 vol.%.

Relatively good particle dispersion was found, though some small aggregates still existed. The elastic modulus of both PA66 and iPP was moderately improved after incorporation of the nanofillers. The fracture behaviours of these materials were characterized by an essential work fracture (EWF) approach. In the case of PA66 system, the EWF experiments were carried out over a broad temperature range (23~120 °C). It was found that the EWF parameters exhibited high temperature dependence. At most testing temperatures, a small amount of nanoparticles could produce obvious toughening effects at the cost of reduction in plastic deformation of the matrix. In light of SEM fractographs and crack opening tip (COD) analysis, the crack blunting induced by nanoparticles might be the major source of this toughening.

The fracture behaviours of PP filled with MWNTs were investigated over a broad temperature range (-196~80 °C) in terms of notched impact resistance. It was found that MWNTs could enhance the notched impact resistance of PP matrix significantly once the testing temperature was higher than the glass transition temperature (T_g) of neat PP. At the relevant temperature range, the longer the MWNTs, the better was the impact resistance. SEM observation revealed three failure modes of nanotubes: nanotube bridging, debonding/pullout and fracture. All of them would contribute to impact toughness to a degree. Moreover, the nanotube fracture was considered as the major failure mode. In addition, the smaller spherulites induced by the nanotubes would also benefit toughness.

Kurzfassung

In den letzten Jahren haben nanopartikelverstärkte polymere Verbundwerkstoffe beträchtliches Interesse vieler Wissenschaftler erweckt, denn sie bieten einzigartige mechanische, elektrische, optische und thermische Eigenschaften im Vergleich zu polymeren Verbundwerkstoffen, die mit Mikropartikeln oder Kurzfasern verstärkt sind. Vor diesem Hintergrund war es das Ziel dieser Arbeit, verschiedene mechanische Eigenschaften polymerer Matrices, die mit unterschiedlichen anorganischen, steifen Nanoteilchen gefüllt wurden, zu untersuchen. Als Nanoteilchen dienten SiO_2 , TiO_2 , Al_2O_3 und mehrwandige Nanoröhrchen aus Kohlenstoff (multi-walled carbon Nanotubes, MWNT). Überdies wurde dem Bruchverhalten der polymeren Nanokomposite besondere Aufmerksamkeit geschenkt. Die in der Arbeit verwendeten Polymermatrices waren zwei Epoxydharz-Typen (zykloaliphatisches EP und Bisphenol-F) sowie zwei Typen von Thermoplasten (Polyamid 66 bzw. isotaktisches Polypropylen).

Die auf Epoxydharz basierenden und mit nano- SiO_2 (Quarz) gefüllten Nanokomposite wurden über *in situ*-Prozesse im Sol-Gel-Verfahren hergestellt und von der Firma nanoresins AG geliefert. Eine exzellente Dispergierung der Nanopartikel wurde erreicht, selbst bei sehr hohen Füllgraden. Die fast homogen verteilten Nanopartikel konnten den Elastizitätsmodul und die Bruchzähigkeit (charakterisiert durch K_{IC} und G_{IC}) simultan verbessern. Den Ergebnissen der dynamisch-mechanischen Thermoanalyse (DMTA) zufolge, besaßen die Quarz-Nanopartikel im Epoxydharz, aufgrund von Interphasen, einen beträchtlichen "effektiven Volumenanteil" im Vergleich zu ihrem tatsächlichen, theoretischen Volumenanteil. Außerdem wiesen Untersuchungen mit dem AFM und dem hoch auflösenden Elektronenmikroskop darauf hin, dass die Quarz-Nanopartikel mit einer Polymerschicht bedeckt sind. Dies deutet auf eine Kern-Schale-Struktur von Partikel und Matrix hin. Fraktographische Untersuchungen gaben Hinweise auf Mechanismen, die verantwortlich für die Zähigkeitsverbesserungen sind, einschließlich Rissablenkung, Riss-Stop (crack pinning) und Beugung der Rissfront sowie eine von Nanopartikeln induzierte plastische Deformation der Matrix.

Die PA66- bzw. iPP-basierenden Nanokomposite wurden mit konventionellen Techniken der Schmelzextrusion hergestellt. Der Gehalt an Nanofüllstoffen wurde als konstant eingestellt und betrug 1 Vol.%. Eine relativ gute Dispergierung der Nanopartikel wurde gefunden, obwohl noch einige kleine Agglomerate vorkamen. Die Elastizitätsmoduln sowohl von PA66, als auch von iPP, zeigten sich nach Beimischung der Nanofüllstoffe mäßig verbessert. Das Bruchverhalten dieser Materialien wurde durch die Methode der „essentiellen Brucharbeit“ (essential work of fracture, EWF) charakterisiert. Im Fall des PA66-Systems wurden die Experimente innerhalb eines breiten Temperaturspektrums (23~120°C) durchgeführt. Dies ergab, dass die EWF-Parameter stark von der jeweiligen Temperatur abhängen. Bei fast allen Temperaturen bewirkte die geringe Menge an Nanopartikeln zähigkeitssteigernde Mechanismen offensichtlich auf Kosten einer Reduktion der plastischen Matrixdeformation. Im Lichte fraktographischer Analysen (REM) und von Untersuchungen der Rissöffnungsverschiebung (COD) erschien die von Nanopartikeln induzierte Rissabstumpfung (crack blunting) als maßgeblicher Ausgangspunkt der Zähigkeitssteigerung.

Das Bruchverhalten des MWNT-gefüllten PP wurde ebenfalls in einem breiten Temperaturbereich (-196~80°C) in Form der Kerbschlagzähigkeit untersucht. Dies ergab, dass MWNT's die Schlagzähigkeit der PP-Matrix deutlich erhöhen können, sobald die Prüftemperatur die Glasübergangstemperatur (T_g) des PP überschreitet. In diesem Temperaturbereich zeigte sich, dass mit wachsender Länge der MWNT's auch die Kerbschlagzähigkeit ansteigt. Basierend auf elektronenmikroskopischen Untersuchungen zeigten sich aufgrund der Nanoröhrchen drei Versagensmodi im Material präsent, z.B. die Überbrückung (nanotube bridging) der Rissfront, das Ablösen/Herausziehen (debonding/pullout) sowie der Bruch von Nanoröhrchen. All diese Mechanismen sollten zur Kerbschlagzähigkeit mehr oder weniger beitragen. Darüber hinaus wurde der Bruch von Nanoröhrchen als besonders wichtiger Versagensmodus eingestuft. Zusätzlich bewogen Nanoröhrchen das Polymer, kleinere Sphärolite auszubilden, welche die Zähigkeit des Materials ebenfalls begünstigen.

List of Abbreviations and Symbols

Abbreviation

AFM		Atomic force microscope
BDT		Brittle-to-ductile transition
COD		Crack opening displacement
CT		Compact tension
DDENT		Deeply double edge notched tensile specimen
DMTA		Dynamic mechanical thermo analyzer
DSC		Differential scanning calorimetry
ESIS		European structural integrity society
EFW		Essential work of fracture
LEFM		Linear elastic fracture mechanics
MFD		Mould filling direction
PA		Polyamide
POM		Polarized optical microscopy
PP		Polypropylene
SWNT		Single-walled nanotube
MWNT		Multi-walled nanotube
SEM		Scanning electron microscopy
TEM		Transmission electron microscopy

Symbols

BET	[m ² /g]	Specific surface area
CTE	[K ⁻¹]	Coefficient of thermal expansion

d	[nm]	Particle diameter
E	[GPa]	Young's modulus
E_f	[GPa]	Flexural modulus
E^*	[GPa]	Complex modulus
E''	[MPa]	Loss modulus
HU	[MPa]	Universal hardness
h	[μm]	indenter penetration depth
K_{IC}	[MPa·m ^{1/2}]	Critical stress intensity factor
l	[mm]	Ligament length
G_{IC}	[J/m ²]	Critical strain energy release rate
F_{max}	[N]	Maximum force
T_g	[°C]	Glass transition temperature
r_p	[μm]	Radius of plastic zone at crack tip
R_a	[nm]	Arithmetic average surface roughness
R_q	[nm]	Square root average surface roughness
t	[mm]	Thickness
T_c	[°C]	Crystallization temperature
T_m	[°C]	Melting temperature
$\tan\delta_{max}$	[1]	Maximum of mechanical loss factor
V_p	[%]	Volume fraction of particle
W	[mm]	Width
W_{ini}	[kJ]	Fracture work for crack initiation
W_{porop}	[kJ]	Fracture work for crack propagation
$w_{f,total}$	[kJ/m ²]	Specific total work of fracture
w_e	[kJ/m ²]	Specific essential work of fracture
w_p	[MJ/m ³]	Specific non-essential work of fracture

$w_{e,ini}$	[kJ/m ²]	Specific essential work of fracture related to crack initiation
$w_{p,prop}$	[MJ/m ³]	Specific non-essential work of fracture related to crack propagation
X_c	[%]	Crystallinity
β	[1]	Dimensionless shape factor
δ	[mm]	Displacement
δ_o	[μ m]	Crack opening displacement
ΔH_m	[J/g]	Specific melting heat of specimen
ΔH_m^0	[J/g]	Theoretical specific melting heat of 100% crystalline polymer
ν	[1]	Poisson's ratio
σ_{net}	[MPa]	Net section stress
ρ	[g/cm ³]	Density
σ_B	[MPa]	Ultimate tensile stress
σ_y	[MPa]	Uniaxial tensile yield stress
ϵ_B	[%]	Elongation at break
φ_e	[%]	Effective volume fraction
φ_p	[%]	Actual particle volume fraction
τ	[nm]	Interparticle distance
γ_m	[J/m ²]	Specific fracture energy

1 State of the Art

1.1 Introduction

In recent years, nanofiller reinforced polymer composites (also termed polymer nanocomposites) have attracted great scientific and technological interest owing to their exceptional physico-mechanical, thermal and other properties achieved at very low nanofiller content (<5 wt.% or <2-3 vol.%) [1]. For example, Coleman et al [2] reported recently that, with less than 1 vol.% multi-walled carbon nanotubes (MWNT), poly(vinyl alcohol) and chlorinated polypropylene achieved approximately 300-400% increases in modulus and strength, a level which cannot be reached by using conventional micron-sized short carbon fiber at similar filler content. The nanofillers are also introduced into polymers to enhance other mechanical properties, e.g., fracture toughness, impact strength, creep and fatigue behaviors, as well as wear resistance. The recent progress in understanding of the mechanical properties of polymeric nanocomposites is briefly reviewed in the following paragraphs.

In general, a nanofiller is defined as a filler having one or more dimensions of the order of 100 nm or less. In contrast, the size of traditional fillers, such as short carbon fiber, glass bead and other ceramic particles, is in the micrometer range. One of the key aspects of nanofillers is their huge surface to volume ratio. Typical values of the specific surface area can reach up to several hundreds and even as high as a thousand m^2/g [3]. As a result of the huge interfacial area, the properties of nanocomposites become dominated mainly by the interface or interphase between filler and matrix; accordingly, some unique thermal and mechanical properties can be expected. Note that the physicochemical properties of the interphase are quite distinct from those of the bulk polymer matrix because several effects (crystallization or orientation or formation of immobile polymer chain [4-6]) exist in the immediate vicinity of the filler surface. On the other hand, with increasing nanofiller content, interparticle distance is significantly reduced, as illustrated in Figure 1.1. As is evident, at a given filler content, smaller nanofillers create closer interparticle distance than larger ones. Once the interparticle distance reduces to a critical value, short-distance filler-filler interactions may occur [7,8]. Moreover, the interfacial layers around

particles may overlap each other, forming a physical three-dimensional network throughout the composites and in turn greatly affecting the material properties [1]. This point of view may be partially confirmed in the present work (see Chapter 4).

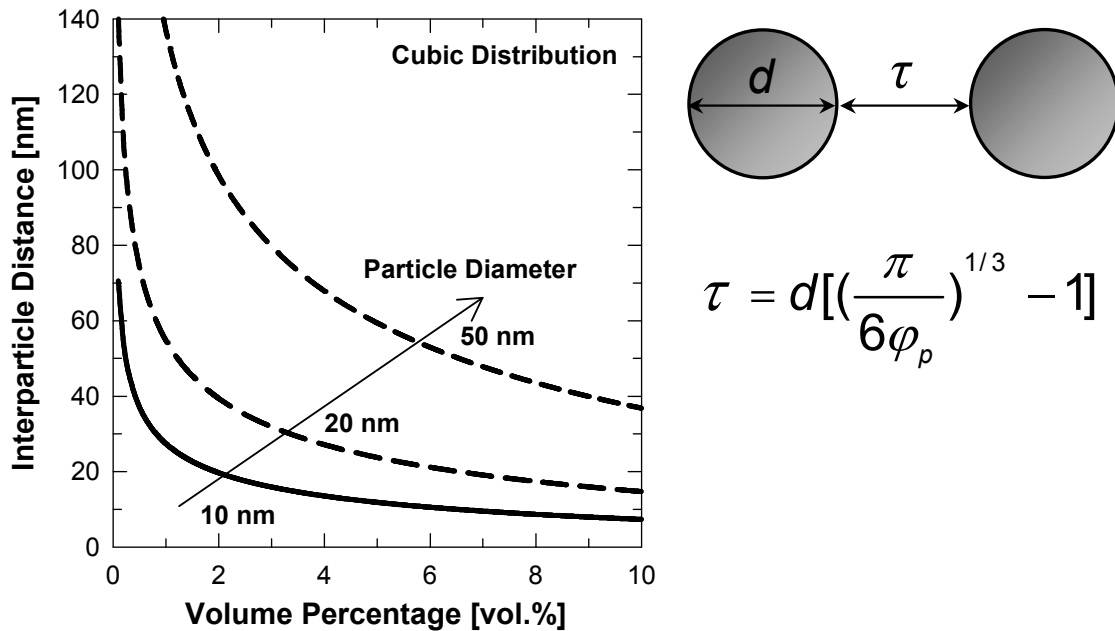


Figure 1.1: Correlation among nanofiller diameter, interparticle distance and volume percentage [1]. Based on the assumptions of cubic distribution and ideal dispersion of nanofillers, a relationship between interparticle distance, τ , and filler content, ϕ_p , can be expressed by the above equation, where d symbolizes the nanofiller diameter.

As a new class of materials, polymeric nanocomposites may potentially be manufactured at low cost and may replace traditional polymeric composites and metals in many engineering applications. The most promising example would be automotive application. It is estimated that vehicle parts made from nanocomposites (non-critical structural parts only) offer on average a 25% weight savings over highly filled plastics and as much as 80% over steel. This reduction in weight can significantly decrease energy consumption. Moreover, nanocomposites also provide stiffness, strength and reliability comparable to or better than metals. An extensive review of related aspects has recently been performed by Garcés et al [9].

1.2 Recent Progress in Mechanical Properties of Nanocomposites

This sub-section highlights recent progress in mechanical properties and the corresponding structure-property relationships of polymeric nanocomposites. First, for the purpose of discussion, we roughly group nanocomposites into three categories, based on the shape of the reinforcement materials: quasi-spherical nanoparticles (e.g. ceramic nanoparticles), fibrous materials (e.g. nanotubes) and layered materials (e.g. nanoclay) [10]. Particular attention is given to the nanoparticle-filled and carbon-nanotube-filled polymer composites, since they are related to the materials studied in this thesis. As regards polymer-layered silicate nanocomposites, some related research work can be found in reference [11].

1.2.1 Nanoparticle-filled Composites

Quasi-spherical nanoparticles (i.e. their aspect ratio is close to unit) are widely used in polymeric nanocomposites to enhance the mechanical and other properties of polymer composites. Commonly used nanoparticles include carbon black, nanosilica (SiO_2), nanoalumina (Al_2O_3), nanotitania (TiO_2), nano-calcium carbonate (CaCO_3) and nano-CdS, as well as some metal powders. The nanoparticles can be introduced into polymer matrices by different compounding methods, which are introduced in sub-section 1.3.

There is no doubt that rigid nanoparticles can improve the elastic modulus of polymer matrices. The reinforcing efficiency of nanoparticles has been shown to be dependent on the polymer system. In many cases, the improvement of elastic modulus is rather moderate [12-16] compared to that of organic nanoclay or nanofiber reinforced polymers at similar filler loadings. Generally, this is ascribed to the small aspect ratio of the quasi-spherical particles. The experimental moduli of nanocomposites usually lie between the upper and lower bounds calculated according to rule-of-mixtures (parallel and serial models) [15]. However, in some cases, the rule-of-mixtures fails to predict the experimental values. For example, Petrovicova et al [4] found that the nanosilica-filled nylon 11 composites exhibited a modulus higher than that calculated by the rule-of-mixtures. As explained by the

authors, the immobilized polymer layers surrounding the nanoparticles could increase the effective particle volume content, giving rise to the greater improvement of elastic modulus. On the other hand, nanoparticles may exhibit higher reinforcing efficiency than micron-particles in some polymer systems. Sumita et al [17] demonstrated that the dynamic storage modulus increased by 100% with the addition of 20 wt.% of 7-nm silica particles in polypropylene whereas the addition of the same amount of 200 μm particles caused only a marginal increase in the dynamic storage modulus.

Tensile strength is another key parameter for engineering applications. Generally speaking, the strength of micron-sized-particle filled systems decreases with increasing particle loading. In other words, the strength of the composite is always below that of the neat polymer matrix, as the filler does not bear any part of the external load [18]. In contrast, obviously increased strength has often been observed for nanoparticle-filled thermoplastics at low filler loadings. So far, the strengthening mechanisms of nanoparticles are still unclear.

More interestingly, nanoparticles can make the base matrix more ductile in some cases. Ash et al [19] reported that 5 wt.% nano-alumina filled PMMA showed a 600% increase in elongation at break at the cost of reduction in stiffness and T_g of base matrix. For comparison, neat PMMA and composites containing micron-sized alumina particles exhibited brittle failure. The authors explained this phenomenon as the transformation from craze formation to homogeneous shear yielding in nano-alumina/PMMA composites when the specimens were subjected to load.

Toughness of nanoparticle-filled composites deserves a separate treatise due to some contradictory findings in the literature. Understanding of the fracture, microdeformation and toughening mechanisms of nanocomposites is rather vague. Many factors (particle size, shape, distribution, type, aspect ratio, interface, particle concentration, dispersion, etc.) can affect the toughening efficiency of nanoparticles. To our knowledge, nanoparticles with a high aspect ratio, e.g. clay, often have negative toughening effects. This is because under external load the large aspect

ratio will generate significantly high stress concentrations at the ends of the particles, leading to earlier crack initiation and propagation, and finally having an adverse effect on material toughness [20]. For example, Chen et al [21] reported that the J -integral value of polypropylene (PP) decreased significantly with an increase of clay filler content. Bureau et al [22] found that the addition of clay (with/without coupling agents) into PP matrix reduced the specific essential fracture work, w_e , but increased the specific non-essential fracture work item, βw_p . Quasi-spherical nanoparticles are recognized as more promising for polymer toughening. Chan et al [15] conducted very tough PP/CaCO₃ nanocomposites by melt compounding, and the J -integral tests showed a dramatic 500% increase in fracture toughness. In such case, the nanoparticles can act as stress concentration sites, which can promote cavitation at the particle-polymer boundaries, further releasing the plastic constraints and triggering mass plastic deformation of the polymer. With regard to the effect of particle size on polymer toughening, nanoparticles have been shown to be more effective in polymer toughening than micron-sized particles in some polymer systems. For example, Singh et al [23] considered that the enhancement in fracture toughness of Al/unsaturated polyester composites was directly related to particle size. Smaller particles resulted in higher fracture toughness.

1.2.2 Carbon-nanotube-filled Composites

Carbon nanotubes were discovered by Iijima in 1991 [24]. They have nanometer scale diameters, are up to ten of microns long, and can be single- or multi-walled (SWNT and MWNT, respectively) [25]. The elastic modulus of carbon nanotubes has been measured as approximately 1-2 TPa, compared to the typical value of 750 GPa of carbon fibers. The strength of carbon nanotubes has been reported to be about two orders of magnitude higher than that of current high-strength carbon fibers [26-28]. Combining outstanding mechanical properties with low density and high thermal and electrical conductivity, nanotubes have stimulated the development of nanotube-filled polymer composites for both structural and functional applications.

In the past decade, much work has been carried out to prepare and investigate carbon-nanotube-based polymer composites [2,29-49]. Indeed, as reported in the literature, even a small amount of nanotubes has obvious effects on the mechanical performance of polymers. Nevertheless, the reinforcing efficiency of nanotubes has been found to be dependent on polymer matrix systems. Coleman [2] reported that, with less than 1 vol.% MWNT, poly(vinyl alcohol) and chlorinated polypropylene achieved approximately 300-400% increases in modulus and strength, respectively, which represented the highest reinforcing effects up to now. Liu et al [29] also pointed out that the elastic modulus and yield strength of the composites were greatly improved, by about 214% and 162% respectively, with incorporation of only 2 wt.% MWNTs. However, for some glassy polymers, e.g. epoxy and poly(methyl methacrylate), only moderate enhancement or even a slight decline in modulus and strength are usually obtained after the incorporation of nanotubes [30-34]. The great discrepancy in reinforcing efficiency of nanotubes is ascribed to several well-known issues, such as dispersion state, interfacial adhesion between nanotubes and polymers, nanotube alignment in polymers and the effect of nanotube waviness [35].

Fracture toughness, which reflects the ability of a material to resist a pre-crack under stress applied, is another crucial parameter of polymers for engineering applications. Some studies deal with the toughness of polymer-nanotube composites [2,32,36-40], but the results seem to be somewhat contradictory. For thermosets, Wagner and co-workers [30,33] found substantial improvement in double-notched impact strength by adding only minute nanotube weight fractions to epoxy resins. In contrast, a slightly decreased Izod impact strength in fluorinated SWMT/epoxy systems has been reported by others [36]. Regarding thermoplastics, a moderate increase in the Izod impact strength of MWNT/ polypropylene system was observed [37]. MWNTs were found to demonstrate enhanced resistance to crack propagation compared to unfilled polycarbonate matrix under quasi-static tensile testing using the EWF approach [38], whereas obvious negative effects of nanotubes on impact strength were reported in PA6/ABS blends [39]. In addition, several investigators [2,32] have pointed out that the tensile toughness of nanotube-based polymers, calculated from the area under stress-strain curves of tensile tests, was enhanced more or less, in comparison with

the pristine matrix. However, it is worth noting that high tensile toughness does not necessarily mean high notched fracture toughness [15] since the specimens are loaded under different stress conditions (i.e. the plane-stress state for the former but the plane-strain state for the latter). Unfortunately, the plane-strain state can cause catastrophic material failure in engineering applications and thus notched fracture toughness is always regarded as a critical parameter in material selection [15]. Therefore, in this thesis, notched samples were used to characterize the fracture resistance of nanotube-filled polypropylene composites.

The toughening mechanisms of nanotubes would be analogous with those of micron-fiber-filled polymer composites, i.e. nanotube pullout, bridging and fracture are considered to be the common energy consumption events. Ajayan and co-workers [43] claimed that SWNTs in the epoxy resin could pull out from many directions without failing, which would increase the effectiveness of the pullout and crack bridging contributions to toughness. The authors also pointed out that, based on SEM observations, the configuration of nanotubes across the cracks depended on the ratio of average tube length to the separation of the crack surfaces. Qian et al [44] observed via TEM that nanotubes were able to bridge the crack surface of polystyrene composites once a crack was initiated. A crack nucleated at low nanotube density area can propagate towards a region with relatively low nanotube density. Pullout of nanotubes was observed when the crack opening displacement reached ca. 800 nm. Another potential energy dissipation mechanism would result from interfacial sliding at the nanotube-polymer interface and interfacial friction at the nanotube-nanotube interface. For example, Suhr et al [45] found that epoxy thin films containing MWNTs had strong viscoelastic behaviour under dynamic loading. For composite films, up to 1400% improvement in loss factor was obtained through the possible energy dissipation mechanism mentioned above.

1.3 Compounding Techniques for Nanocomposites

As mentioned before, nanofillers can lead to significant improvements in the mechanical properties of polymer matrices if a homogeneous state of nanofillers can be achieved. However, aggregates or clusters in micron scale can be often observed

in filled polymer composites. This is mainly due to the strong tendency of nanofiller to agglomerate in polymer matrices. Such occurrences are especially serious at higher nanofiller loadings. Accordingly, the mechanical properties of such nanocomposites are even poorer than those of neat matrix. In principle, the aggregates can result in significant reductions in tensile strength and fracture toughness; however, they have only a small influence on the elastic modulus of the resulting materials. Up to now, the commonly used compounding methods can be divided into three major groups: (i) *in situ* polymerisation, (ii) solvent-assisted techniques and (iii) melt compounding [1]. In this thesis, the nanosilica-particle filled epoxy resins were formed *in situ* through a sol-gel method (prepared by hanse chemie AG), while the nanofiller-reinforced thermoplastics were manufactured by conventional melt compounding. Therefore, both these processes are briefly introduced here.

1.3.1 Sol-gel Method

The *in situ* sol-gel technique is normally used for the preparation of organic-inorganic hybrids. Many nanofiller/polymer systems can be prepared by the sol-gel process [50-52]. By this process, inorganic or inorganic-organic materials can be produced from liquid starting products via a low temperature process [53]. The most frequently used precursor in the sol-gel process is tetraethoxysilane (TEOS). The nanosilica particles can be formed through polymerization of TEOS, as depicted in the related reference in detail [54]. As a result, nanoparticles can be produced elegantly and free of agglomerates. Moreover, the distribution of nanoparticle size is extremely narrow.

1.3.2 Melt Compounding

Melt compounding is the most attractive way to produce commercial nanocomposites. The advantages of this technique are: (i) fast dispersion of the nanoparticles in the melt, (ii) available industrial melt compounding capacities and (iii) environmental friendly preparation [1]. A large percentage of nanofiller-reinforced thermoplastic and rubber composites are fabricated using twin-screw extruder, kneading or open mill

machines [55-57]. However, to the author's knowledge, it seems to be difficult to achieve satisfactory particle dispersion, especially at higher filler content.

1.3.3 Other Methods

To overcome the difficulties often encountered in preparation of nanocomposites, several alternative techniques have been proposed.

One method, radiation grafting of macromolecular chains on to the nanofillers, appears to be very effective. As reported by Rong et al [58,59], nanosilica particles were treated through irradiation grafting so that macromolecular grafting chains could form onto the surfaces both inside and outside the nanoparticle aggregates. These modified nanosilica particles were mechanically mixed with PP matrix as usual. Even though a completely uniform distribution of the particles could not be achieved during the compounding, the tensile strength and fracture toughness of the matrix were significantly improved. Moreover, a brittle-to-tough transition was found at rather low particle content. Hypothetical model of double percolation was suggested by the authors to explain this phenomenon.

Another method is related to the preparation of carbon-nanotube-filled polymer composites. To date it is still a great challenge, since the very high aspect ratio of nanotubes can cause extremely high viscosity in melt or dissolved polymers, which in turn affects the uniform dispersion of nanotubes and further limits their maximum loading in polymers. Generally speaking, the typical loading of nanotubes in polymers (especially for thermosets) is limited to only 5 vol.% or less. In order to resolve these problems, several innovative processing techniques have been developed recently. For example, Wang et al [60] fabricated SWNT buckpapers/epoxy nanocomposites by infiltrating and subsequent hot-press procedures. The SWNT loading in the resulting composites was as high as 39 wt.%. Accordingly, the dynamic storage modulus of the nanocomposite was about four factors greater than that of the original epoxy resin. Similarly, Baughman and co-workers [61] successfully prepared SWNT-

sheet-reinforced polymer composites. The mechanical properties of these composites were greatly improved in comparison with those of neat polymer matrices.

1.4 Toughening Mechanisms of Inorganic Rigid Particles

To improve the crack resistance of polymer matrices, numerous toughening techniques have been developed during recent years, and can be roughly classified as two types: rubber toughening and inorganic rigid particle toughening. In the present work, only the latter is described in detail. The fracture behaviours of rigid-particle-filled polymer matrices result from a complicated interplay of the properties of the constituent phases: matrix, filler and interphase. Many relevant parameters such as filler type, filler size, aspect ratio, filler-matrix interphase, strain rate and testing temperature influence the toughening effects to greater or lesser degree. Although rigid particle toughening has been studied for over 30 years, theoretical understanding of the toughening mechanisms is still lacking. Many contradictory explanations exist in the opening publications. For most cases, the toughening phenomenon is too complicated to be explained by a simple mechanism. This is due to the fact that the fracture behaviours of composites may involve several mechanisms, each one contributing towards the total fracture toughness of the materials. Some toughening mechanisms are discussed in following section. Although the toughening mechanisms and the general principles described below are based on conventional polymer composites filled with micron-sized fillers, they can still supply much useful information to nanoparticle-toughened polymer systems.

1.4.1 Thermoplastic Matrix

The general idea for most rigid-toughened thermoplastics is to intimate toughening mechanisms of rubber-thermoplastics blends. Argon and Cohen [62-64] proposed that for toughening to occur in rigid filler systems, the fillers must debond from the matrix, creating voids around the particles and allowing the interparticle ligaments to deform plastically. A schematic diagram of this toughening process is shown in Figure 1.2.

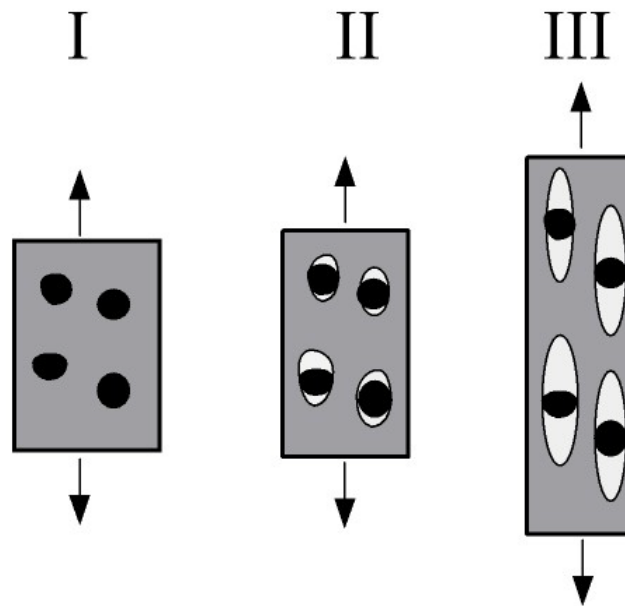


Figure 1.2: Toughening mechanism of rigid-particle-reinforced thermoplastics [65].

As illustrated, there are three stages for the micro-mechanism of filled thermoplastics proposed by Friedrich and co-worker [65]: at the first stage, the rigid particles act as stress concentrators due to the difference of elastic modulus between particle and matrix; thereafter triaxial stress is accumulated around particles, which leads to debonding at the particle-matrix interface; finally, the stress state is altered due to the formation of cavitation. Shear yielding instead of crazing is developed, which is accompanied by the consumption of a large amount of fracture energy. Based on the above micro-mechanistic model, Zuiderduin et al [20] pointed out that the rigid nanofiller must satisfy several prerequisites for toughening polymers, which mainly involve smaller filler size (several microns), non-aggregates, low aspect ratio and appropriate filler-matrix interfacial bonding.

It can be seen from Figure 1.2 that the debonding process of reinforcement plays the key role in toughening of polymer matrix. It is well accepted that the debonding of fillers depends highly on the interface between filler particles and polymer. Thio and co-workers [66] suggested that for the purpose of toughening, relatively weak interfacial adhesion between filler and matrix was desirable, which can promote earlier debonding during load. The earlier debonding causes greater plasticity in the

composites during deformation, which translates into significantly higher macroscopic toughness. Lazzeri et al [67] indicated that debonding time was crucial for toughening. This means that if the particle-matrix debonding occurs too early (when the material is still in its elastic stage), the triaxial state of stress at the crack tip will favour matrix crazing and brittle fracture. Only 'just-in-time' debonding, i.e. close to yielding, can produce high toughening effects.

On the other hand, mobility of the polymer matrix is considered to be a precondition for the various toughening mechanisms to be effective. Recently, Shah et al [68] found that for nano-clay-filled polymer composites (including semicrystalline and amorphous polymer matrices), increase in toughness corresponded with increase in the mobility of the polymer chain.

1.4.2 Thermosetting Matrix

Over the past two decades, many toughening mechanisms have been proposed to explain the improved toughness in rigid-filler-reinforced thermosetting polymers. Some major mechanisms that are usually present in filled polymer systems are summarized below.

1.4.2.1 Crack Deflection

The crack deflection toughening mechanism was introduced by Farber and Evans [69,70]. A schematic diagram is shown in Figure 1.3. In their assumption, when a crack front approaches an obstacle, it is tilted and even twisted out of its original plane, thus producing non-planar cracks. The tilted and twisted cracks are subjected to mixed-mode local loading (mode I/II for the former and mode I/III for the latter). Since most polymers have much higher toughness in mode II/III (shear/tear) than in mode I (tensile), an increase in fracture energy due to the crack deflection is expected. This mechanism is unrelated to particle size, but it is thought that uneven spacing provides better results than uniform spacing. Particle morphology also

affects the deflecting advancing cracks, particles with high aspect ratio is proved to more effective in toughening than disc-shaped or spherical particles [69].

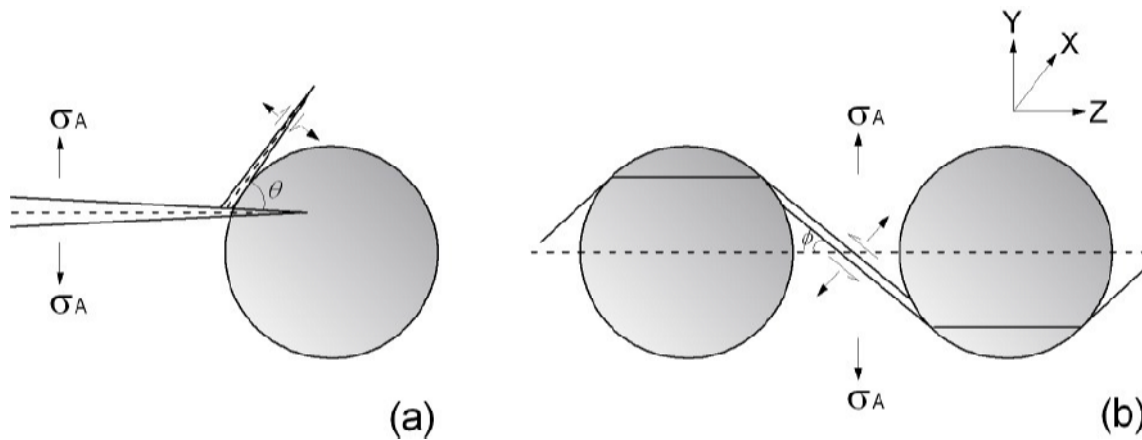


Figure 1.3: A schematic of crack deflection mechanism [69]: (a) crack tilting, (b) crack twisting.

1.4.2.2 Crack Pinning and Bowing

The crack pinning and bowing toughening mechanism was first proposed by Lange [71] and was developed by Green et al [72]. A schematic diagram is shown in Figure 1.4. This theory assumes that when a crack meets an array of rigid particles it becomes pinned and tends to bow out between the particles by forming secondary cracks, thereafter leaving a characteristic step structure, which is usually termed a *tail*. The bowed secondary crack front has more elastic energy stored than the straight unbowed one. Therefore, more energy is required for crack propagation. Crack bowing is a particularly important toughening mechanism in rigid-particle-reinforced brittle polymer systems, and is considered the dominant toughening mechanism in some particle-filled systems [73]. Additionally, good particle-matrix bonding is necessary, because it can enhance the efficiency of pinning [74].

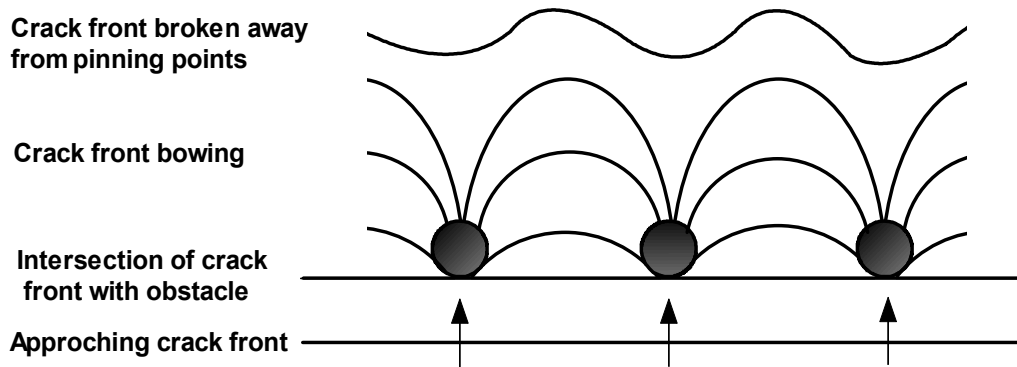


Figure 1.4: A schematic of crack pinning/bowing mechanism.

1.4.2.3 Particle Bridging

As shown in Figure 1.5, fillers can act as bridging behind the crack tip, thus increasing the resistance to crack propagation. This mechanism has been found to be effective also in ductile-filler-reinforced epoxy systems (e.g. rubber or thermoplastics particles) [75]. It is clear that this toughening mechanism favours larger particles or fillers with higher aspect ratios.

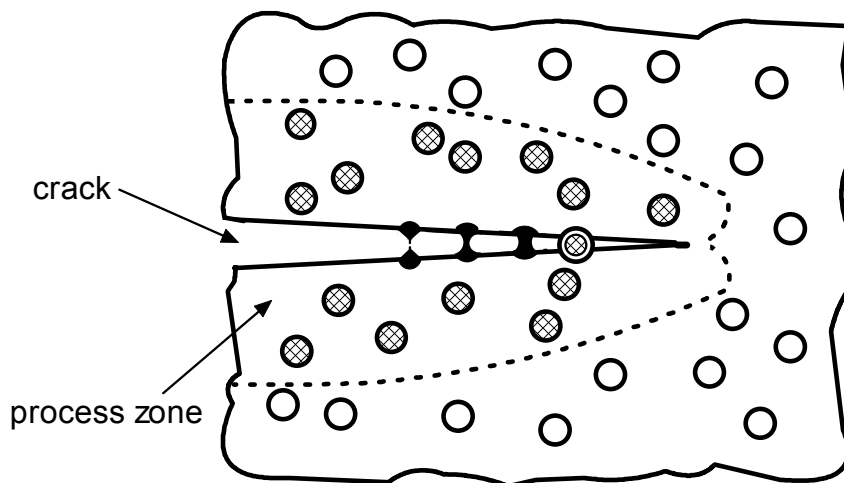


Figure 1.5: A schematic of crack bridging mechanism.

1.4.2.4 Microcracking

Due to the stress concentration effect, rigid fillers can induce microcracks of the polymer matrix around the crack tip. This microcracking can effectively reduce the

modulus in the frontal process zone and increase the fracture surface area, and further relieve the stress intensity. For some epoxy resins filled with rigid particles (micro-sized glass spheres [76] and nano-clay fillers [77]), microcracking is considered as the major toughening mechanism.

1.4.2.5 Plastic Deformation

Despite the heavily crosslinked structure of thermosetting polymers (e.g. epoxy resin), they can still develop some shear deformation and plastic zone near the crack tip. The plastic zone can blunt the crack tip, reduce the local stress concentration and allow the material to support higher loads before failure.

2 Aim of this Work

As reviewed in Chapter 1, significant improvements in mechanical performance can be achieved through the incorporation of nanofillers. Therefore, polymer-based nanocomposites promise to become novel structural materials in various engineering applications. Nevertheless, much fundamental work is still needed for deep understanding of the process-structure-property relationships in nanocomposite systems.

In general, the aim of this study is focused on the mechanical properties of nanocomposites measured under different testing conditions; moreover, special attention is devoted to the fracture behaviours and the relevant toughening mechanisms of nanocomposites. With this purpose, different kinds of polymers were selected as base matrices. Two kinds of epoxy resin (cycloaliphatic type and bisphenol-F type) served as the thermosetting polymer matrices, while polyamide 66 and isotactic polypropylene served as the thermoplastic polymer matrices. For the thermosetting systems, the nano-SiO₂ particles were *in situ* introduced into epoxy resins by using a special sol-gel method, whereas for the thermoplastic systems various nanofillers such as SiO₂, TiO₂, Al₂O₃ and multi-walled carbon nanotubes (MWNT) were added to the original thermoplastic matrices by conventional melt extrusion, i.e. the commonly used method in industrial applications. The main concerns of this work are summarized below:

- To homogeneously disperse nanofillers in polymer matrix using different mixing techniques, including a laboratory mixing device and a twin-screw extruder.
- To evaluate the various mechanical properties of the nanocomposites under different testing conditions (e.g., under static and dynamic loads, at different testing temperatures) and to more thoroughly understand the reinforcing mechanisms of nanofillers.

-
- To characterize the fracture behaviours of brittle and ductile nanocomposites according to the related mechanics theories. To investigate the temperature dependence of fracture toughness of the nanocomposites (not for all material systems).
 - To discuss the related toughening mechanisms of nanofillers based on fractography and modelling calculation.

3 Experimental Procedures

3.1 Materials and Sample Preparation

In this work, two distinct polymeric systems, thermosetting and thermoplastic composites, were considered. The thermosetting material systems included two types of epoxy-based nanocomposites (cycloaliphatic and bisphenol-F), which were kindly supplied by hanse Chemie AG. The nanoparticles (nanosilica) in the epoxy resins were *in situ* introduced by a special sol-gel technique. For the thermoplastic material systems, two commercially available semicrystalline polymers, polyamide 66 (Zytel[®] 101L, DuPont Co.) and isotactic polypropylene homopolymer (Molpen[®] HP501H, Basell Co.), were selected as matrices. Various nanoparticles were added to the neat matrices by the melt-extrusion method, the most commonly used method in industrial applications.

3.1.1 Thermosetting Composites

As stated above, two types of epoxy resin, cycloaliphatic type and bisphenol-F, were used in this study. Corresponding master batches of SiO₂/epoxy were also used. The nanosilica in the epoxy master batches was *in situ* manufactured via a novel sol-gel technique. The master batch contained c.a. 40 wt.% of spherical nanosilica particles in a narrow particle size distribution (5-50 nm) and with an average diameter of 25 nm. In spite of the high concentration of nanoparticles the master batch still retained good fluidity, and therefore could be easily handled at ambient temperature. An anhydride curing agent (Albidur HE 600, hanse Chemie AG) was used in this study. Basic information about the epoxy matrices and curing agent is given in Table 3.1. The compounding procedures for the two types of epoxy systems were similar. For example, the compounding of cycloaliphatic epoxy/SiO₂ nanocomposites was carried out by the following steps: (i) before mixing, the neat epoxy resin and master batch were warmed to 70 °C to remove possible crystals inside; (ii) the master batch was diluted in an appropriate amount of the neat epoxy resin and then mechanically mixed with a stoichiometric ratio of the anhydride curing agent at 60 °C for 30 min; (iii)

the mixture was subsequently placed under vacuum for removing trapped bubbles; and finally (iv) it was cast into aluminium and silicone moulds for curing. A four-step curing schedule was selected as recommended by the supplier. As a result, a series of epoxy-based nanocomposites with desired nano-silica contents was prepared. For the bisphenol-F system, almost all processing steps were same except the curing schedule. The designation of prepared samples is given in Table 3.2.

Table 3.1: Basic characteristics of SiO₂/epoxy master batch and curing agent

Designation	Cycloaliphatic type master batch	Bisphenol-F type master batch	Anhydride curing agent
Brand name	Nanopox XP22/0314	Nanopox F520	Albidur HE600
SiO ₂ content [wt.%]	~40	~40	---
Viscosity at 25°C [mPa·s]	~4000	~20000	~80
Epoxy equivalent weight [g/equiv]	250	275	170
Curing schedule [°C/hr]	90/3;120/1;140/1;160/4	120/1;160/2	---
Density [g/cm ³]	1.40	1.35	1.07

Table 3.2: Designation of cycloaliphatic and bisphenol-F epoxy samples

Epoxy type	Sample code	SiO ₂ content [vol.%]	SiO ₂ content [wt.%]
Cycloaliphatic	X0	0	0
	X1	1	1.8
	X3	3	5.3
	X6	6	10.3
	X10	10	16.7
	X12	12	19.7
	X14	14	22.7
Bisphenol-F	F0	0	0
	F1	1	1.8
	F3	3	5.2
	F6	6	10.3
	F7	7	12.0
	F8	8	13.6
	F10	10	16.8
	F13	13	21.5
	F15	15	24.7

3.1.2 Thermoplastic Composites

In this study, various nanoparticles were selected as additional reinforcements for thermoplastic polymers. They were nano-TiO₂ (with and without surface modification), nano-SiO₂, nano-Al₂O₃ and multiwalled nanotubes of different lengths. The detailed characteristics of the nanoparticles are listed in Table 3.3.

Table 3.3: Basic characteristics of nanoparticles used in thermoplastic polymers

Nanoparticle type	Brand name/ manufacturer	Diameter [nm]	Length [μ m]	Density [g/cm ³]	Specific surface area (BET, m ² /g)	Surface modification
TiO ₂	P25/degussa	21	---	4.0	50 \pm 15	None
TiO ₂	T805/degussa	21	---	4.0	45 \pm 10	Ostylsilane
TiO ₂	Kronos 2310	300	---	4.0	~18	None
SiO ₂	R7200/degussa	13	---	2.2	150 \pm 25	Methacrysilane
Al ₂ O ₃	Al-C/degussa	13	---	2.9	100 \pm 15	None
Nanotube	MWCNTs/NTP	10~30	1~2	1.75	---	None
Nanotube	MWCNTs/NTP	10~30	5~15	1.75	---	None

The compounding of nanoparticles with thermoplastic polymers was carried out in a co-rotating twin-screw extruder with well-designed elements (Berstoff ZE 25A \times 44D-UTS). Prior to compounding, the polymer granules (PA66 or iPP) and nanoparticles were dried in an oven at 70 °C for c.a. 72 hours. Then they were mixed using a twin-screw extruder at a screw speed of 150~200 rpm. The mixing temperatures were 260~285 °C for PA66 and 185~200 °C for iPP, respectively. During melt extrusion, ventilation was kept on to remove trapped air in the blends. After extrusion, the blend granules were injection-moulded into square plates of different thickness and dog-bone shape specimens using an injection-moulding machine (Alburg Allrounder 320S). For all samples, the parameters of injection moulding were kept constant. The injection pressure and speed were 500 bar and 80 cm³/s, respectively. For PA66 composites, the barrel temperature was set 290 °C, and the mould temperature was kept at 70 °C. For iPP composites, they were 220 °C and 40 °C, respectively. As a reference, neat polymer matrices were also processed similarly to ensure analogous process conditions and thermo-mechanical history for all studied materials. The

nanoparticle content was set constant as 1 vol.%. A detailed description of the PA (PP)-based nanocomposites is given in Table 3.4.

Table 3.4: Designation of filled PA66 and PP samples

Sample code	Matrix	Nanoparticle	Volume content [%]
Neat PA	PA66	---	---
1TPA		Nano-TiO ₂ , P25	1
1T805PA		Nano-TiO ₂ , T805	1
1R7200PA		Nano-SiO ₂ , R7200	1
1APA		Al ₂ O ₃ , Aluminium-C	1
Neat PP	PP	---	---
1TPP		Nano-TiO ₂ , P25	1
1T805PP		Nano-TiO ₂ , T805	1
1KrPP		Nano-TiO ₂ , Kronos 2310	1
1MPP		MWNT, 1~2 μm	1
1LPP		MWNT, 5~15 μm	1

3.2 Fracture Toughness

In polymeric composites, there are two general modes of failure: *brittle fracture*, characterized by a linear relationship between an applied load and sample displacement, and *ductile fracture*, characterized by plastic yielding. This yielding is manifested in the load-displacement curve as a decrease in the slope of the load-displacement curve prior to failure. As illustrated in Figure 3.2, brittle fracture is frequently a result of highly localized crazing, confined to a very small volume of the material. Ductile fracture, on the other hand, is accompanied by a comparatively large plastic zone during crack initiation and subsequent crack propagation, which is usually due to multiple crazing or shear yielding. Sometimes, a mixed failure mode may occur in the one specimen.

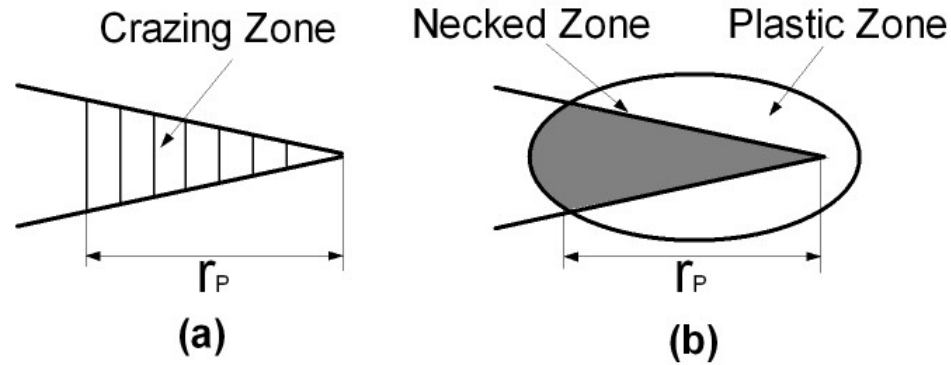


Figure 3.2: Typical crack tip deformation zones in (a) brittle, (b) ductile polymeric materials.

Because of the different failure modes, several techniques for measuring fracture toughness of polymeric composites have been developed. Among them, linear elastic fracture mechanics (LEFM) is one of the most frequently used methods to characterize the fracture behaviour of brittle materials. The fracture toughness in LEFM can be represented in terms of the stress intensity factor K , or the strain energy release rate G . The stress intensity factor is based on stresses around a crack tip. The strain energy release rate is a measure of the energy available to extend a crack of a unit area. According to LEFM theory, when K (or G) reaches a critical value K_c (or G_c), failure occurs. However, for ductile materials, LEFM becomes invalid since a large plastic deformation zone exists around the crack tip (see Figure 3.2b) and the energy dissipated in this zone can no longer be attributed to the fracture process. Therefore, several alternative techniques are used, such as the crack growth resistance curve (R-curve), the crack opening displacement (COD), the J -integral analysis, essential work of fracture (EWF), and so on. In this study, the LEFM theory and the EWF technique were respectively employed to determine the fracture toughness of thermosetting and thermoplastic nanocomposites, which are described in detail in the following sections.

3.2.1 K_{IC} and G_{IC} for Brittle Materials

Quasi-static fracture toughness tests were performed with compact tension (CT) specimens according to LEFM method [78]. The configuration of CT specimens is

shown in Figure 3.3, where a , B and W represent the specimen dimensions. In the present study, specimen thickness B was chosen to be 3.4 mm for cycloaliphatic epoxy specimens and 5.7 mm for bisphenol-F specimens. The pre-crack was made by lightly tapping a fresh razor blade into the bottom of the saw slot in the specimen. By this technique, the crack can pop into the material over several millimetres, yielding a very sharp natural crack. The crack range should satisfy $0.45 < a/W < 0.55$. Tensile loading of the CT specimens took place on a Zwick 1485 universal testing machine with a crosshead speed of 0.1 mm/min for cycloaliphatic epoxy specimens and 1 mm/min for bisphenol-F epoxy specimens. The actual crack length was measured after the fracture experiment by an optical microscope equipped with a micrometer scale. Three to five specimens were measured for each composition. The critical stress intensity factor K_Q was then calculated from the following relationship:

$$K_Q = f \frac{P_Q}{BW^{1/2}} \quad (3.1)$$

where P_Q is the maximum force in the load-displacement curve, and f is the calibration factor for the CT specimen, which is obtained according to the equation:

$$f = \frac{(2 + \alpha)}{(1 - \alpha)^{2/3}} \left[0.886 + 4.64\alpha - 13.32\alpha^2 + 14.72\alpha^3 - 5.6\alpha^4 \right] \quad (3.2)$$

where $\alpha = a/W$

Since the dimensions of all specimens satisfied the equation:

$$B, a, (W - a) > 2.5 \left(\frac{K_Q}{\sigma_y} \right)^2 \quad (3.3)$$

K_Q was considered to be equal to K_{IC} , i.e. the plane strain critical stress intensity factor. Here, σ_y is the uni-axial tensile yield stress of the specimens. Moreover, the critical strain energy release rate in a plane strain state, G_{IC} , can be obtained by equation,

$$G_{IC} = \frac{(1 - \nu^2) K_{IC}^2}{E} \quad (3.4)$$

where E is the Young's modulus of the composites, ν is the Poisson's ratio, which was set to be a constant of 0.35 for all epoxy nanocomposites.

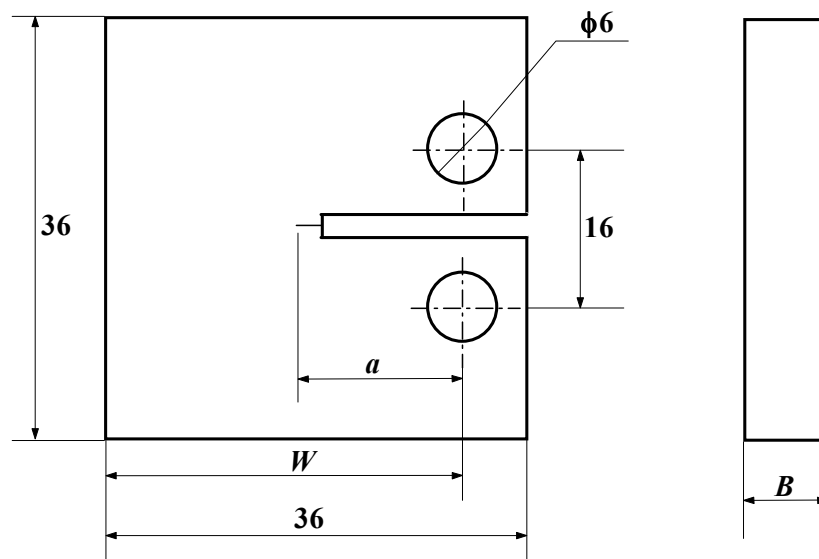


Figure 3.3: The configuration of a CT specimen.

3.2.2 Essential Work of Fracture (EWF) for Ductile Materials

3.2.2.1 Concept of EWF

The essential work of fracture (EWF) approach, first proposed by Broberg [79-81], has been used to characterize the plane-stress-state fracture toughness of ductile materials, including metals, papers, polymers, fibre composites and even foods. The EWF method has gained popularity owing to its experimental simplicity, especially compared to the J -integral technique. Reports have indicated that the EWF parameters are affected by a number of factors such as sample geometry [82-86], test conditions [87-91], notching method [92,93], polymer composition [94,95], filler fraction [96-98] and so on [99-102]. Recently, this method has been introduced to investigate fracture behaviours of polymer nanocomposites as well [103].

According to the EWF concept, when a crack propagates in a ductile material, the total work of fracture (W_f) can be separated into two parts: essential work (W_e) and non-essential work (W_p). The former represents the pure energy required to fracture the material and is proportional to the fracture area, while the latter represents the energy consumed by various deformation mechanisms in the outer plastic zone and is hence proportional to the volume of the outer region. So W_f can be described as:

$$W_f = W_e + W_p = w_e l t + \beta w_p l^2 t \quad (3.5)$$

where l and t are the ligament length and thickness of specimen, respectively. β is a dimensionless shape factor associated with the volume of plastic deformation zone.

Dividing equation (3.5) by $l t$, we obtain

$$w_f = \frac{W_f}{l t} = w_e + \beta w_p l \quad (3.6)$$

According to equation (3.6), the specific essential and non-essential work of fracture (w_e and βw_p) can be obtained from linear regression of a set of values represented in a diagram of specific total work of fracture w_f vs. ligament length l (Figure 3.4b).

In the interests of consistency and reproducibility, it is recommended in the European Structural Integrity Society (ESIS) protocol for EWF measurement [104] to use deeply double-edge-notched tensile specimen (DDENT, as shown in Figure 3.4c). In order to maintain a state of plane stress, the ligament length of specimens must satisfy inequation (7), although the restriction on ligament length is reported to be rather conservative in certain polymer systems [105]:

$$\max(3t, 5\text{mm}) < l < \min(W / 3, 2r_p) \quad (3.7)$$

where r_p is the radius of the plastic zone at crack tip.

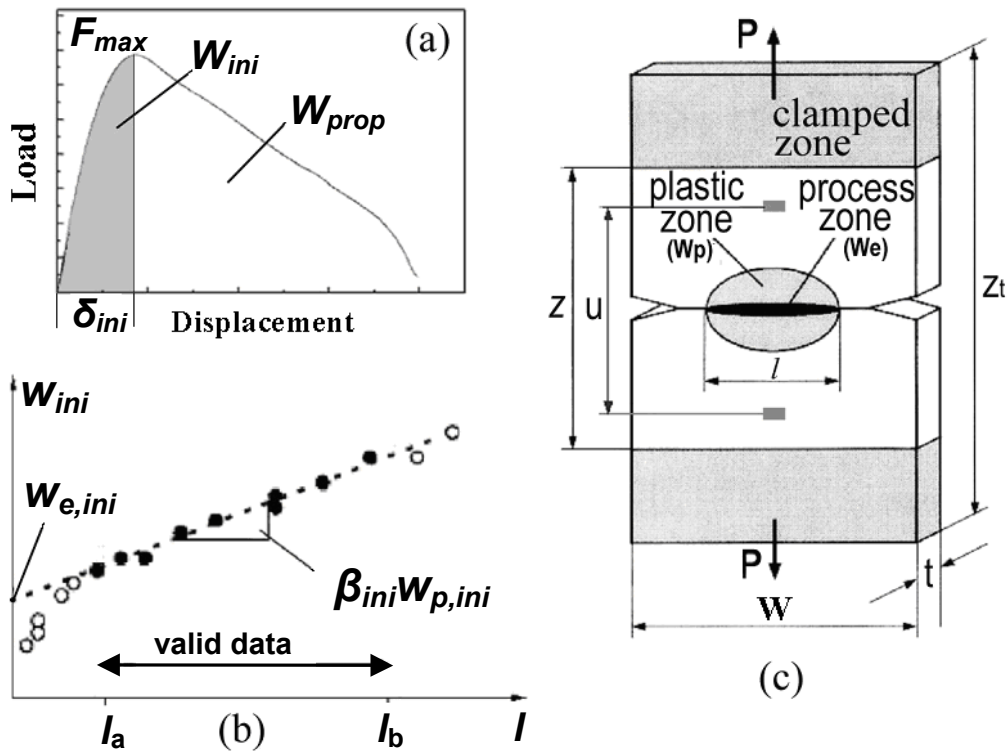


Figure 3.4: Schematic diagram of the essential work of fracture (EWF) approach: (a) a typical load-displacement curve; (b) a curve of specific total work of fracture vs. ligament length; and (c) a deeply double-edge-notched tensile (DDENT) specimen.

3.2.2.2 Partitioning of EWF

To deeply understand the fracture behaviour of ductile material, the total fracture energy can be divided from the maximum load point F_{max} in the load-displacement ($F-\delta$) curve, as schematically shown in Figure 3.4a. In the present study the method proposed by Karger-Kocsis [105] and Hashemi [89] was adopted. In the $F-\delta$ curve a sudden load drop at F_{max} indicates that the ligament region of the DDENT specimen reaches full yielding and then the ligament necking and subsequent tearing occur. Based on the clear load drop, the total work of fracture W_f is divided into two items, i.e. work for crack initiation (W_{ini}) and subsequent crack propagation (W_{prop}). Thus W_f can be expressed as:

$$W_f = W_{ini} + W_{prop} \quad (3.8)$$

Based on EWF concepts, either W_{ini} or W_{prop} is also considered as a sum of the essential and non-essential work of fracture. In analogy with equation (3.6), we can obtain immediately:

$$W_{ini} = \frac{W_{ini}}{lt} = W_{e,ini} + \beta_{ini}W_{p,ini}l \quad (3.9)$$

$$W_{prop} = \frac{W_{prop}}{lt} = W_{e,prop} + \beta_{prop}W_{p,prop}l \quad (3.10)$$

where w_{ini} and w_{prop} are the specific items of W_{ini} and W_{prop} , respectively; $w_{e,ini}$ and $w_{e,ini}/w_{p,prop}$ and $w_{p,prop}$ are the specific essential/non-essential work of fracture related to crack initiation and propagation stages; β_{ini} and β_{prop} are the dimensionless shape factors of aforementioned two stages. We can in the same way determine the $w_{e,ini}/w_{e,prop}$ and $\beta_{ini}w_{p,ini}/\beta_{prop}w_{p,prop}$ from the intercepts and slopes of the corresponding linear regression equations.

It is evident from equation (3.5), (3.8), (3.9) and (3.10):

$$W_e = W_{e,ini} + W_{e,prop} \quad (3.11)$$

$$\beta W_p = \beta_{ini}W_{p,ini} + \beta_{prop}W_{p,prop} \quad (3.12)$$

In the present work we concentrate only on the W_{ini} and its related parameters, since they represent the fracture energy consumed at the crack initiation stage and are the crucial parameters for material design in engineering applications.

3.2.2.3 EWF Test

EWF tests were performed on DDENT specimens with dimensions shown in Figure 3.4c. The pre-crack was made by slowly pushing a fresh razor blade into the bottom of the saw slot. The sharp pre-crack is very important, because a blunt one can produce an abnormally high w_e value [104]. In the present work the sharpness of the pre-crack was confirmed as shown in Figure 3.5. To satisfy the state of plane stress, the ligament length of the specimen ranged from 6 to 13 mm. Quasi-static tensile tests were performed on a universal testing machine (Zwick 1485) at a constant crosshead speed of 1 mm/min for PA66 composites and 5~50 mm/min for iPP composites. The displacement of each specimen during tension was accurately

measured by an extensometer. After tests a light microscope was used to measure the ligament length and the average value was used for each specimen. The specific essential and non-essential work of fracture were obtained from linear regression equation as mentioned earlier. The data were processed according to the ESIS protocol [104]. At least 20 specimens were tested for each composition.

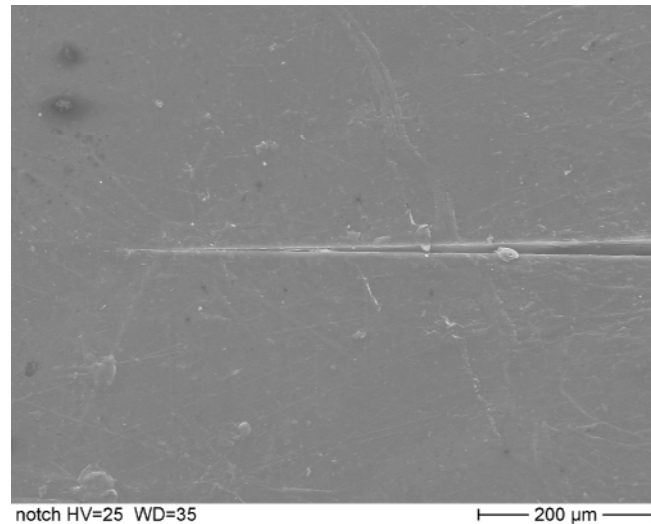


Figure 3.5: A sharp pre-crack prepared by razor blade in the present work.

3.3 Other Mechanical Properties

3.3.1 Tensile and Flexural Tests

Tensile and flexural (three-point-bending geometry) tests were conducted with a Zwick 1485/1445 universal testing machine according to the standards ASTM D-638 and DIN-ISO-178, respectively. A load cell of 10 kN was selected. Different crosshead rates were applied to different sample systems (1 mm/min for epoxy and PA66, 5 mm/min for iPP). The experimental data represent the average of five specimens.

3.3.2 Microhardness Test

Micro-hardness tests were performed using an ultra-micro-hardness tester (Shimatzu DUH-202). A load range of 1000 mN at a loading and unloading speed of 35 mN/s

was selected. The universal micro-hardness HU (MPa) was calculated according to the following equation [106]:

$$HU = \frac{P}{26.43h^2} \quad (3.13)$$

where P is the force applied in [mN], and h is the indenter penetration depth in [μm]. HU represents the strength characteristics including both plastic and elastic deformation. The average values with standard deviations were reported from five measurements of each composition.

3.3.3 Charpy Impact Test

Impact test was conducted with an instrumented impact tester (AFS-MKs fractoscope of Ceast, Torino, Italy) according to standard ISO179. Striker energy of 4 J, testing time of 4~8 ms and final velocity of 2.9 m/s were applied. For thermosetting materials, an unnotched rectangular bar ($4 \times 10 \times 80 \text{ mm}^3$) was chosen. For thermoplastic materials, a notched rectangular bar (single-edge V sharp notch of 2 mm depth and tip radius of 0.25 mm) was cut from 4-mm injection-moulded plates along the mould flow direction (MFD). The impact tests were also performed at -196 , 23, 50 and 80 °C. The low temperature tests were achieved by immersing specimens into liquid nitrogen for more than 30 min and then testing immediately (less than 5 sec. delay). For the tests above room temperature, specimens were firstly warmed in an oven for 1 hour and then quickly tested on the impact tester. Measurements were made on at least six specimens and the average value together with standard deviation was reported.

3.3.4 Dynamic Mechanical Thermal Analysis

Dynamic mechanical thermal analysis (DMTA) was performed using a Gabo Qualimetrer Explexor 25N under the tension configuration. The complex modulus and loss factor of each rectangular specimen ($55 \times 10 \times 2 \text{ mm}^3$) were determined at a constant frequency of 10 Hz, raising the temperature from -140 to 250 °C at a heating rate of 1~2 °C/min.

3.4 Differential Scanning Calorimetry

Thermo-grams of the materials were carried out on a DSC821 apparatus (METTLER TOLEDO). All tests were performed in nitrogen atmosphere with a sample mass of about 10~18 mg. The scanning rate was 10 °C/min. To completely eliminate thermal history, the sample was held at 300 °C for 3 min, and then cooled to 0 °C at the same scanning rate. For the semicrystalline polymer composites, the crystallinity X_c was calculated according to equation (3.14):

$$X_c = \frac{\Delta H_m}{\Delta H_m^0(1 - w_t)} \quad (3.14)$$

where ΔH_m is the specific melting heat of the specimen, ΔH_m^0 is the theoretical specific melting heat of 100% crystalline polymer, which is taken to be 195 J/g and 209 J/g for PA66 and iPP, respectively. w_t is the weight fraction of nanoparticles.

3.5 Microstructure Characterization

3.5.1 Scanning Electron Microscopy

After mechanical tests the fracture surfaces of the materials were examined by scanning electron microscopy (SEM, JEOL 5400). Prior to observation, the fracture surfaces were sputtered with Pt/Pd alloy for 150 sec. Some higher resolution micrographs were taken from the Institute of Physics, Chinese Academy Sciences, by a SEM HITACHI S5200.

3.5.2 Transmission Electron Microscopy

The dispersion effect of nanofillers was examined by transmission electron microscopy (TEM, FEI Tecnai G 20). Before observation, ultrathin sections of several tens nanometers were cut using an ultramicrotome machine.

3.5.3 Atomic Force Microscopy

The smooth fracture surfaces of some specimens were also examined by atomic force microscopy (AFM, Nanoscope IIIa, Digital Instruments Co.) using a tapping mode to obtain more detailed information. The scanning rate was 0.5003 Hz.

3.5.4 Laserprofilometry

The topography of epoxy-based nanocomposites was detected by a laserprofilometer (UBM Messtechnik) to better understand the toughening mechanism of nanoparticles. The image analysis was performed according to DIN 4768.

4 In situ Epoxy Nanocomposites

Owing to the high degree of cross-linking between polymer chains, epoxy resins usually exhibit high tensile modulus and strength, high creep resistance and excellent wear resistance. These outstanding mechanical properties, together with good processability and moderate cost, have led to the wide use of epoxy resins in engineering applications, such as structural components, coating and adhesives. On the other hand, the high cross-linking structure also makes epoxy resins inherently brittle, with poor damage tolerance, which greatly limits their broad utility. Improving the fracture toughness of epoxy resins is an important issue. Among various modification methods, using an additional phase (e.g. rubber particles, organic thermoplastic particles, rigid micro-particles, etc.) to toughen epoxy resins and other polymers has become a common practice [23,107-112]. It is well known that addition of rubber particles can dramatically increase the fracture toughness of epoxy resins, but at cost to the mechanical and thermal properties of the pristine matrix. Rigid inorganic particles, the size of which ranges from micron scale to nanoscale, may overcome such defects. They can improve the stiffness and toughness of epoxy resin simultaneously, even though the improvement in fracture toughness is not as pronounced as that in rubber toughened epoxy systems. Compared to micro-particles, nanoparticles have several unique features. Firstly, they have a much higher specific surface area, which promotes stress transfer from matrix to nanoparticles. Some studies have reported that nanoparticles could increase the modulus of composites more dramatically than micro-particles [113,114], suggesting that the high particle-matrix interphase may play a key role in stiffening polymer matrices. Secondly, the loading of nanoparticles in composites is usually found to be much lower than that of micro-particles (10~40 vol.%, typical for micro-particles). Therefore, many intrinsic merits of epoxy resin, such as light weight, ease of process as well as transparency, need not be sacrificed with the addition of the nanoparticles.

In this section, various mechanical properties of *in situ* formed epoxy nanocomposites (two types: cycloaliphatic and bisphenol-F, see section 3.1) were systematically investigated in order to understand the structure-property relationship

of the nanocomposites. The stiffening and toughening mechanisms of the nanoparticles were considered based on the experimental data and related fractographs.

4.1 Cycloaliphatic Epoxy Nanocomposites

4.1.1 Microstructure

TEM inspection as shown in Figure 4.1 showed almost perfect nanoparticle dispersion in the epoxy resins even at very high filler content. Optical transparency is maintained up to filler content of 14 vol.%, which is due to the minimized reduction of light transmission by the well-dispersed nanoparticles. The average diameter of the nanosilica particles is about 25 nm.

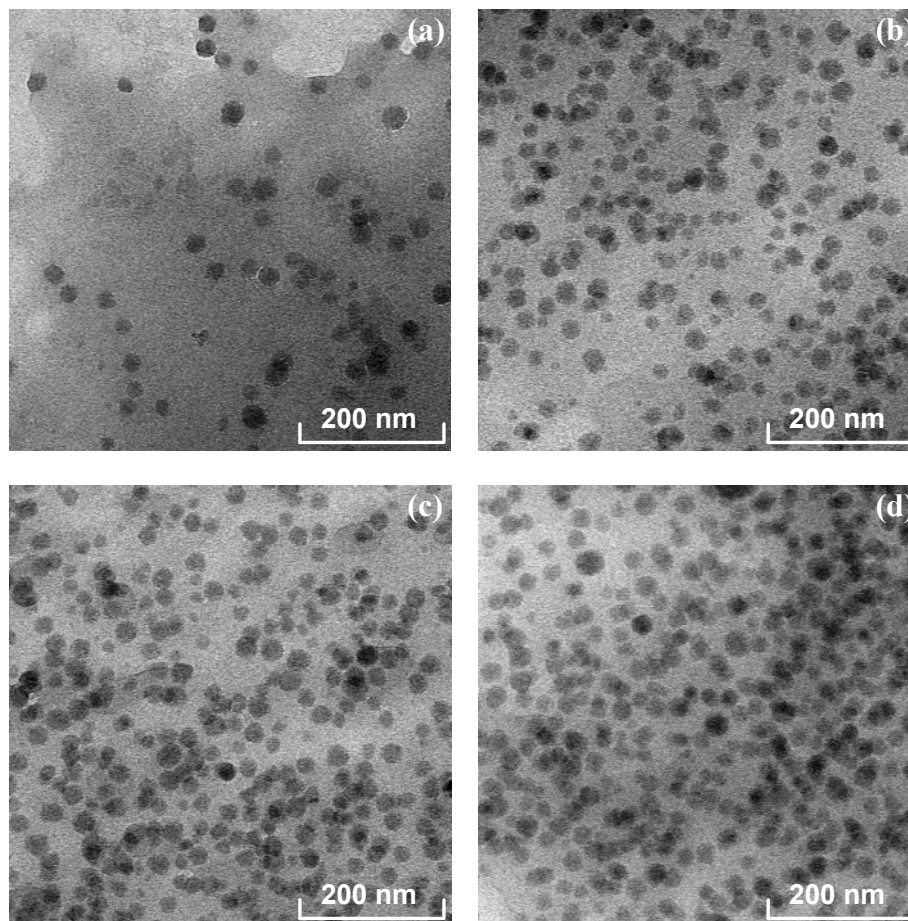


Figure 4.1: Transmission electron microscopy (TEM) inspection of (a) 3 vol.%, (b) 6 vol.%, (c) 12 vol.% and (d) 14 vol.% silica/ cycloaliphatic type nanocomposites,

exhibiting excellent nanoparticle dispersion even at rather high filler content.

The homogeneous particle distribution is also confirmed by high resolution SEM image, as shown in Figure 4.2. With the exception of few particles, an extremely narrow distribution of particle size is achieved through the *in situ* sol-gel method.

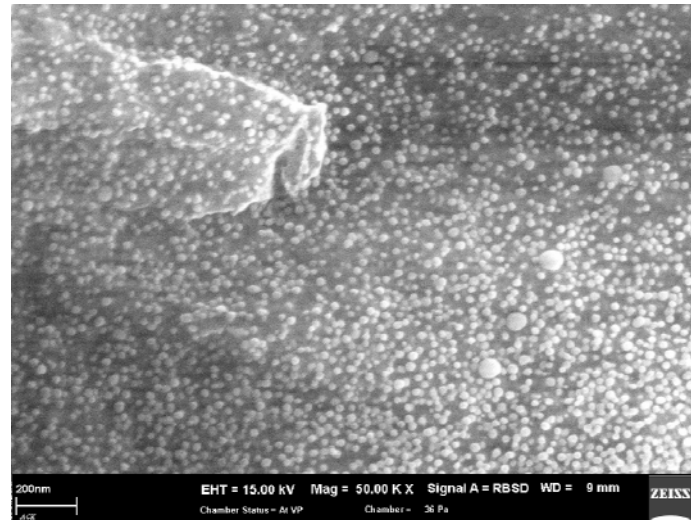


Figure 4.2: High resolution SEM image showing excellent distribution of nanoparticles. (Courtesy: H. Giertzsch, 2006)

4.1.2 Dynamic Mechanical Thermal Analysis

Figure 4.3 a shows the traces of DMTA of the cycloaliphatic type nanocomposites. Two obvious features can be detected. Firstly, the addition of nanosilica slightly enhances the damping values of the epoxy resin from cryogenic temperatures up to glass transition temperatures (T_g), and the relaxation temperatures are obviously changed. The α -, β - relaxation temperatures as a function of nanosilica content are given in Figure 4.3 b, measured by both DMTA and DSC. Decline in the T_g of epoxy nanocomposites has been reported by other researchers [115]. A plasticizing effect of colloidal silica is believed to contribute to this phenomenon. Another possible reason is that the epoxy resin in the nanocomposites might not be completely cured due to the influence of nanoparticles. However, a contrary tendency is observed on the second glass transition temperature (T_β) in our case, and the mechanism is still not clear at present. Secondly, the dynamic complex modulus is significantly improved with increasing nanosilica content. Comparatively, for a given nanosilica

content, the stiffening effect is seemingly more pronounced at lower test temperatures as shown in Figure 4.3 a. This phenomenon may be attributed to the mismatch in the coefficient of thermal expansion (CTE) between the matrix and particles. According to thermal mechanical analysis, the CTE of the current epoxy resin is $6.2 \times 10^{-5} \text{ K}^{-1}$, while the value of bulk silica is about $5.5 \times 10^{-7} \text{ K}^{-1}$ [116]. Due to the great difference in their CTEs, a residual compressive stress between two phases should exist, which may provide additional stress transfer under loading. It is reasonable to infer that the lower temperature will lead to a higher residual compressive stress, thus allowing better stress transfer from matrix to filler. Accordingly, a notable stiffening effect is obtained at lower temperatures.

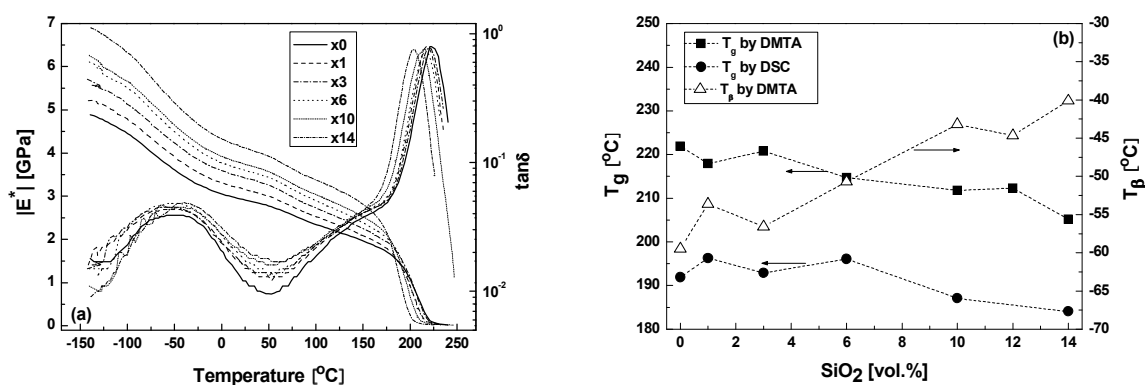


Figure 4.3: Temperature dependence of dynamic mechanical properties of cycloaliphatic type nanocomposites: (a) complex modulus and damping, and (b) the first and second glass transition temperatures (T_g and T_β) as a function of nanosilica volume fraction.

It can be noted from the above experimental results that the nanoparticles produce obvious reinforcing effects even at low volume content. This is usually ascribed to the huge surface area of the nanoparticles, which can to some extent affect the properties of the nanocomposites by forming a non-negligible interphase layer between particle and matrix. An "effective volume fraction" was empirically introduced for quantitative characterization and comparison of the interphase properties of particulate filled polymers on a micron scale [117-119]. According to this concept, some amount of surrounding polymers (interphase) are immobilized due to interfacial binding, which results in an increased effective region for the particles. The "effective

volume fraction", φ_e , can be estimated by the following equation, assuming that the immobilized polymer parts do not contribute to energy loss [3]:

$$\frac{E_c''}{E_m''} = (1 - \varphi_e)^{-1} \quad (4.1)$$

where E_c'' and E_m'' are the relative loss moduli of the composite and the matrix, respectively, and φ_e is related to the effective thickness of the interfacial region, ΔR , defined by

$$\varphi_e = \left(1 + \frac{\Delta R}{R}\right)^3 \varphi_p \quad (4.2)$$

in which R is the radius of the spherical particle, and φ_p is the actual nanoparticle volume fraction.

This approach has also recently been adopted for the nanocomposites [4-6]. In the present case, the temperature dependent "effective volume fraction" calculated according to equation 4.1 is plotted in Figure 4.4 a. It is clear that the φ_e is not constant, but varies with increasing temperature up to about 180 °C. When temperature further increases, the influence of glass transition may result in $E_c'' < E_m''$. Consequently, φ_e decreases sharply and even becomes negative. Therefore the discussion of φ_e near and above T_g seems to be meaningless, at least in the present case. Nevertheless, a clear tendency is easily found that the higher filler fraction always relates to higher φ_e . For a comparison purpose, an average value of φ_e below 150 °C is given in Figure 4.4 b for each material against the actual nanoparticle volume fraction, φ_p . Accordingly, ΔR can be estimated by equation 4.2, which is plotted additionally in Figure 4.4 b. It can be seen that in general the φ_e is much higher than the corresponding φ_p . A φ_p with 1 vol.% nanoparticles matches a φ_e value of more than 20 vol.% under this assumption. Zhang et al [5] reported similar results that the "stress volume fraction" (identical with the "effective volume fraction" in our opinion) ranged between 37~87 vol.% for 0.39~4.68 vol.% grafted nanosilica (7 nm) in a polypropylene matrix. Kojima et al [6] also found that the restriction of polymer chain mobility by nanoclay contributed finally to the improved tensile modulus. In our case, the effective thickness of the interfacial region ΔR ranges from 2.79 to 10.55

nm, which is approximately consistent with the results of 3.6~22.4 nm of nylon 11/silica (7~12 nm) nanocomposites studied by Petrovicova et al [4]. The ratio of $\Delta R/R$ in the present study is in the range of 0.22~0.84, which is much larger than that of micro-particle-filled composites, only ranging between 0.02~0.07 (estimated in the present work) [118]. Nanoparticles seem to be more "effective" in reinforcing polymers due to the particle-matrix interactions. Interestingly, ΔR is found to decrease monotonously with increasing particle content in Figure 4.4 b, suggesting a reduced influence region of a nanoparticle at higher particle loadings. This can be explained due to some overlaps and offsets of the neighbouring stress fields at increased particle content. It seems to us that the "effective volume fraction" could provide some clues to the significant property improvements of polymer matrix at relatively low nanoparticle content by considering the influence of interphase regions. However, no further experimental evidence can be applied to support the key assumption of this approach that nanoparticle/polymer interphase does not contribute to energy loss, which is simply adopted from the case of micro-particles. It is our opinion that this assumption may bring about an overvalued size of the interphase region of a nanoparticle. More discussion about the interphase is presented in the following sections for the present situation of much reduced interparticle distance at relatively high nanosilica content.

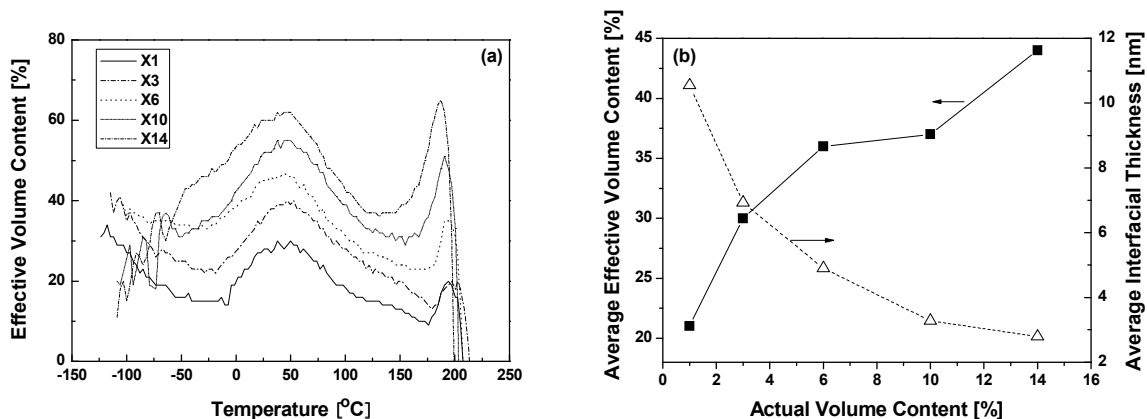


Figure 4.4: Evaluation of nanosilica-matrix interphase: (a) temperature dependence of effective volume content and (b) average effective volume content and average interfacial thickness of nanoparticles.

4.1.3 Various Mechanical Properties

Although this work is mainly concerned with the toughening effects of nanoparticles in epoxy resin, it is necessary to measure the basic mechanical properties such as modulus, strength and microhardness, because some of these parameters will be used to determine the fracture parameters (e.g., G_{IC} , radius of plastic zone).

Improvements in the mechanical properties of nanosilica/epoxy composites were investigated systematically. The results are summarized in Table 4.1. Figure 4.5 shows typical stress-strain curves measured by three-point-bending tests, and typical load-displacement curves measured by compact tension (CT) specimens. In Figure 4.5 a it can be seen that both neat epoxy and nanocomposites were broken in a brittle fashion, and no obvious deflections can be detected. The reduced elongation at break of the nanocomposites suggests that nanosilica can suppress macromolecular mobility to some extent. In Figure 4.5 b, despite the very sharp natural pre-cracks achieved in the specimens, crack propagation occurred entirely in a controlled manner during the whole measurement period of each specimen, i.e. no abrupt fracture took place once the crack started to propagate at the maximum load. The maximum load is remarkably improved by the addition of nanosilica, which therefore dramatically enhances the fracture toughness of the nanocomposites. Epoxy filled with 14 vol.% nanosilica shows the highest maximum load and the largest area under the load-displacement curve. It is also clear, in the present case, that the greater the nanosilica content, the higher the fracture toughness of the nanocomposites.

Table 4.1: Mechanical properties of cycloaliphatic type nanocomposites

Sample code	Three-point-bending			Tension	Micro-hardness [MPa]	Impact energy [kJ/m ²]	K_{IC} [MPa·m ^{1/2}]	G_{IC} [J/m ²]
	E_f [GPa]	σ_B [MPa]	ϵ_B [%]	E [GPa]				
X0	3.05	129.6	4.55	3.27	201.1	25.6	0.42	46.5
X1	3.23	121.9	3.86	3.31	209.9	28.8	0.47	58.3
X3	3.36	120.5	3.60	3.60	211.9	31.4	0.55	72.6
X6	3.43	133.1	4.08	3.71	221.7	30.9	0.61	87.4
X10	3.90	133.9	3.67	3.87	232.5	30.0	0.66	98.8
X12	4.08	120.1	3.01	3.77	239.7	24.4	0.73	123.1
X14	4.18	134.7	3.42	4.19	238.4	23.7	0.74	115.1

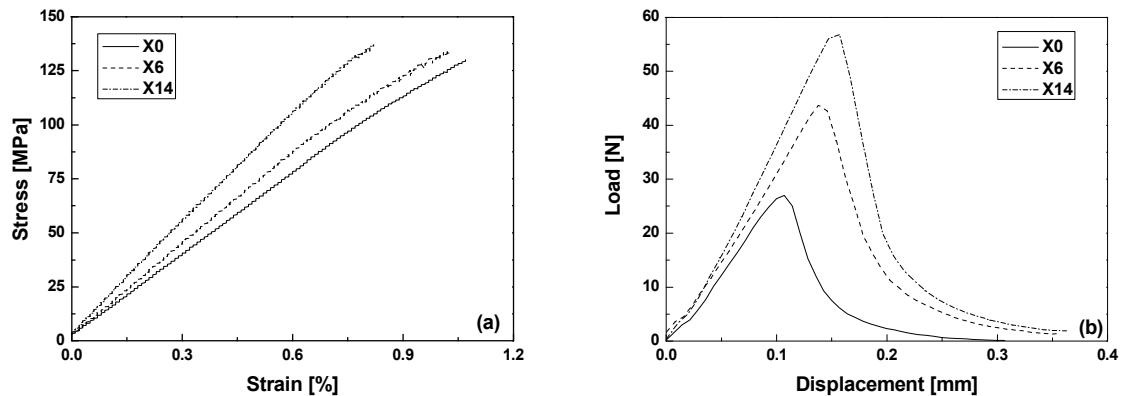


Figure 4.5: Typical load-displacement curves of cycloaliphatic type nanocomposites: (a) three-point-bending and (b) compact tension test.

Figure 4.6 summarizes the relative improvements in various mechanical properties of cycloaliphatic type nanocomposites. It is clear that the flexural modulus (E_f), micro-hardness (HU) and fracture toughness (K_{IC}) are all monotonously improved with increasing nanosilica volume content. 14 vol.% silica/epoxy presents the highest improvements in micro-hardness, modulus and fracture toughness by about 19%, 37% and 78%, respectively, compared to the neat epoxy. For unnotched Charpy impact resistance, a peak value is found at a very low nanosilica loading of 3 vol.% (performed about 23% increase to the impact resistance). However, flexural strength does not show any apparent improvement. These results confirm that the

homogeneously distributed nanoparticles can improve stiffness and toughness of epoxy simultaneously. Moreover, the toughening effect of nanosilica in the epoxy matrix is more pronounced in this study.

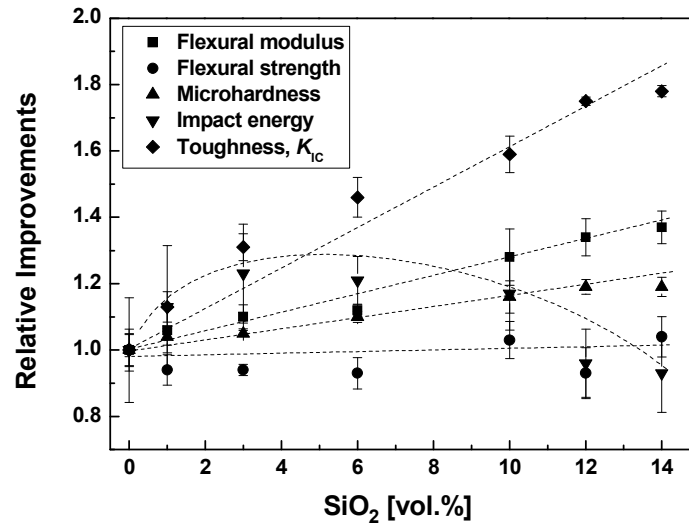


Figure 4.6: Relative improvement in various mechanical properties as a function of nanosilica volume fraction of cycloaliphatic epoxy nanocomposites.

4.1.4 Fractography

4.1.4.1 Three-Point-Bending Samples

Scanning electron microscopy (SEM) fractographs of three-point-bending specimens can reflect some of the fracture mechanisms of these nanocomposites. Figure 4.7 a shows the fracture surface of the neat epoxy, with ribbons and fracture steps, and rather smooth areas in between, as is typical for the brittle fracture. However, the addition of nanosilica yields a much rougher fracture surface, as shown in Figures 4.7 b and 4.7 c, of 1 and 10 vol.% nanosilica content, respectively. Numerous dimples with irregular shapes are observed. Interestingly, the density of these dimples increase with the increase of the nanosilica volume fraction. A close-up of one such dimple in Figure 4.7 d can give some ideas as to their formation. Although nanosilica particles are almost perfectly dispersed in the epoxy matrix, there are still some regions where several individual nanoparticles are quite close to each other. These nanoparticle-rich regions may not be fully cured during the curing procedure, causing

stress concentration and creating weak sites, and further triggering the formation of dimples under load. In addition, the debonding of nanoparticles from the matrix seems not as serious as that in micron-sized particle filled epoxy resin. This may be evidence of the good particle-matrix interphase. In addition, the debonding process depends strongly on particle size. As particle size decreases, the critical stress necessary to cause debonding increases, resulting in greater difficulty in debonding [120]. Occasionally, cavitations after particle debonding can be found in the middle of the dimples, as indicated by the white arrow in Figure 4.7 d. It is evident that the size of the cavitation is larger than the single nanoparticle size measured by TEM (Figure 4.1). This suggests that failure might not occur directly at the filler-matrix itself, but instead in the polymer around the particles, i.e., cohesive debonding occurs during fracture.

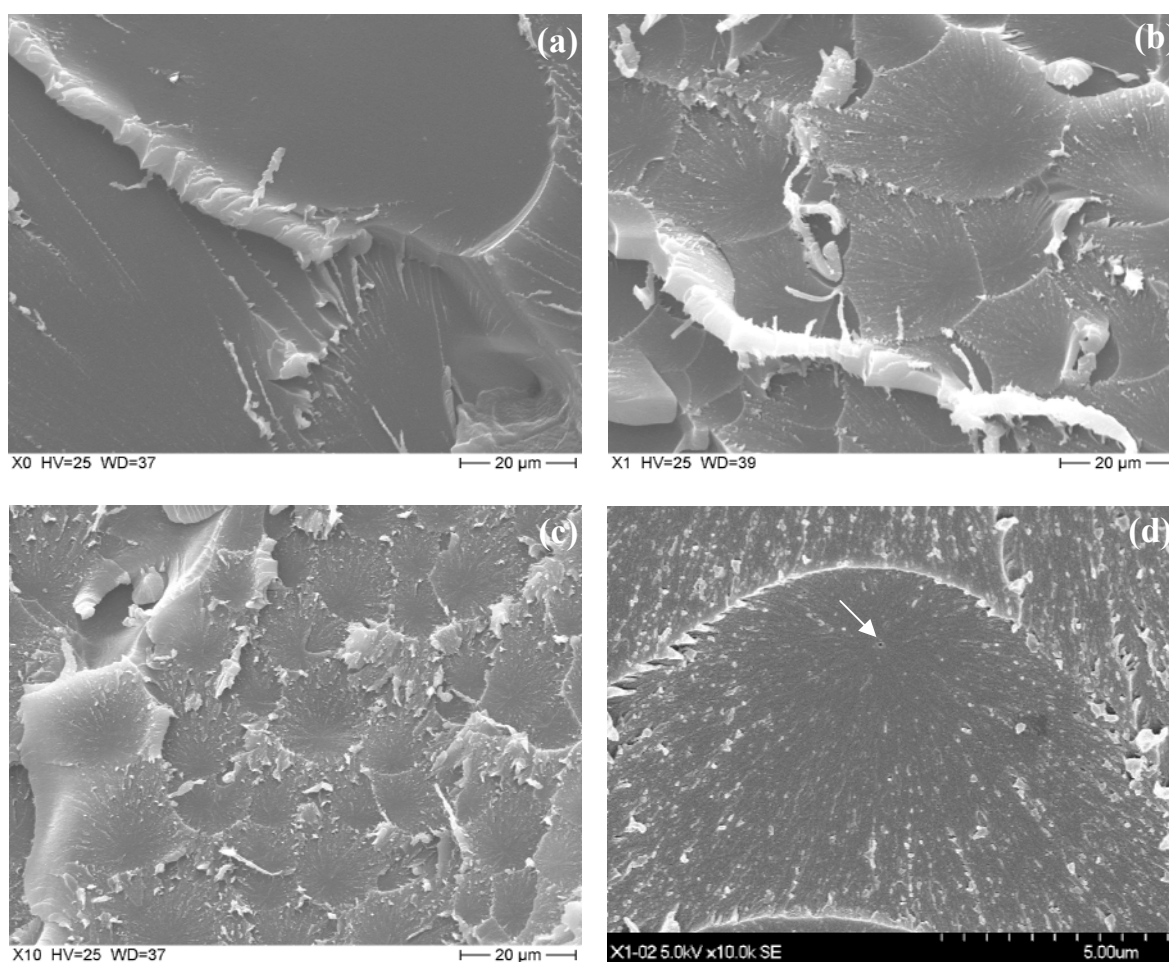


Figure 4.7: Lower magnification SEM fractographs of cycloaliphatic type nanocomposites from three-point-bending tests: (a) neat matrix, (b) 1 vol.% nanosilica, (c) 10 vol.% nanosilica, and (d) close-up of a dimple.

Comparison between the higher-magnification fractographs taken from three-point-bending in Figures 4.8 b and 4.8 c (1 and 10 vol.% nanoparticle content, respectively) and neat epoxy in Figure 4.8 a are very interesting. Numerous spheres can be found in these fractographs. Their amount is dependent on the nanosilica volume fraction. The size of these spheres is in a range of about 30~80 nm (a few are even larger), which means that the interfacial thickness is in a range of 2.5~22.5 nm. This value agrees well with the results estimated by DMTA (2.79 ~10.55 nm, see section 4.1.2). Based on the above results, it could be concluded that the nanoparticle-matrix bond is really strong. The strong interface is probably attributable to surface modification of the nanoparticles occurring during the sol-gel process. This structure formed during fracture can be depicted as a core-shell structure of a nanosilica particle relatively strongly coated with polymer chains, as illustrated in Figure 4.9 [121]. These core-shell structures may construct the unique morphology of fracture surfaces, finally favouring the mechanical performance of the materials.

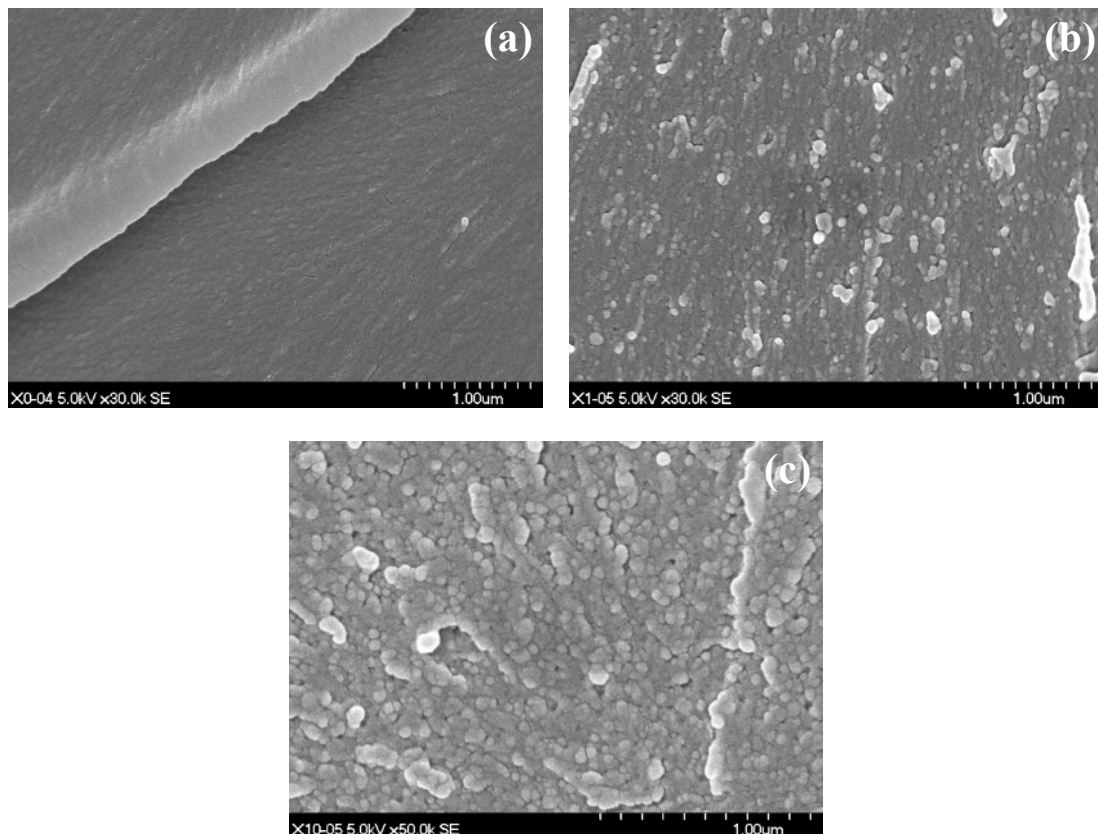


Figure 4.8: Higher-magnification SEM fractographs of epoxy and nanocomposites from three-point-bending tests: (a) neat epoxy, (b) 1 vol.% nanosilica and (c) 10 vol.% nanosilica.

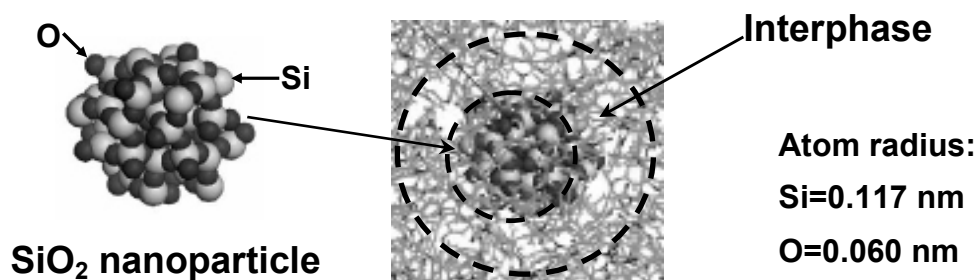


Figure 4.9: Illustration of the core-shell structure of a silica nanoparticle coated with polymer chains [121].

From another angle, the improvements in the mechanical properties of nanocomposites with the core-shell structures could be explained by the percolation theory, which is schematically illustrated in Figure 4.10. As seen, by increasing the nanoparticle content, the interparticle distance will be gradually reduced. At higher filler content, the interphase around the nanoparticles can interconnect and form a three-dimensional physical network throughout the matrix, thereby becoming the key factor in determining the performance of the nanocomposites. If this theory holds, a critical particle content (or critical interparticle distance) should exist, above which the mechanical performance of the nanocomposites will be controlled by the networks. Actually, this would be confirmed by Figure 4.11, the correlation between interparticle distance, τ , and mechanical performance. Here, the interparticle distance was estimated using equation (4.3), assuming cubic arrangement of particles in the materials studied.

$$\tau = d \left[\left(\frac{\pi}{6\phi_p} \right)^{1/3} - 1 \right] \quad (4.3)$$

As seen, at the nanosilica content of c.a. 6 vol.%, i.e. the interparticle distance is approximately equal to the particle diameter, and it is where the obvious turning point for the various mechanical properties (stiffness, toughness and micro-hardness) can be observed.

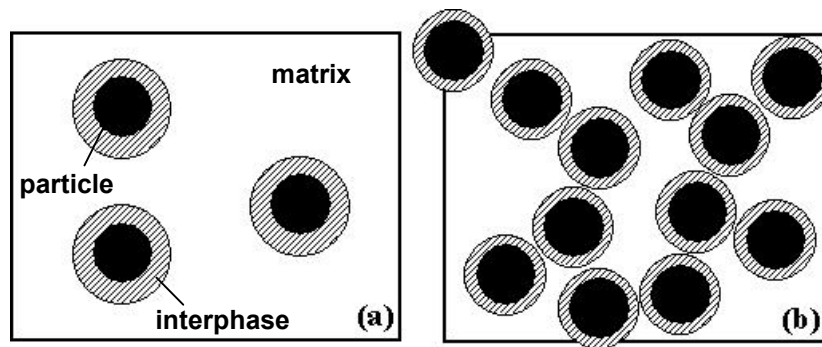


Figure 4.10: Schematic illustration of percolation theory: (a) the particles are disconnected at lower volume content; (b) the percolation state at critical particle content (critical interparticle distance).

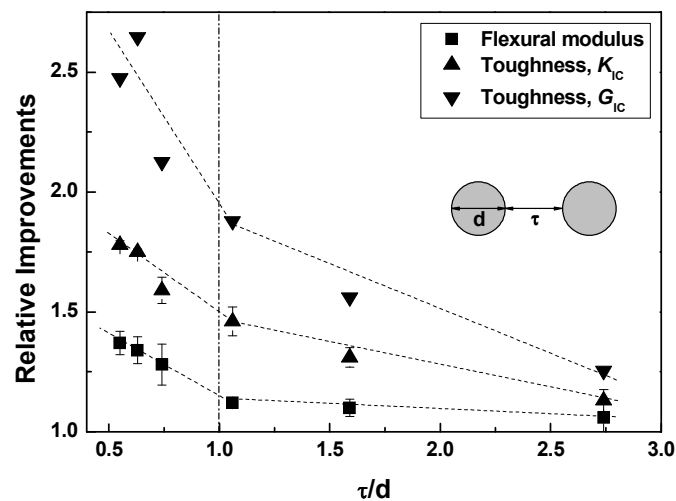


Figure 4.11: Correlations between interparticle distance and mechanical properties of cycloaliphatic epoxy nanocomposites.

4.1.4.2 Impact Samples

Further characterization of a fracture surface is shown in Figure 4.12, an AFM fractograph obtained after a Charpy impact test of a specimen with 10 vol.% nanosilica. Primary nanosilica particles on the surface can be detected also (some examples indicated by arrows). Compared to the average diameter of 25 nm of the nanoparticles obtained in TEM images (Figure 4.1), the greater mean size of these

particles can be recognized with image analysis software (Nano Scope III V5). The arrow-marked particles have an average diameter of c.a. 50 nm. This result confirms the core-shell structures and good particle-matrix adhesion discussed earlier. Hence we can infer that it is the core-shell structure rather than the naked nanoparticle that plays the key role in deformation and fracture of the nanocomposites.

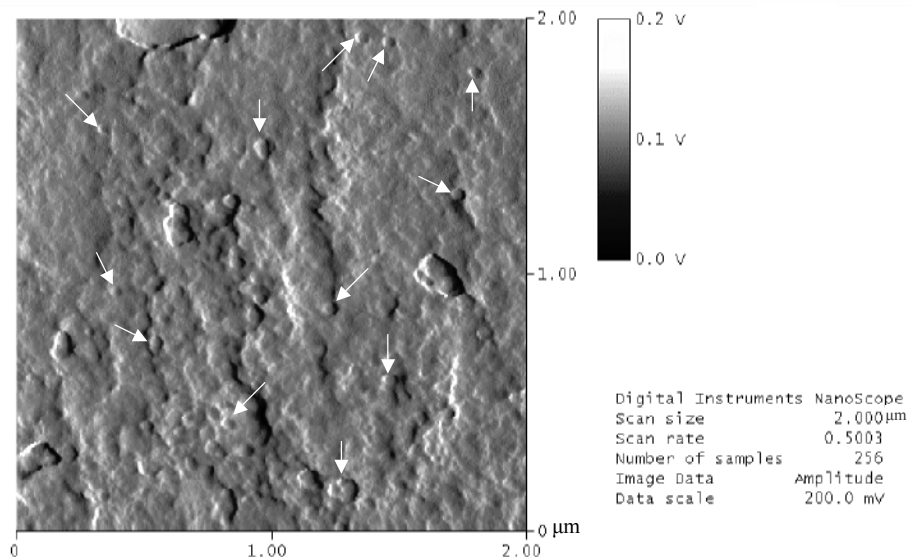


Figure 4.12: Atomic force microscopy (AFM) fractograph of cycloaliphatic type nanocomposite (10 vol.% nanosilica) after Charpy impact test. The arrow-marked particles are of a larger size than naked ones, suggesting the presence of a core-shell structure.

4.1.4.3 CT Samples

Fractographs from CT specimens can supply some information about the toughening mechanisms of the nanoparticles. Figure 4.13 shows the fracture patterns of the neat epoxy (Figures 4.13 a and 4.13 b) and 14 vol.% nanosilica/epoxy (Figures 4.13 c and 4.13 d) obtained near crack tips and in the middle zones of fracture surfaces. For both materials, river-like lines are formed near the crack tips and along crack propagation zones. Near the crack tips (crack initiation region) the river-like lines are dense, and they then tend to converge along the crack propagation, suggesting that less strain energy is acquired. Comparatively, much denser river-like lines can be observed in both crack initiation and crack propagation regions of the

nanocomposites, which may be associated with crack tip blunting in the initiation stage and high-energy dissipation during crack propagation. These river-like lines in nanocomposites are not straight but are to some extent deflected, which is probably due to the crack bowing and pinning effects of nanoparticles [108,122]. Moreover, some of these river-like lines are not continuous, implying that the crack fronts are often trapped through crack-particle interactions. In addition, some cavitations of hyperbolic shape are formed during crack propagation (marked by a rectangle in Figure 4.13 c), which presumably benefit fracture toughness by relieving stress intensity around the crack tip.

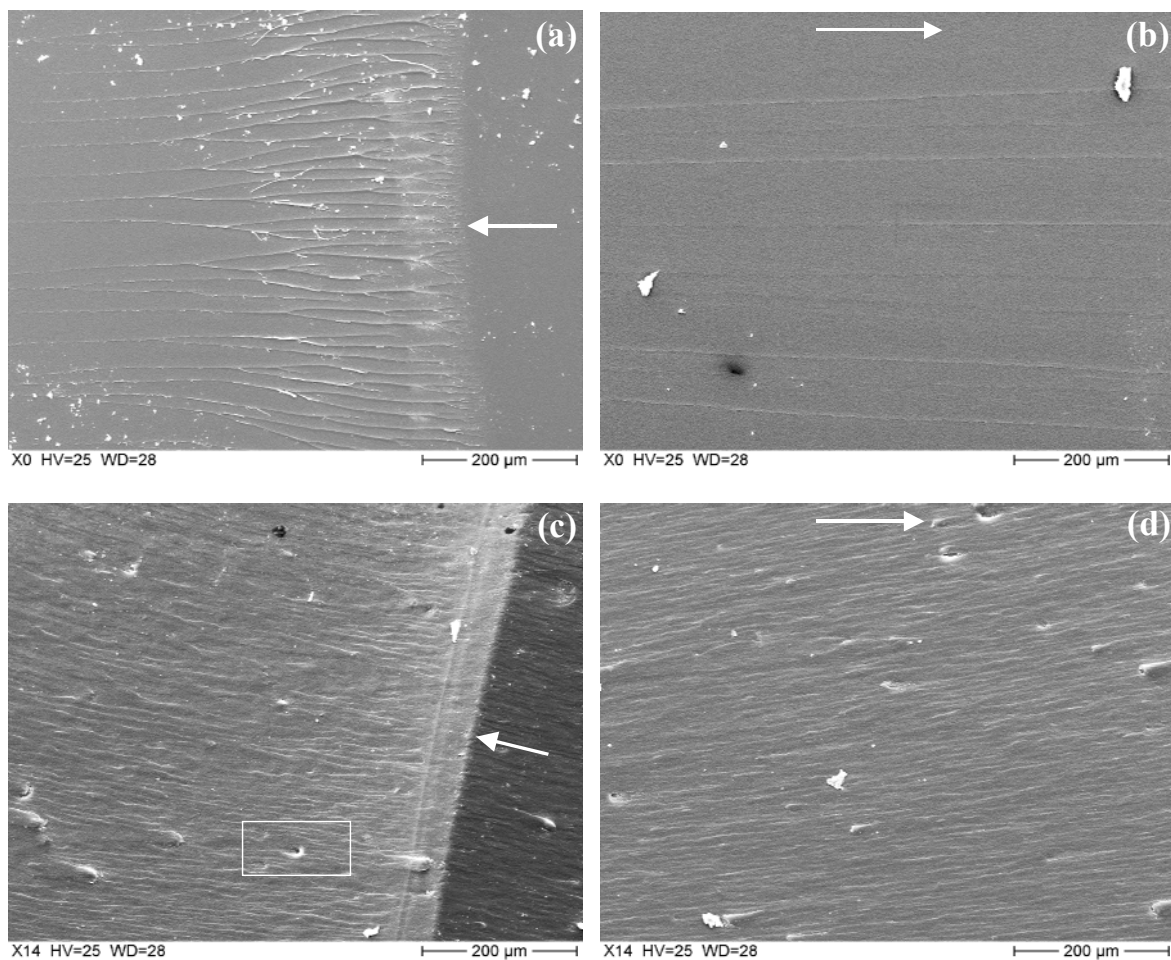


Figure 4.13: SEM fractographs of cycloaliphatic type composites taken from CT tests. The arrows represent the crack propagation directions: (a) crack initiation region for neat matrix, (b) crack propagation region for neat matrix, (c) crack initiation region for 14 vol.% nanosilica and (d) crack propagation region for 14 vol.% nanosilica.

4.2 Bisphenol-F Epoxy Nanocomposites

4.2.1 Microstructure

As with the cycloaliphatic type nanocomposites, the nanosilica particles in the bisphenol-F nanocomposites show excellent distribution, and an agglomerate-free state can be obtained even at highest particle volume fraction, as shown in TEM images (Figure 4.14). The average diameter measured with TEM is about 25 nm.

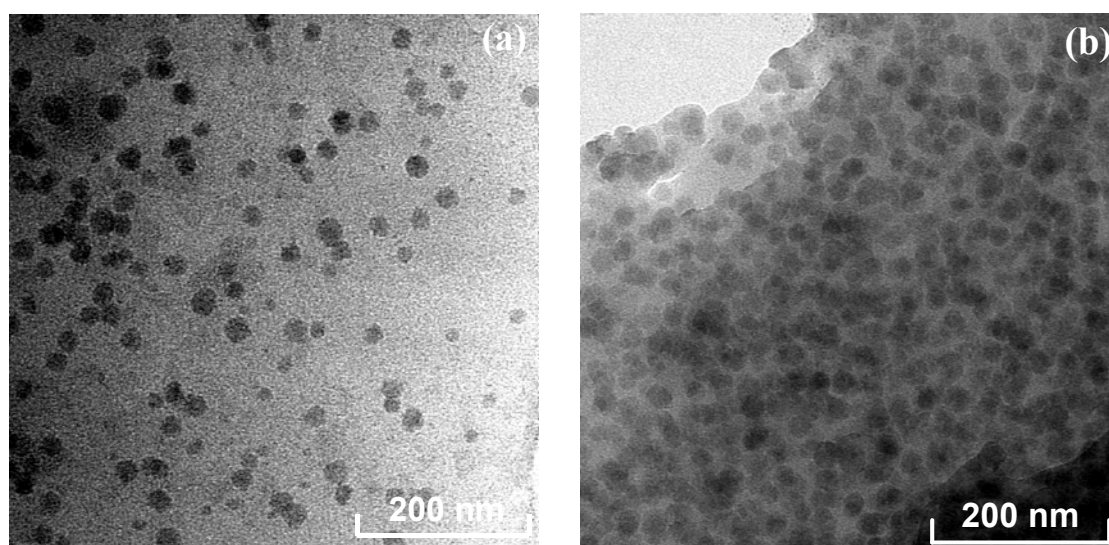


Figure 4.14: Transmission electron microscopy (TEM) inspection of (a) 3 vol.%, (b) 15 vol.% silica/epoxy nanocomposites, exhibiting excellent nanoparticle dispersion even at rather high filler content.

4.2.2 Dynamic Mechanical Thermal Analysis

Figure 4.15 shows DMTA curves of the bisphenol-F nanocomposites. Here, the testing temperature ranged from room temperature to 200 °C. As expected, the complex modulus of the epoxy resin is obviously increased after the addition of nanosilica particles. However, damping behaviours are not significantly affected by the nanoparticles. The decline in T_g can be confirmed by both DMTA and DSC techniques (Figure 4.15 b), the reason of which may arise from the plasticizing effect of colloidal silica particle or incomplete curing of epoxy resin in the particle-rich region, or a combination of both factors. Decline in T_g after incorporation of nanoparticles has also been found in some filled thermoplastic and thermosetting polymer systems

[20,123,124]. On the other hand, although the T_g s obtained by different methods show a similar tendency with change of nanoparticle content, they are not identical. For a given nanoparticle content, the T_g s obtained by DMTA are obviously higher than that obtained by DSC, by about 30 °C. This is because the two techniques used in this study work on different principles of measurement. DSC is based on the heat effect of material whereas DMTA is related to the viscoelastic response of material.

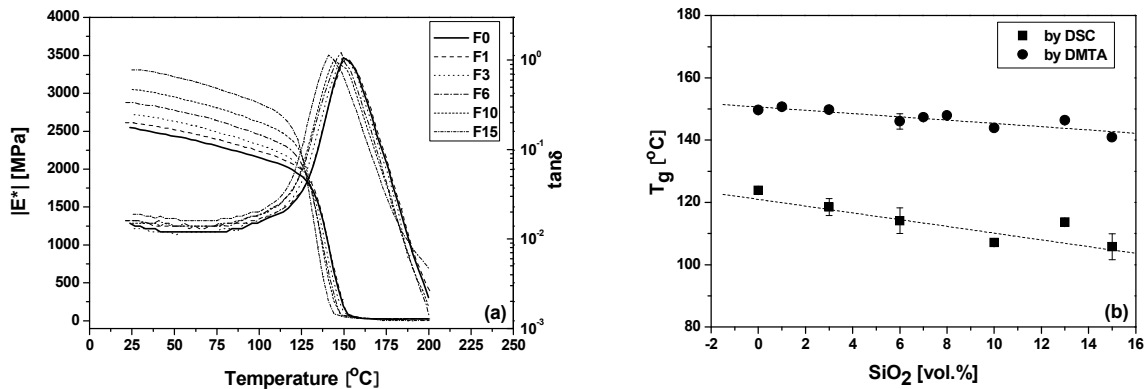


Figure 4.15: Temperature dependence of dynamic mechanical properties of bisphenol-F epoxy nanocomposites: (a) complex modulus and damping and (b) glass transition temperatures (T_g) as a function of nanosilica volume fraction.

From equations (4.1) and (4.2) we can estimate the thickness of the immobilized polymer layer around the nanoparticle surface. The effective volume content and interfacial thickness from room temperature to 130 °C were averaged and plotted against the actual filler content, as shown in Figure 4.16. Where compared with Figure 4.3, a similar tendency can be found. The effective volume content is much higher than the actual particle content, which is likely beneficial to the improvement in tensile modulus of epoxy resin, as discussed. Although some scatter exists, the thickness of the interfacial polymer layer is found to decrease as the nanosilica content increases. This can be explained by the overlaps and offsets of neighbouring stress fields at increased particle content. In addition, an insufficient amount of polymer that should wet the nanoparticles is another possible reason for the reduced thickness of the interfacial layer with increased particle content [125].

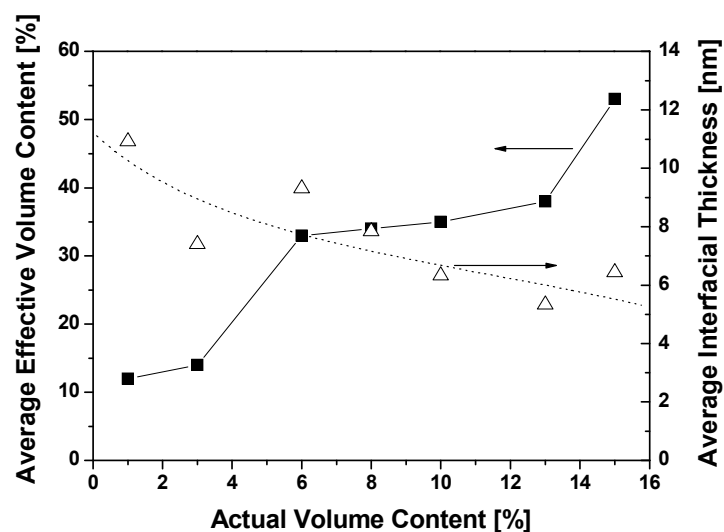


Figure 4.16: Evaluation of nanosilica-matrix interphase: average effective volume content and average interfacial thickness of nanoparticles.

4.2.3 Various Mechanical Properties

4.2.3.1 Tensile Test

The basic mechanical properties of the bisphenol-F nanocomposites were thoroughly investigated at room temperature. Some of the testing was also undertaken at 80 °C. Typical tensile stress-strain curves for the neat epoxy resin and its nanocomposites at 23 and 80 °C are shown in Figure 4.17. At room temperature both filled and unfilled epoxy composites exhibit yielding prior to failure. Comparatively, the bisphenol-F matrix is more ductile than the cycloaliphatic type matrix, as discussed in the preceding section (cf. Figure 4.5). At 80 °C, the bisphenol-F materials show slight necking after yielding.

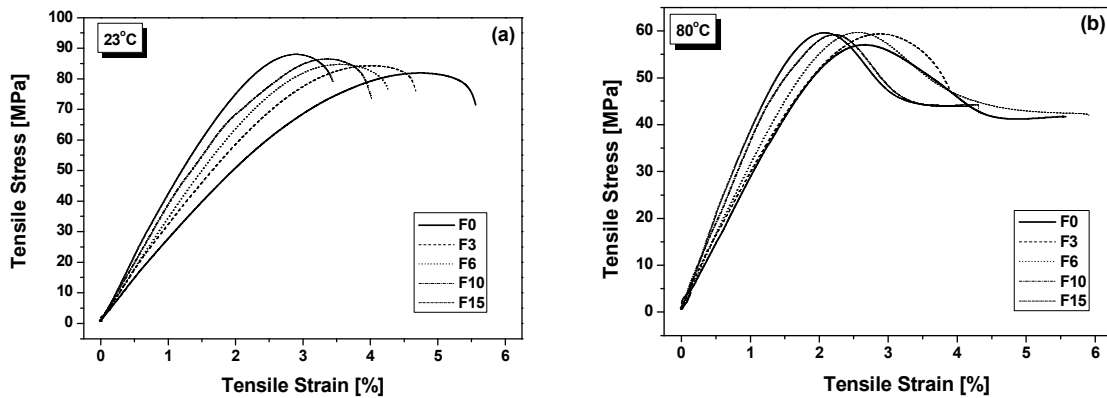
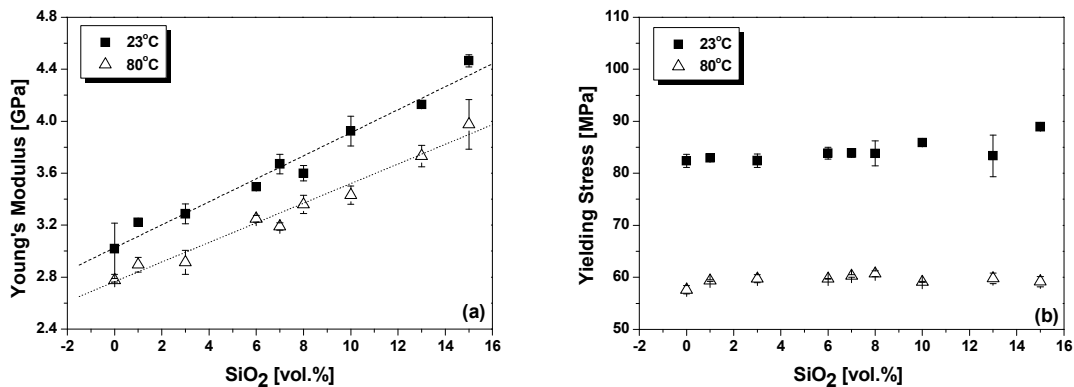


Figure 4.17: Typical tensile stress-strain curves of bisphenol-F epoxy nanocomposites at 23 and 80 °C.

Figure 4.18 summarizes the effects of testing temperature and nanoparticle volume content on the tensile properties of the epoxy resin. Due to the viscoelastic behavior of the polymer matrix, the tensile parameters rely strongly on testing temperatures. At the elevated temperature, the elastic moduli, the yielding stress, and the ultimate tensile stress all decline significantly in comparison with those at room temperature (Figures 4.18 a-c). It seems that the elongation at break is not very sensitive to the testing temperature (Figure 4.18 d), which is probably attributable to the limitation of molecular mobility by the highly crosslinked network of epoxy resins. With regard to the effect of particle content, addition of nanosilica leads to linear increase in the elastic modulus of the epoxy resin with an increase in particle volume content at both temperatures (Figure 4.18 a). However, it has almost no effect on the yielding stress, the ultimate tensile stress and the elongation at break (Figures 4.18 b-d).



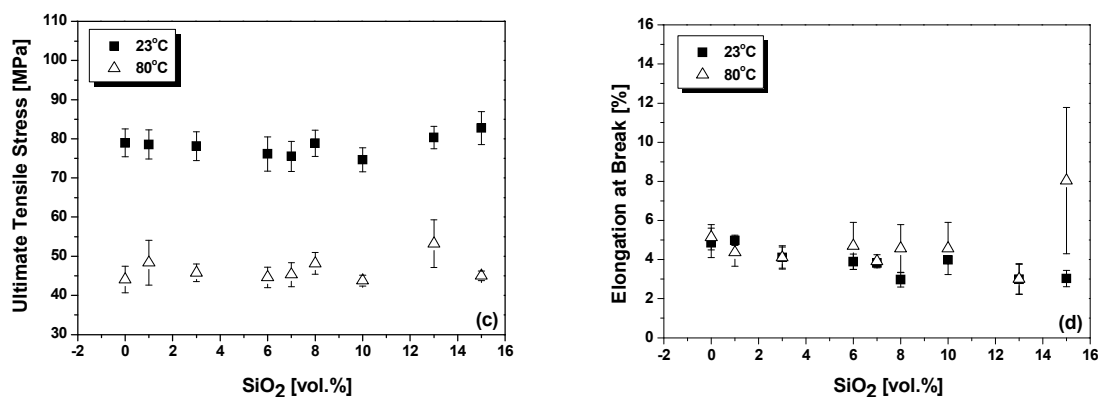


Figure 4.18: Tensile properties of bisphenol-F epoxy nanocomposites at different testing temperatures: (a) tensile modulus, (b) yielding stress (c) ultimate tensile stress and (d) elongation at break.

4.2.3.2 Impact Test

The Charpy impact test is a high-speed fracture test measuring the energy required to break a specimen under bending conditions. The specimens are deformed within a short period and are therefore exposed to high strain rates. The unnotched impact resistance in this study represents the sum of the energy consumed in crack initiation and the subsequent crack propagation process [126]. Figure 4.19 gives the unnotched Charpy impact strength of the bisphenol-F epoxy resin as a function of nanosilica volume content. The impact tests were conducted at room temperature. As evident, there is a broad plateau in this curve. The highest increment of 63% is achieved at particle content of 10 vol.%. With further increase in particle content, the impact resistance tends to decrease; however, the values of impact resistance are still slightly higher than that of the neat resin.

These results obtained in impact tests are analogous to those obtained in the cycloaliphatic type system (cf. Figure 4.6) and also agree with the results obtained by other researchers, who have considered that the decrease in impact strength at high filler content was normally due to particle agglomerates which acted as the structural flaws and caused pre-fracture under load [14,127]. However, in our composites, no agglomerates can be observed even at the highest nanosilica content. Therefore, the

variation of impact strength can possibly be interpreted as follows. Roughly speaking, under impact load an appropriate amount of nanoparticles having strong bonding to polymer matrix can, to some extent, act as crosslinking points, which may transfer the impact energy absorbed by the matrix and make it disperse homogeneously in the composite. Besides, the nanoparticles themselves can hinder crack initiation and propagation through a series of possible energy consuming mechanisms, such as particle debonding, crack front pinning and bowing, as well as crack deflection. Accordingly, impact resistance is improved. However, the high loading of nanoparticles can significantly confine macromolecular mobility, weakening the energy consuming process through matrix deformation and thereby decreasing impact resistance.

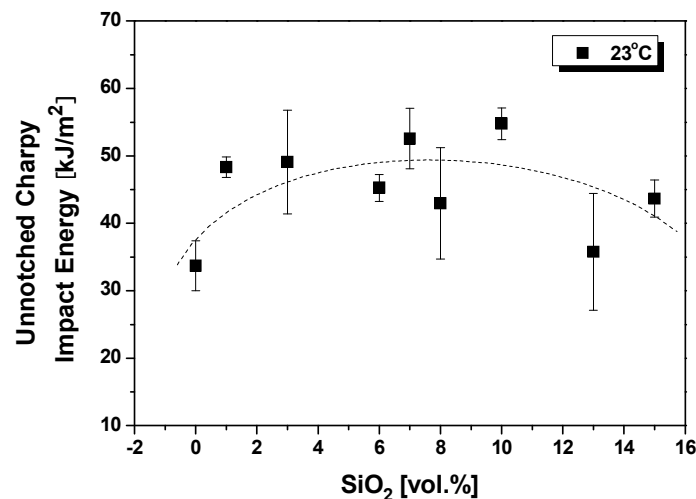


Figure 4.19: Unnotched Charpy impact energy of bisphenol-F epoxy nanocomposites at room temperature.

4.2.3.3 Fracture Test

Figure 4.20 illustrates the typical CT curves of epoxy nanocomposites tested at 23 and 80 °C, respectively. In contrast with the brittle stable crack propagation of cycloaliphatic type samples, a majority of the filled and unfilled bisphenol-F samples exhibit unstable stick-slip crack propagation at both testing temperatures.

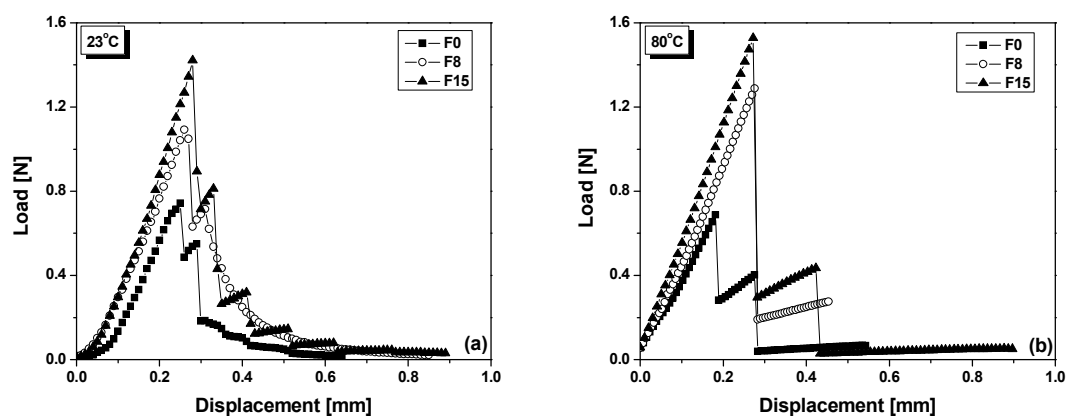


Figure 4.20: Typical CT curves of bisphenol-F epoxy nanocomposites tested at (a) 23 °C and (b) 80 °C.

The stick-slip phenomenon is sometimes observed in epoxy resins [128,129] and in some thermoplastic polymer composites [130,131]. It depends on the intrinsic properties of the matrix and curing agent (for epoxy resin), the specimen geometry, as well as the testing conditions. So far, considerable debate exists in the literature as to the origin of stick-slip crack growth. One common explanation is the crack tip blunting mechanism, proposed by Kinloch and Williams [132]. According to the theory, prior to crack propagation, the crack tip is blunted by localized plastic flow. The blunting can retard crack growth and result in more strain energy being stored in the surrounding material. Up to a critical value, the strain energy allows the crack to grow at an accelerated rate [133]. With crack growth, the excess energy is gradually dissipated for the creation of new fracture surfaces and can be stopped temporarily until a sufficient amount of energy (transferred from the crosshead) is accumulated to re-propagate the crack.

On the basis of this theory, stick-slip crack propagation is favored by a relatively high testing temperature and low strain rate, which facilitate the development of the plastic deformation around the crack tip. By comparing the crack propagation behaviors shown in Figures 4.5 and 4.20, it can be confirmed again that the bisphenol-F epoxy matrix is much more ductile than the cycloaliphatic type matrix. The former exhibits stick-slip crack growth at relatively high strain rate (1 mm/min), whereas the latter has

the stable brittle crack growth even at a very low strain rate (0.1 mm/min). To our surprise, it can be observed from Figure 4.20 b that the amount of stick-slip of epoxy nanocomposites tends to be smaller at 80 °C than that at 23 °C. This does not agree with the analysis described above, i.e., that higher temperatures promote stick-slip behavior of polymer materials. In our opinion, this result can be explained on the assumption that with relatively higher mobility of macromolecules at 80°C, the degree of crack blunting is rather high and a greater amount of excess strain energy can be accumulated around the crack tip. The stored energy may give rise to catastrophic crack propagation, which is difficult to arrest.

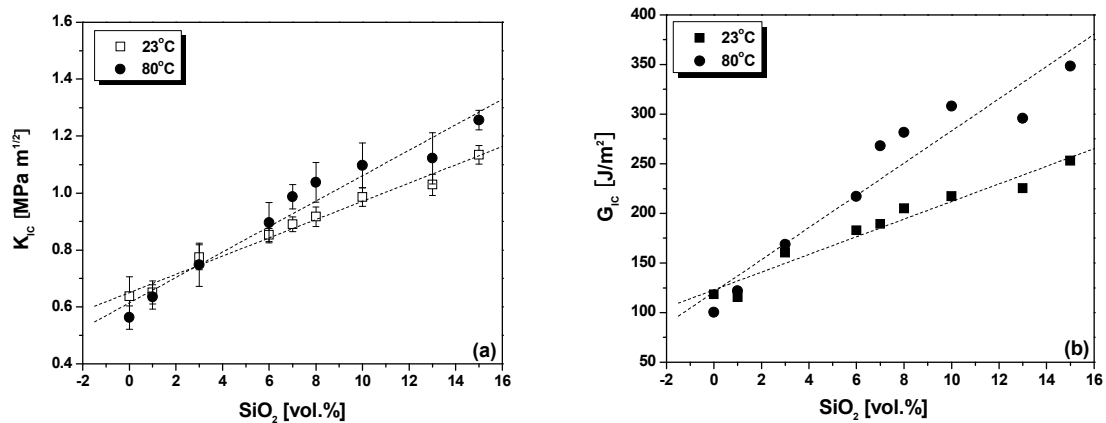


Figure 4.21: Fracture toughness parameters of bisphenol-F nanocomposites as a function of nanosilica volume content: (a) K_{IC} , (b) G_{IC} .

The fracture toughness of bisphenol-F epoxy nanocomposites is characterized by K_{IC} and G_{IC} . The G_{IC} can be calculated from equation 3.4, because the specimen dimension satisfied the criteria of plane-strain state at both testing temperatures. Care should be taken to evaluate the fracture toughness of filled polymers in terms of K_{IC} and G_{IC} , since in some case K_{IC} shows different particle-content dependence from G_{IC} (e.g., rubber particle filled thermosetting resins [134]). This is usually due to the fact that the particle volume content can greatly affect the elastic modulus of the filled polymers, and thereby the K_{IC} values. Therefore, it would be better to describe the fracture property by G_{IC} , because the disturbance of elastic modulus is removed according to equation 3.4.

In the present work, the value of K_{IC} and G_{IC} as a function of nanosilica volume content at 23 and 80 °C is given in Figure 4.21. The K_{IC} and G_{IC} values show roughly similar dependence on the filler content. Both K_{IC} and G_{IC} show approximately linear increases with particle content. With respect to the temperature effect, it is interesting to note that at higher filler content (≥ 3 vol.%), both K_{IC} and G_{IC} are enhanced with increasing temperature whereas the contrary tendency is seen for the neat epoxy resin and the nanocomposites with lower filler content (< 3 vol.%).

4.2.3.4 Brief Summary

In summary, the relative improvements in various mechanical properties measured at 23 and 80 °C are plotted in Figure 4.22 and the experimental data are listed in Table 4.2. It can be observed from Figures 4.22 a, b that addition of nanosilica particles can improve the Young's modulus, micro-hardness and fracture toughness simultaneously without sacrificing ultimate tensile strength. At the appropriate particle content, the unnotched impact resistance is also increased to some extent. Among these improvements in mechanical performance, the toughening effect is the most remarkable and therefore deserves special consideration, which will be discussed in the following sections. On the other hand, the improvements in some mechanical properties (stiffness, micro-hardness and fracture toughness) appear to obey the percolation theory, as shown in Figure 4.22 c,d. As with cycloaliphatic type composites (see section 4.1.4.1), the turning points are found at $\tau \approx d$, independent of testing temperatures. The average diameter of nanoparticles inspected by TEM is 25 nm. This means that the thickness of the interfacial layer is approximately 12.5 nm, which roughly accords with the average interfacial thickness of 9.3 nm (6 vol.% nanosilica) estimated by DMTA (see Figure 4.16).

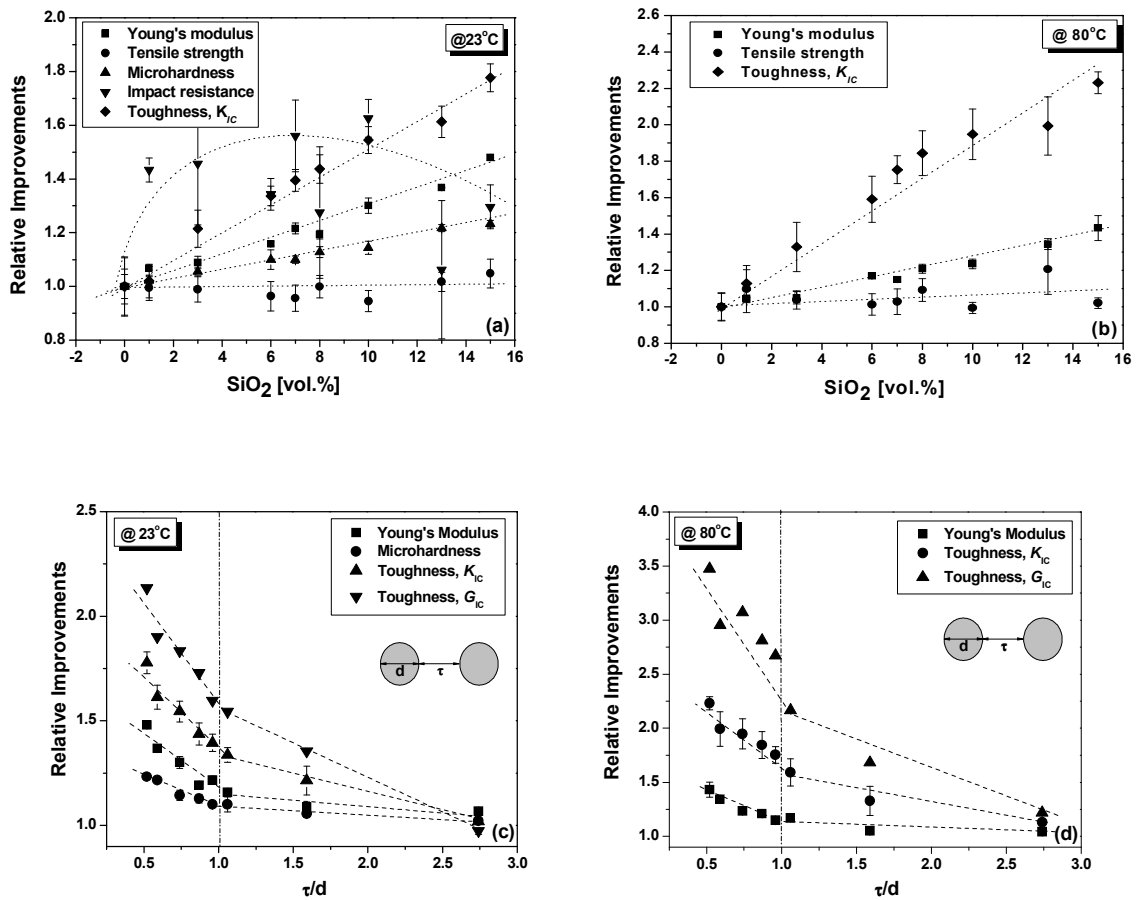


Figure 4.22: Relative improvements of various mechanical properties of bisphenol-F epoxy nanocomposites at two testing temperatures: (a), (b): correlation between relative improvements and nanosilica volume content, (c), (d): correlation between relative improvements and the interparticle distance/particle diameter.

Table 4.2: Mechanical properties of bisphenol-F epoxy nanocomposites

Sample code	Temperature	Tension				Micro-hardness [MPa]	Impact energy [kJ/m ²]	K_{IC} [MPa·m ^{1/2}]	G_{IC} [J/m ²]
		E [GPa]	σ_y [MPa]	σ_B [MPa]	ϵ_B [%]				
F0	23 °C	3.02	82.39	78.98	4.85	176.58	33.7	0.64	118.50
F1		3.22	82.94	78.55	4.98	180.50	48.33	0.65	115.42
F3		3.29	82.43	78.1	4.11	186.39	49.09	0.78	160.57
F6		3.49	83.88	76.15	3.89	194.24	45.27	0.85	182.94
F7		3.67	83.92	75.53	3.83	194.24	52.57	0.89	189.33
F8		3.6	83.8	78.87	2.97	199.14	42.97	0.92	204.97
F10		3.92	85.9	74.65	3.98	202.09	54.78	0.99	217.34
F13		4.13	83.37	80.33	2.99	214.84	35.79	1.03	225.27
F15		4.47	88.94	82.76	3.03	217.78	43.66	1.13	252.95
F0	80 °C	2.78	57.6	44.09	5.14	-	-	0.56	100.20
F1		2.9	59.37	48.39	4.36	-	-	0.64	122.06
F3		2.91	59.72	45.78	4.1	-	-	0.75	168.63
F6		3.25	59.71	44.61	4.7	-	-	0.90	217.05
F7		3.19	60.27	45.33	3.91	-	-	0.99	267.88
F8		3.36	60.68	48.15	4.57	-	-	1.04	281.75
F10		3.43	59.12	43.81	4.57	-	-	1.10	307.78
F13		3.73	59.79	53.23	3	-	-	1.12	295.89
F15		3.98	59.18	45.02	8.04	-	-	1.26	348.15

4.2.4 Fractography

4.2.4.1 Tensile Samples

The topography of the fracture surfaces of the epoxy-based nanocomposites is of particular interest. Figure 4.23 demonstrates the fractographs from tensile tests at room temperature. The fracture surface can be roughly divided into two distinct regions: the crack initiation zone (indicated by I) and the crack propagation zone (indicated by P). The former looks dark grey in SEM images and is distinguished by a relatively smooth area together with several river markings indicative of cracks propagation on slightly different planes. Surrounding the crack initiation zone is the crack propagation zone, which is characterized by very rough surface having hackles or ribbons emanating radially from the initiation site with numerous fracture steps in between. The smooth region usually corresponds to the zone of sub-critical crack

growth or the zone over which the crack is accelerating, while the rough region relates to the fast fracture zone, formed due to the considerable branching of the primary crack [135]. It can be seen from Figure 4.23 that at room temperature the smooth region of the unfilled epoxy material is the roughly same size as that of the filled materials. However, the appearance of the rough regions of filled and unfilled materials is quite disparate. This can be clearly detected in higher-magnified SEM images, as shown in Figure 4.24. It is clearly observed that numerous dimples are present in the fracture surface of the filled epoxy resin, and the dimple density increases with particle content. In contrast, there are only ribbons and river lines in the unfilled resin. The formation of the dimples is accompanied by the creation of new fracture surfaces, and thus much fracture energy is expected.

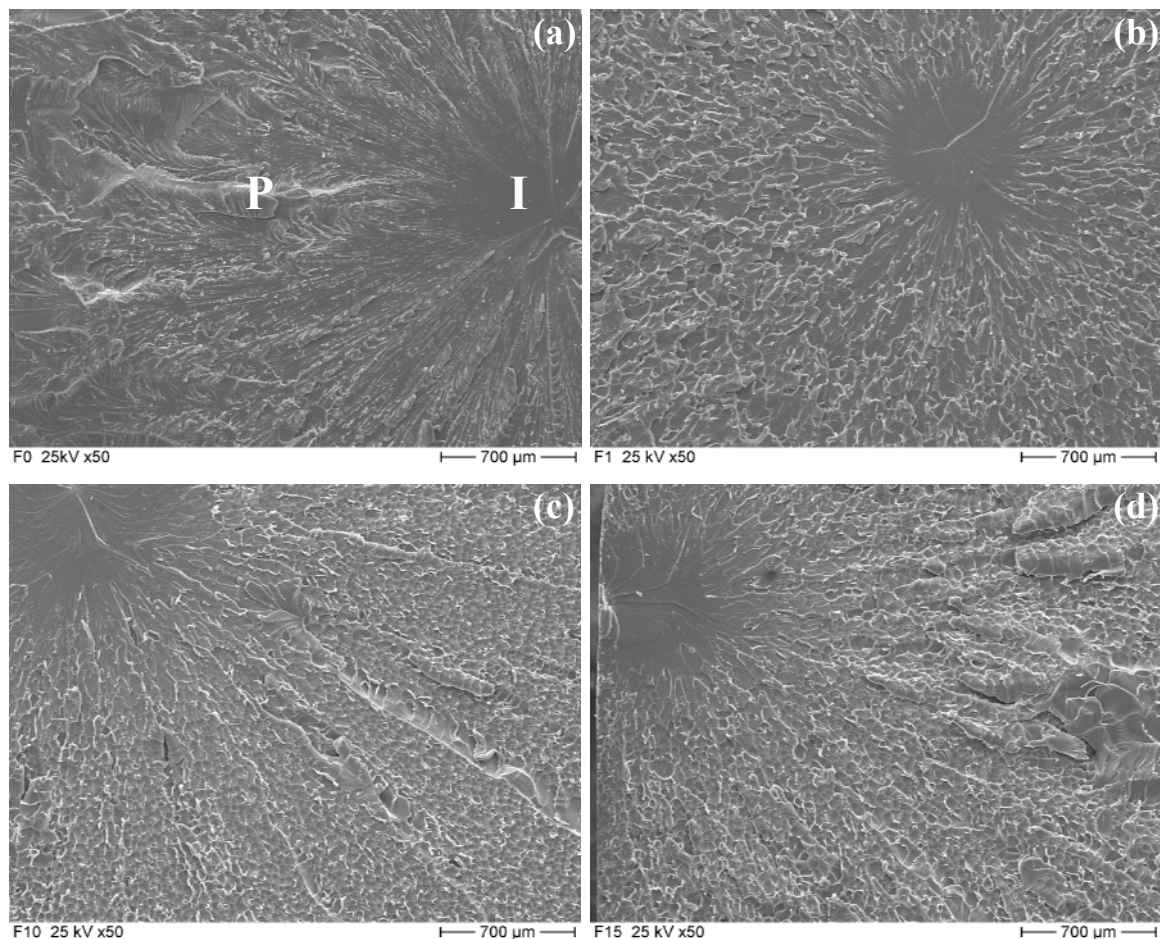


Figure 4.23: Lower-magnification SEM fractographs of bisphenol-F epoxy nanocomposites taken from tensile tests at room temperature: (a) neat matrix, (b) 1 vol.% nanosilica, (c) 10 vol.% nanosilica and (d) 15 vol.% nanosilica.

Occasionally, holes can be found in the middle of the dimples, as shown in Figure 4.25. The diameter of the dimple is much larger than that of a single particle, implying good particle-matrix interfacial adhesion. It is also seen that the basic longitudinal texture (BLT, the finest texture formed on the fracture surface, including low ridges and shallow grooves [136]) emanates radially from the hole of the dimple. Since the BLT is parallel to the direction of local crack propagation [111], this morphology suggests that the direction of local cracks is not always the same as that of macroscopic crack propagation.

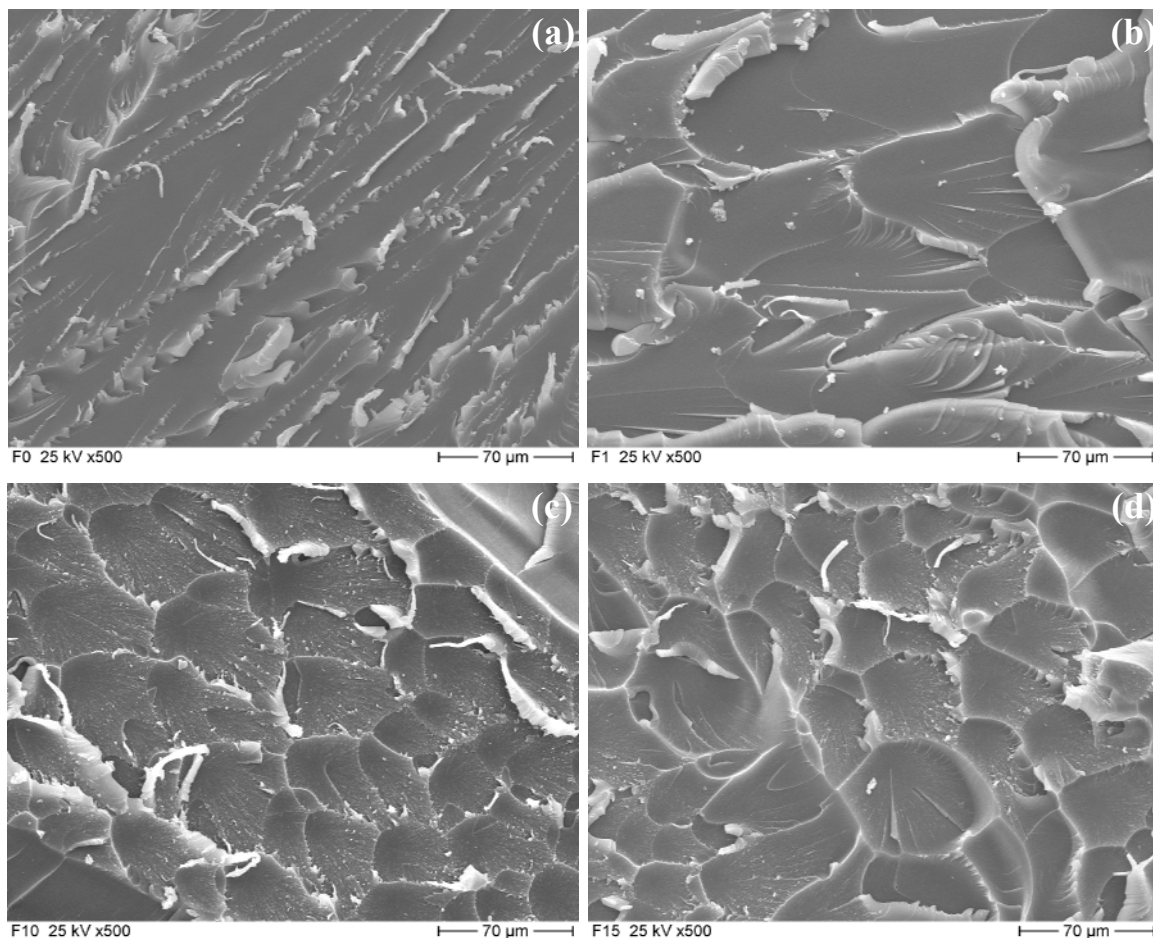


Figure 4.24: Higher-magnification SEM fractographs of bisphenol-F epoxy nanocomposites taken from tensile tests at room temperature: (a) neat matrix, (b) 1 vol.% nanosilica, (c) 10 vol.% nanosilica and (d) 15 vol.% nanosilica.

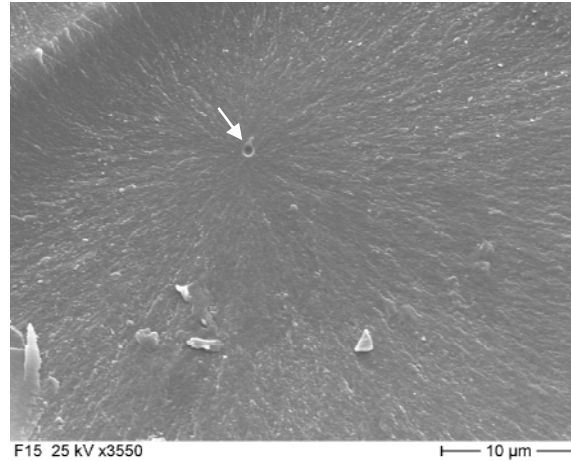


Figure 4.25: A close-up of a dimple. The arrow indicates the particle debonding from matrix. The silica loading is 15 vol.%.

When the testing temperature is increased to 80 °C the fractographs changed markedly, as shown in Figure 4.26. The most striking feature is that the smooth zone is significantly larger than that at 23 °C. More interestingly, the size of the smooth region is associated with nanoparticle content. As seen in Figure 4.26 c,d, with higher particle content, the smooth region covers nearly the entire fracture surface, and a few parabolic steps remain on the edge of the fracture surface. As stated above, the smooth region probably represents the zone of slower fracture. Hence, it is reasonable to expect that the nanoparticles in higher concentration can hinder fast crack growth and therefore prevent earlier catastrophic fracture.

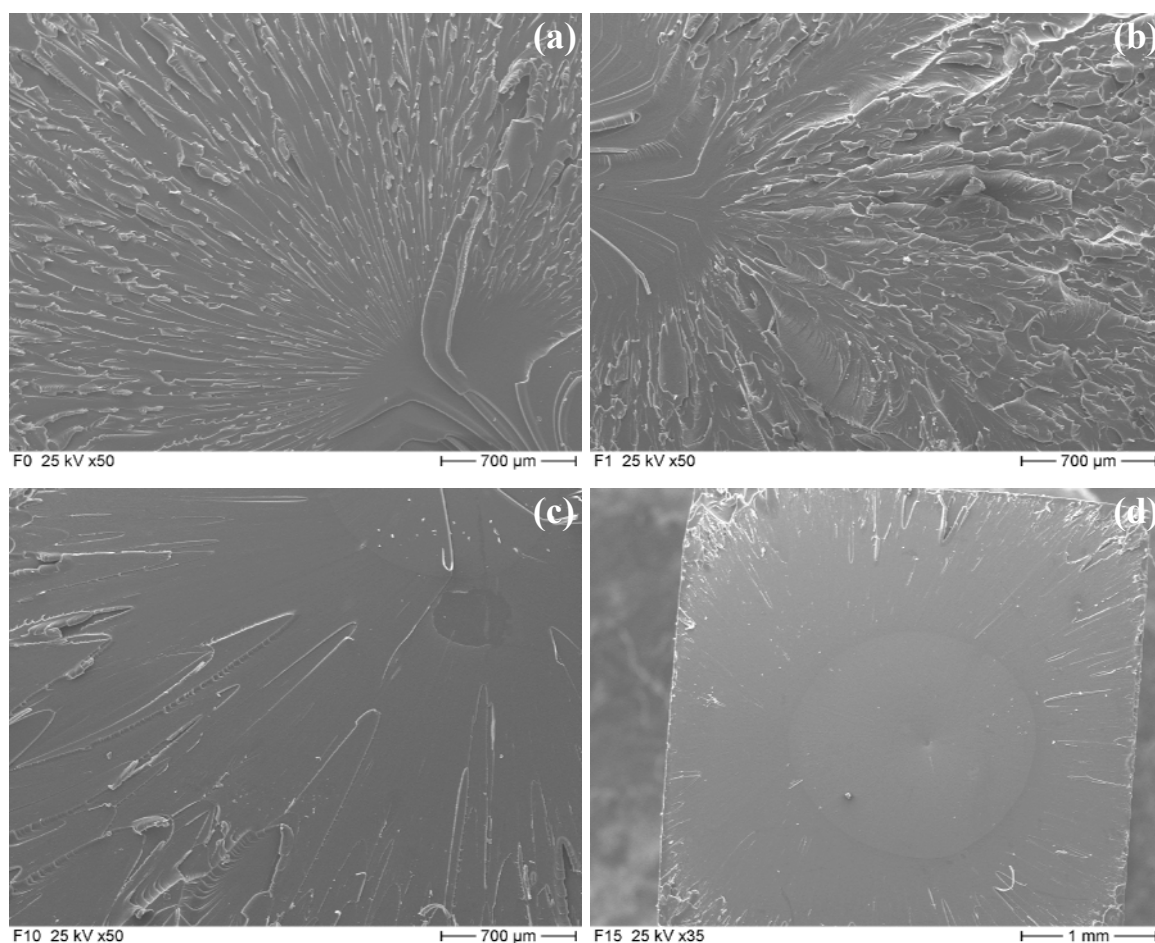


Figure 4.26: Lower-magnification SEM fractographs of bisphenol-F epoxy nanocomposites taken from tensile tests at 80 °C: (a) neat matrix, (b) 1 vol.% nanosilica, (c) 10 vol.% nanosilica and (d) 15 vol.% nanosilica.

4.2.4.2 CT Samples

Figure 4.27 presents an overview of the CT fractographs of the neat epoxy resin and the nanocomposites. The figure is a collage of 8 optical micrographs from the CT fracture surface. Obvious differences between them can be identified. Firstly, the fracture surface of the nanocomposites is much rougher than that of the neat matrix. There are only a few straight river lines through the majority of the fracture surface of the neat matrix; however, they are considerably deflected and discontinuous in the nanocomposites. Secondly, the arrest line that forms due to stick-slip growth is clearly visible on the fracture surface. The slightly curved arrest lines, as indicated by arrows, are roughly perpendicular to the crack propagation direction. An obvious feature is that the amount of arrest lines is greater for the nanocomposites than for the neat matrix.

This is also accord with the experimental observation. As stick-slip behaviour reflects crack tip blunting, it can be inferred from Figure 4.27 that addition of the nanoparticles can effectively promote crack tip blunting, the mechanism of which is likely due to nanoparticle-induced plastic shear deformation around the crack tip.

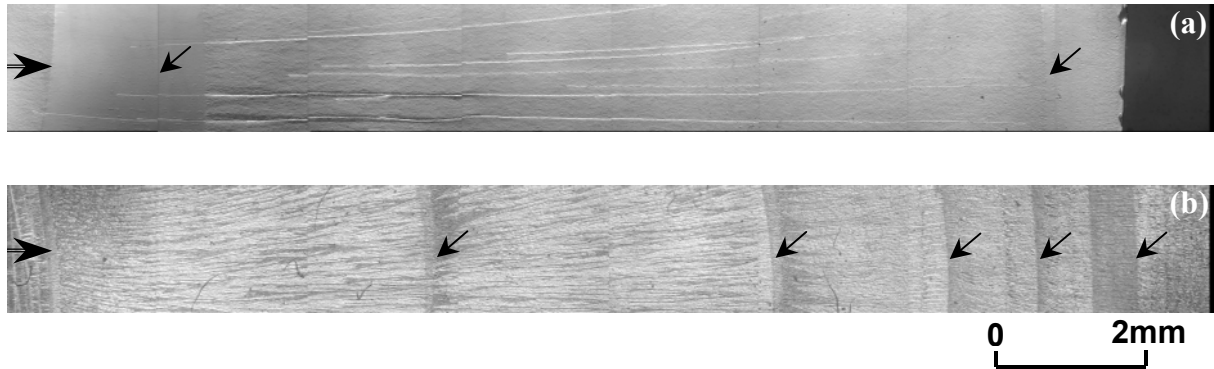


Figure 4.27: Overview of CT fracture surfaces tested at room temperature: (a) neat matrix, (b) 15 vol.% nanosilica. The arrows indicate the crack propagation direction and arrest lines, respectively.

SEM micrographs can further supply useful information on the fracture behaviour of unfilled and filled epoxy resins. Figure 4.28 shows the SEM fractographs taken near the crack tip of CT specimens tested at room temperature. For the neat epoxy resin, the fracture surface is mirror-smooth and featureless (Figure 4.28 a). Few river lines can be found at higher magnification (Figure 4.28 b). For the nanocomposites with 8 vol.% filler content, the density of the river lines is much higher. This feature is consistent with observations in cycloaliphatic type nanocomposites. The high-density river lines in the nanocomposites are formed due to particle-matrix interactions and improve the fracture resistance of the epoxy resin. The possible toughening mechanisms consist of crack deflection, crack pinning and bowing as well as crack tip blunting, which are discussed in depth in the next section.

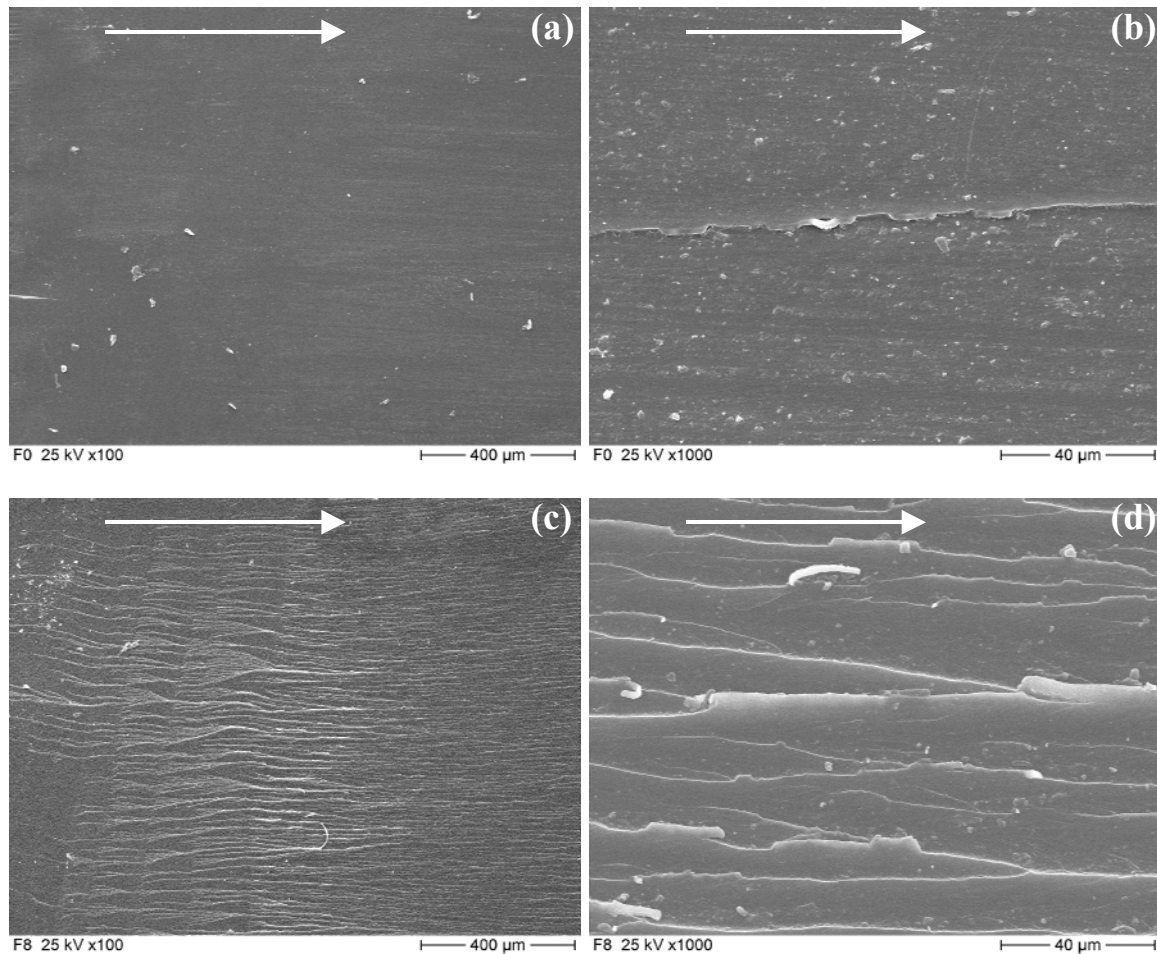


Figure 4.28: SEM fractographs of bisphenol-F epoxy nanocomposites taken from CT tests measured at 23 °C. The arrows represent the crack propagation direction: (a) crack initiation region for neat matrix, (b) crack propagation region for neat matrix, (c) crack initiation region for nanocomposite with 8 vol.% nanosilica particles and (d) crack propagation region for nanocomposite with 8 vol.% nanosilica particles.

As shown in Figure 4.21, a higher testing temperature (80 °C) led to an increase of K_{IC} and G_{IC} of the nanocomposites with relatively higher filler content (≥ 3 vol.%). This increase is also reflected in the CT fractographs, as shown in Figure 4.29 a. (The fracture surface of the neat matrix at 80 °C is very similar to that at 23 °C, and therefore is not shown here.) Be careful comparison of the CT fractographs of the nanocomposites at 23 and 80 °C (Figure 4.28 c vs. Figure 4.29 a) one can still detect some different points, i.e., the river lines at 80 °C appear to become more tortuous. This can be attributed to the relatively larger plastic deformation of the matrix at higher temperature. In other words, increased plastic deformation is responsible for the

improvement in fracture toughness. In addition, Figure 4.29 b supplies some evidence for the crack tip blunting mechanism, which results in stick-slip crack growth. As is evident, high-density river lines near an arrest line as well as some fibrils (indicated by black arrows) can be clearly recognized. This finding suggests that the crack tip blunting probably results from localized plastic deformation around the crack tip.

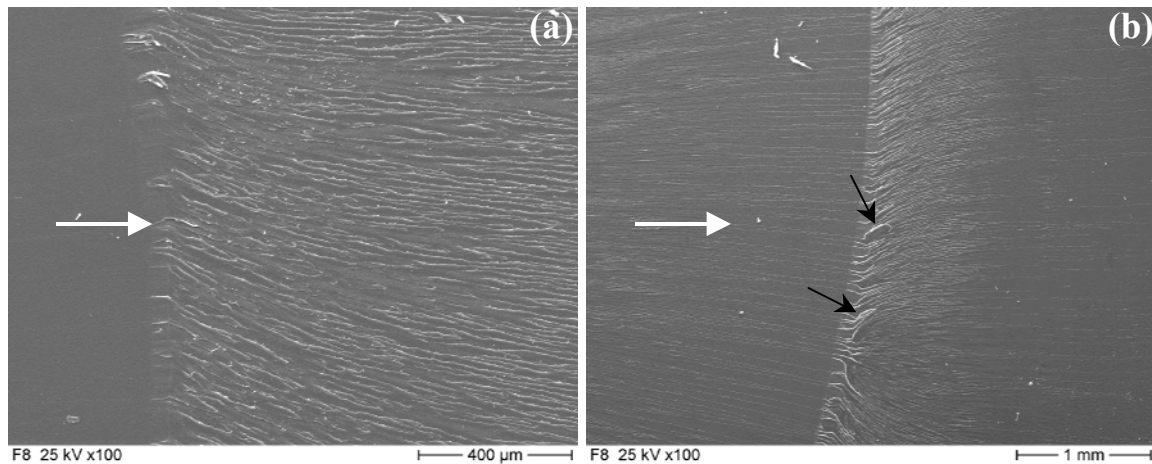


Figure 4.29: SEM fractographs of epoxy nanocomposites (8 vol.% silica) taken from CT samples tested at 80 °C. The white arrows indicate crack propagation direction: (a) crack initiation region, (b) around an arrest line. The black arrows indicate some slight fibrils near the arrest line.

To make a quantitative characterization of the CT fracture surfaces, laserprofilometry was used in the present study. Typical topographs of the CT samples tested at room temperature are shown in Figure 4.30. It is considered that the array of parallel ridges in this figure may represent the river markings shown in SEM micrographs. Similarly, the river lines tend to be deflected at higher filler content and finally yield a very rough surface. The surface roughness of the CT fractographs was determined in terms of the arithmetic average surface roughness, R_a , and the square root average surface roughness, R_q . To achieve better accuracy, at least five scans at different positions were taken of each specimen. The effect of nanoparticle content on surface roughness is shown in Figure 4.31. The testing temperature appears to have little effect on the surface roughness. Despite some scatter of the experimental data, the general effect of filler content on surface roughness can be still observed. Surface roughness is dramatically increased at lower filler content, and then reaches a plateau at higher

filler content. Further increase in filler content seems to cause a slight decrease in surface roughness at 23 °C. On the basis of the morphologies of the CT specimens, it is considered that the crack deflection effect, crack bowing effect and plastic deformation of the matrix are the major toughening mechanisms in our epoxy-based nanocomposites.

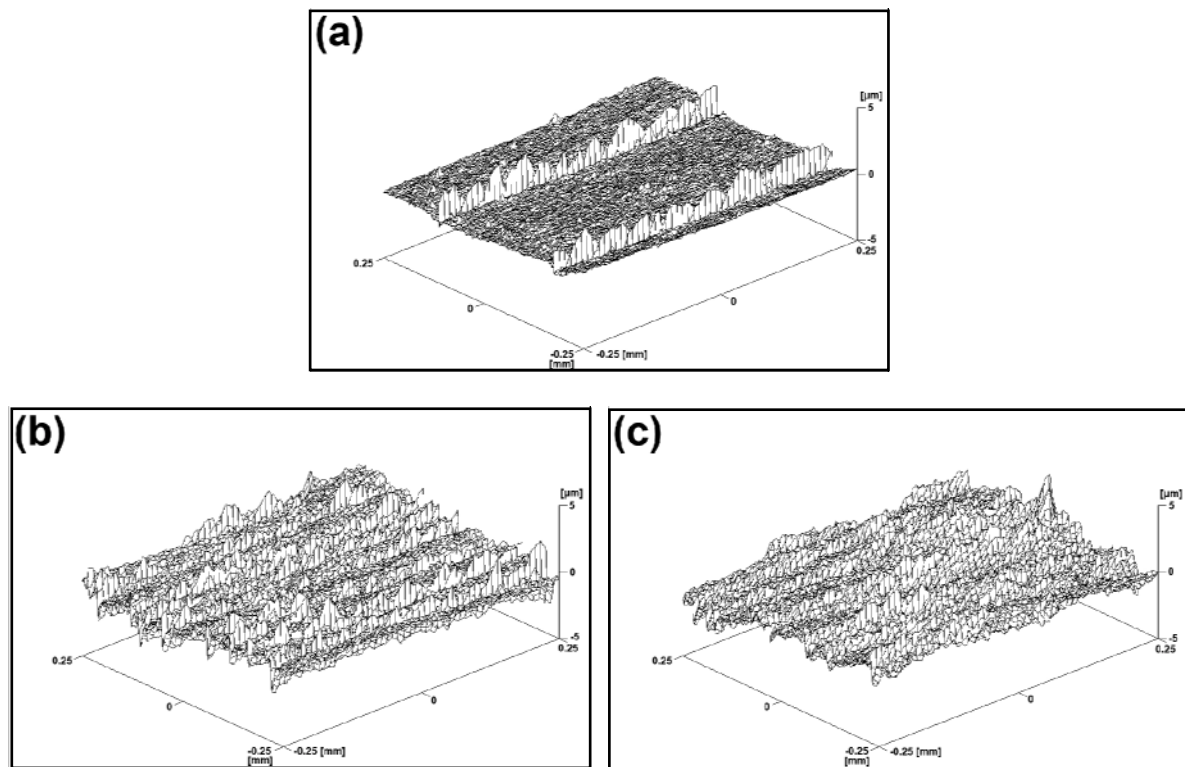


Figure 4.30: Typical topography of the bisphenol-F epoxy nanocomposites taken from CT samples tested at 23 °C: (a) neat matrix, (b) 10 vol.% nanosilica and (c) 15 vol.% nanosilica.

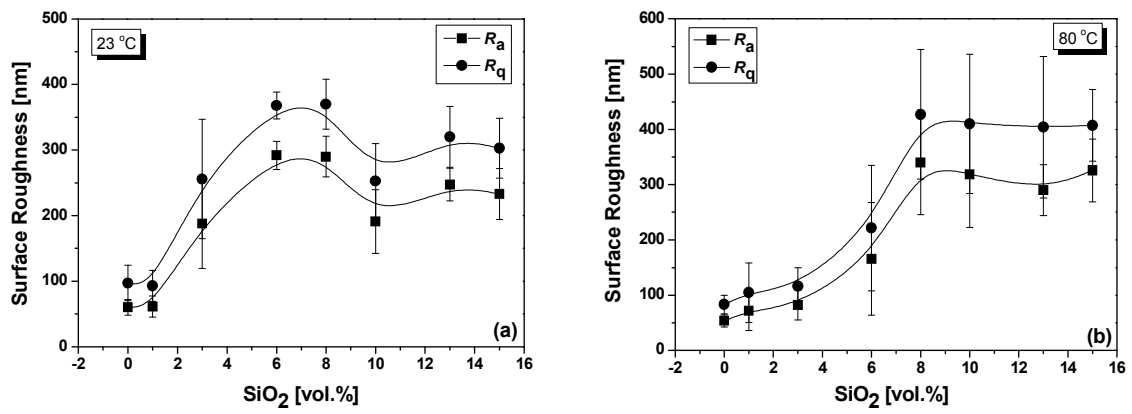


Figure 4.31: Surface roughness of CT samples as a function of nanosilica volume content: (a) 23 °C and (b) 80 °C.

5 Thermoplastic Nanocomposites

Polyamide 66 (PA66) and isotactic Polypropylene (PP) are semicrystalline thermoplastic polymers. They are used widely for numerous engineering applications due to the combination of relatively high thermal and mechanical properties together with easy processing and relatively low expense. However, their one distinct deficiency is low crack resistance. They tend to break in a brittle manner in the presence of sharp notch or impact load. This factor has somewhat limited their broad utility [137]. Some practical applications require components made of PA66 or PP-based composites to be used at higher temperatures [138], e.g. piping systems for hot water supply, panels for automobiles, bearings, rollers, and containers for food industries. Therefore, characterization of the mechanical performance and fracture behaviours of PA66 or PP at higher temperatures would be interesting both academically and practically.

During failure PA66 and PP samples can develop a geometry-dependent plastic deformation zone around the crack tip, the size of which is comparable to the crack length. This kind of fracture process cannot be characterized by linear elastic fracture mechanics (LEFM) which is valid for brittle fracture, i.e. where little plastic deformation occurs before fracture. Both K_{IC} and G_{IC} are meaningless to describe the fracture process. To overcome this problem, the EWF method was used to evaluate the fracture toughness of neat PA66 (PP) and its nanoparticle-filled composites tested at different temperatures. The EWF technique was described in detail in section 3.2.2. For PA-based composites, the temperature dependent fracture parameters were obtained in experiments and also estimated via a crack opening displacement (COD) method. The fracture surfaces were observed by SEM. In light of the experimental results and the COD method the related fracture mechanisms are further discussed. The EWF technique is not a universally applicable method for characterization of material toughness. As shown in section 5.2, it fails to describe the fracture behaviours of PP-based composites. The possible reasons are discussed in the corresponding paragraphs.

5.1 Polyamide 66 Filled with Various Nanoparticles

5.1.1 Microstructure

Two typical SEM fracture surfaces are selected to show the dispersion effect of nanoparticles in the PA66 matrix, as shown in Figure 5.1. The designation of samples is given in Table 3.4. For 1T805PA (the surface-modified nano-TiO₂ particle filled PA66 sample), nearly homogeneous distribution of nanoparticles is achieved, although some aggregates are present. However, in the case of 1R7200PA (nano-SiO₂ filled PA66 sample), some larger aggregates of micron-size can be found. Clearly, it is not easy to break up all the nanoparticle aggregates by using only twin-screw extrusion. It is speculated that the relatively good dispersion in 1T805PA is attributable to the appropriate surface modification and the lower specific surface area value (cf. Table 3.3).

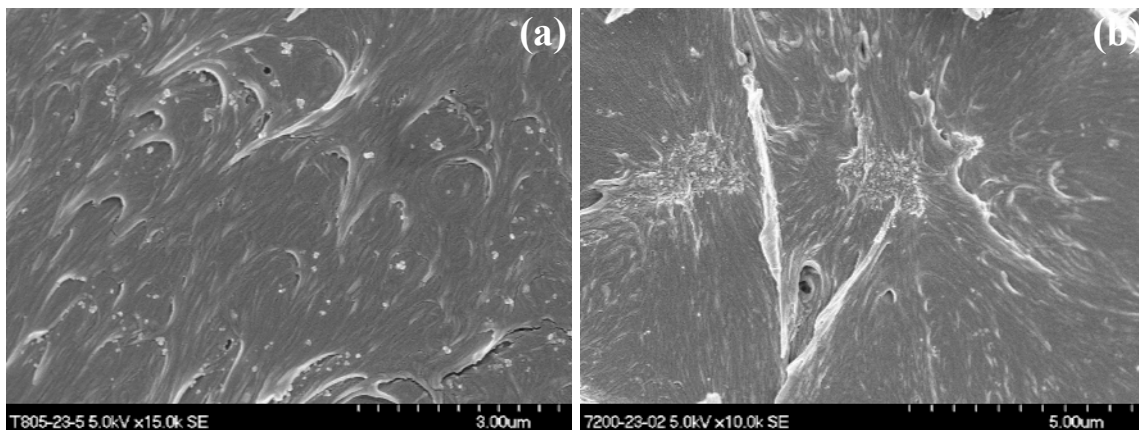


Figure 5.1: Typical SEM morphology of PA-based nanocomposites: (a) 1T805PA and (b) 1R7200PA.

5.1.2 Thermal Properties

DSC results are summarised in Table 5.1. It can be seen that a small volume fraction of nanoparticles does not affect the degree of crystallinity (X_c), the melting point (T_m) or the crystallization temperature (T_c) of the host matrix. Therefore, the influence of crystallinity on the matrix toughness after introduction of the nanoparticles seems negligible.

Table 5.1: DSC and DMTA results of PA-based nanocomposites

Sample code	DSC			DMTA	
	X_c [%]	T_m [°C]	T_c [°C]	T_g [°C]	$\tan \bar{\delta}_{max}$
Neat PA	38.67	266.34	232.31	59.7	0.123
1TPA	34.53	266.45	232.70	71.6	0.133
1T805PA	38.56	266.26	232.51	67.5	0.127
1R7200PA	37.94	266.60	233.84	69.8	0.127
1APA	35.68	265.35	233.53	69.8	0.141

Figure 5.2 presents the DMTA results. The glass transition temperature (T_g) and the peak value of loss factor ($\tan \bar{\delta}_{max}$) listed in Table 5.1 are the average values calculated from two measurements of each sample. It is observed that, by introducing only 1 vol.% nanoparticles, T_g is shifted to higher temperature by about 10 °C, while the $\tan \bar{\delta}_{max}$ is changed slightly with respect to neat PA66. The results confirm that small amount of nanoparticles can effectively restrain the movements of polymeric segments, which in turn affect matrix toughness, especially in regions near the glass transition temperature. This is discussed further in the following sections.

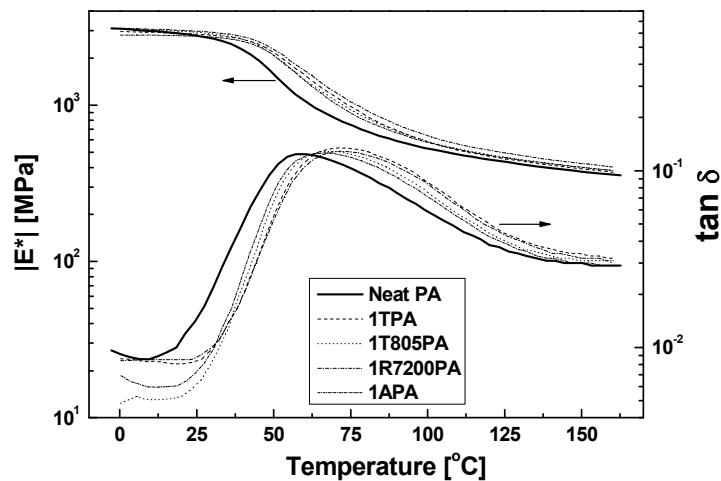


Figure 5.2: DMTA curves of loss factor and dynamic complex modulus of PA-based nanocomposites.

5.1.3 Essential Work of Fracture

Load-displacement (F - δ) curves of DDENT specimens were obtained at various testing temperatures. Most specimens exhibited full ductile fracture over the whole temperature range. A large plastic deformation zone surrounding the crack tip and evident necking after yielding were clearly observed when the specimens were loaded. Typical F - δ curves are shown in Figure 5.3 a for PA66 with 1 vol.% TiO₂ (1T805PA) measured at room temperature. These F - δ curves have geometrical similarity, indicating that the fracture mechanism is probably independent of the ligament length. In fact, the self-similarity of the F - δ curves is a basic precondition of the EWF methodology to be applied. Figure 5.3 b illustrates the typical F - δ curves at various temperatures of 1T805PA at a constant ligament length (≈ 10 mm). It can be seen that for a given ligament length, with increasing temperature, the maximum load decreases, but the displacement at break extends.

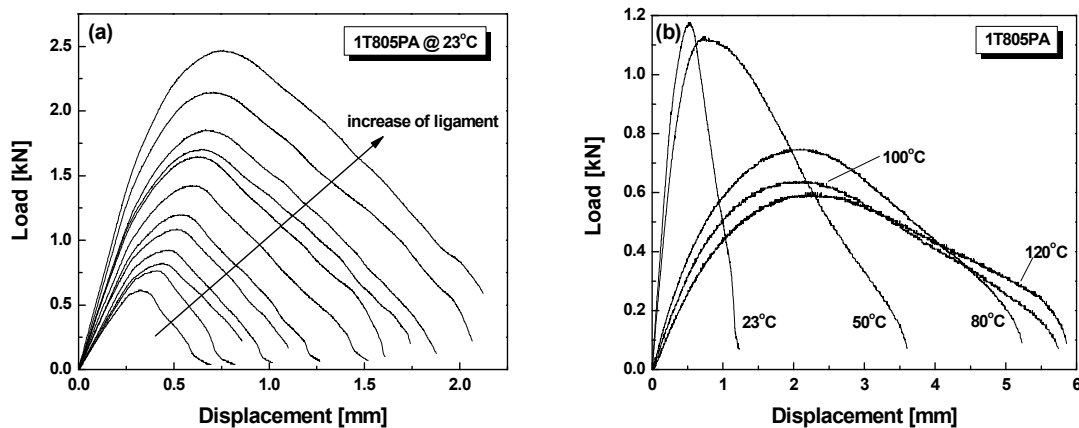
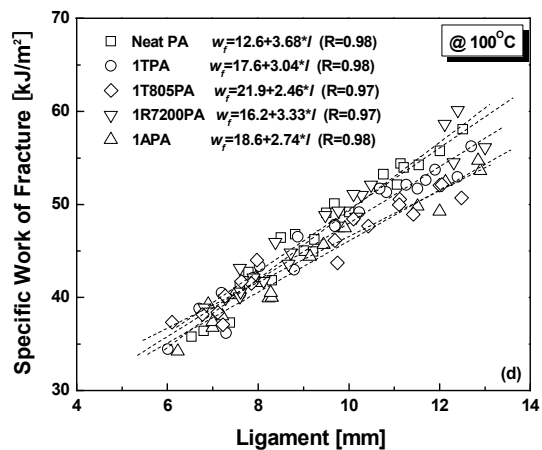
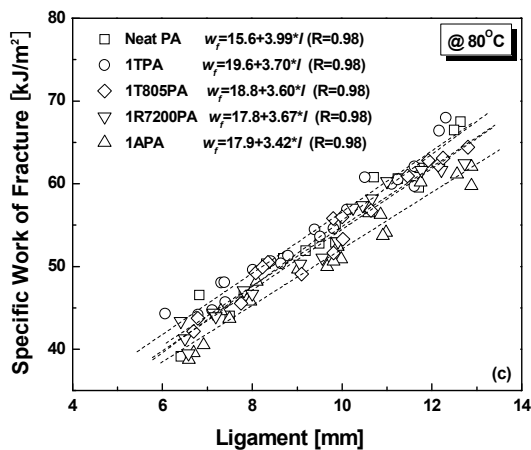
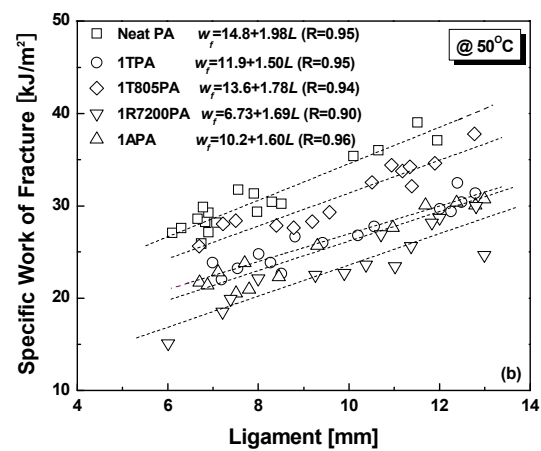
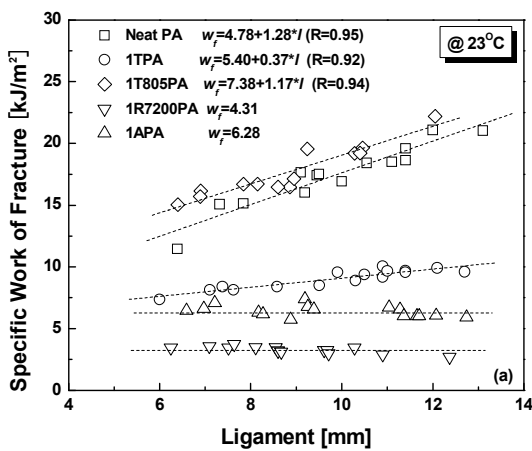


Figure 5.3: Typical load-displacement curves of the nanocomposites studied: (a) 1T805PA at 23 °C with different ligament lengths and (b) 1T805PA at various temperatures with a constant ligament length ≈ 10 mm.

Figure 5.4 presents the w_{ini} vs. l curves for all samples measured at various temperatures. It is seen that for the great majority of samples, positive slopes and good linear correlation coefficients ($R > 0.9$) are obtained. The corresponding EWF parameters, i.e. $w_{e,ini}$ and $\beta_{ini} w_{p,ini}$, which represent respectively the resistance to crack initiation and the contribution of the plastic zone to crack resistance, can be

acquired from intercepts and slopes of linear regression equations. However, it is also noticed that two groups of samples (1R7200PA and 1APA) exhibit semi-ductile fracture at room temperature, i.e. unstable fracture has occurred after yielding. Further, the specific work of fracture is nearly constant to the ligament length on the w_{ini} vs. l curve (Figure 5.4 a). In other words, the specific non-essential work item for fracture initiation ($\beta_{ini}w_{p,ini}$) can be set to zero for these two samples. Hence the $w_{e,ini}$ values can be obtained straightforwardly from the intercepts of the horizontal dashed lines in Figure 5.4 a. All these results are summarized in Table 5.2.



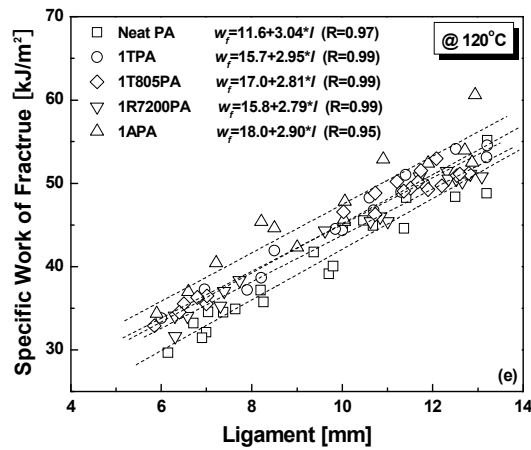


Figure 5.4: Curves of the specific work of fracture related to crack initiation against the ligament length of DDENT specimens: (a) 23 °C, (b) 50 °C, (c) 80 °C, (d) 100 °C and (e) 120 °C.

Table 5.2: EWF parameters of PA-based nanocomposites at various temperatures

Sample code	Temperature [°C]	σ_{net} [MPa]	$\delta_{0,ini}$ [mm]	$w_{e,ini}$ [kJ/m ²] (estimated)	$w_{e,ini}$ [kJ/m ²] (experimental)	$\beta_{ini}w_{p,ini}$ [MJ/m ³] (experimental)
Neat PA	23	57.6	0.18	6.95	4.78	1.28
	50	57.9	0.38	14.7	14.8	1.98
	80	36.1	0.53	12.8	15.6	3.99
	100	31.6	0.70	14.6	12.6	3.68
	120	30.2	0.72	14.4	11.6	3.04
1TPA	23	46.1	0.16	4.94	5.40	0.37
	50	56.7	0.29	11.0	11.9	1.50
	80	37.1	0.72	17.9	19.6	3.70
	100	32.5	0.95	20.7	17.6	3.04
	120	29.9	0.99	19.5	15.7	2.95
1T805PA	23	57.9	0.23	8.92	7.38	1.17
	50	58.3	0.40	15.6	13.6	1.78
	80	37.8	0.71	18.0	18.8	3.60
	100	32.6	1.03	22.5	21.9	2.46
	120	29.2	1.03	19.9	17.0	2.81
1R7200PA	23	29.8	0.19	3.80	4.31	0
	50	49.8	0.26	8.68	6.73	1.69
	80	38.5	0.79	20.4	17.8	3.67
	100	34.0	0.92	20.9	16.2	3.33
	120	31.3	0.95	19.6	15.8	2.79
1APA	23	38.5	0.24	6.19	6.28	0
	50	53.7	0.31	11.2	10.2	1.60
	80	37.4	0.62	15.5	17.9	3.42
	100	32.8	0.90	19.8	18.6	2.74
	120	30.9	1.01	20.6	18.0	2.90

5.1.4 Temperature Dependence of EWF Parameters

Temperature dependence of EWF parameters of ductile materials has been studied by many researchers. Previous work by Wu et al [94] indicated that both static and impact fracture toughness of PBT/PC/IM (impact modifier) blends had maximum values at certain temperatures. Hashemi et al [89-91] studied a series of polymer films at various temperatures and found that both $w_{e,ini}$ and $\beta_{ini}W_{p,ini}$ decreased more or less with increasing temperature. However, it should be noted that the testing temperatures used in their studies were always below the glass transition temperatures of the corresponding materials.

The temperature dependence of the EWF parameters ($w_{e,ini}$ and $\beta_{ini}W_{p,ini}$) of PA66 and its nanocomposites are given in Figure 5.5. Generally speaking, both $w_{e,ini}$ and $\beta_{ini}W_{p,ini}$ increase at elevated temperature for all materials in the present work. It is seen that $w_{e,ini}$ of the neat PA66 exhibits a peak value in the range of 50-80 °C; however, the trend is different for the nanocomposites, which show peak values at around 80-100 °C. Regarding toughening effects, the addition of nanoparticles on the one hand improves the $w_{e,ini}$ value of the host matrix at most testing temperatures. (The only exception at 50 °C was likely due to the influence of glass transition on polymer toughness, discussed in detail in the next paragraph.) On the other hand, all nanoparticles reduce the $\beta_{ini}W_{p,ini}$ value of the host matrix over the whole temperature range, indicating that the ability of the matrix to plastically deform is decreased after adding the nanoparticles. In other words, the incorporation of rigid nanoparticles improves the resistance to crack initiation at the cost of reduced resistance to crack propagation over the measured temperature range. This finding is also in agreement with a previous claim [105] that the two EWF parameters cannot be improved simultaneously.

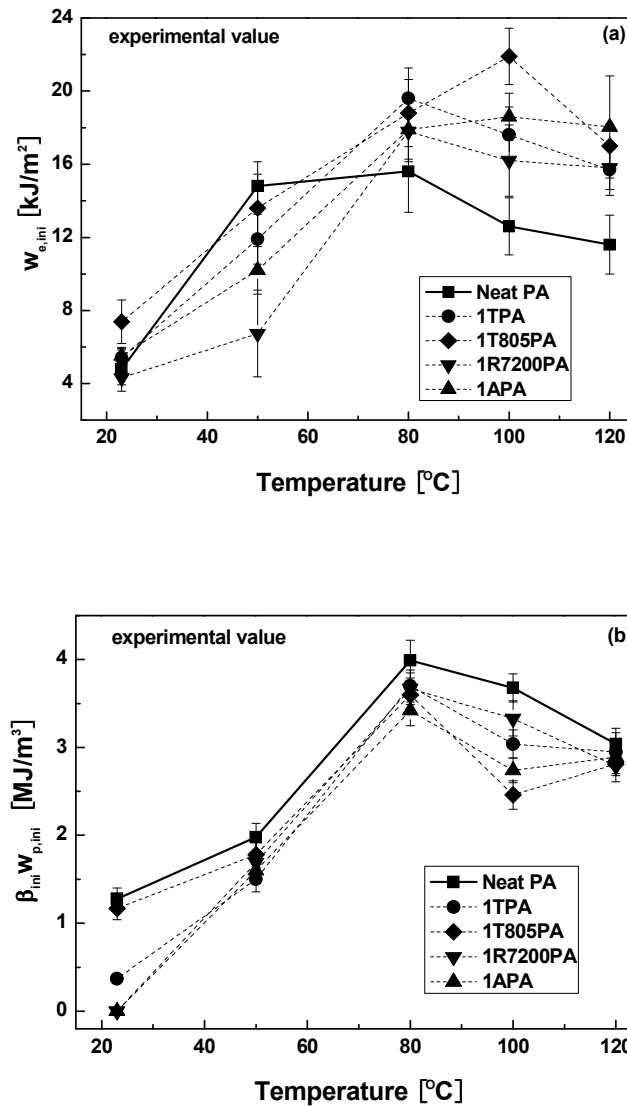


Figure 5.5: Temperature dependence of (a) $w_{e,ini}$ (specific essential work of fracture) and (b) $\beta_{ini} w_{p,ini}$ (specific non-essential work of fracture item).

As shown in Figure 5.5 a, the peak values of crack resistance exist near the glass transition temperature (T_g) of the samples studied, implying some relationship between crack initiation toughness and polymeric segment relaxation. It is known that in the vicinity of T_g , parts of polymeric segments absorb enough energy and begin to move; however, the very tight space between the macromolecules causes high internal friction, and thus additional energy is required for molecule movement [60]. That is the reason why all samples exhibit peak values of loss factor near T_g s, as

shown in Figure 5.2. Such additional energy consumption near T_g is believed also to benefit fracture toughness. Comparing the DMTA curve in Figure 5.2 with the crack initiation toughness curve in Figure 5.5 a, one can observe that the two curves display approximately similar tendencies, even though the latter is not a continuous curve. Therefore, it can be inferred from the above discussion that the shift of the peak values of $w_{e,ini}$ of the nanocomposites to higher temperatures is probably due to their increased T_g s.

5.1.5 COD Analysis

In order to understand the toughening mechanisms of the nanocomposites, the crack opening displacement (COD) approach proposed by Hashemi et al [89] was introduced. Assuming that the load-displacement curve of a DDENT specimen (Figure 3.4 a) is parabolic in shape, the following equation can be easily deduced:

$$w_{e,ini} = \frac{2}{3} \sigma_{net} \cdot \delta_{0,ini} \quad (5.1)$$

where σ_{net} ($=F_{max}/lt$) is the net section stress of a DDENT specimen; $\delta_{0,ini}$ is the COD related to crack initiation, which is the extrapolated value of $\bar{\delta}_{ini}$ at $l=0$ according to equation (5.2):

$$\bar{\delta}_{ini} = \delta_{0,ini} + \alpha_{ini} \cdot l \quad (5.2)$$

where $\bar{\delta}_{ini}$ is the displacement related to crack initiation (Figure 3.4 a), and α_{ini} is the corresponding proportional constant.

With equation (5.1), $w_{e,ini}$ can be considered as a product of two basic factors, $\bar{\delta}_{0,ini}$ and σ_{net} . Here $\bar{\delta}_{0,ini}$ represents the degree of crack tip blunting during the crack initiation process, and σ_{net} correlates with the material yielding stress (according to plasticity theory, $\sigma_{net} = 1.15\sigma_y$ for DDENT specimen under a pure plane stress condition [90]). Both $\bar{\delta}_{0,ini}$ and σ_{net} were calculated and summarized in Table 5.2. Thereafter, the $w_{e,ini}$ values were estimated by equation (5.1) and plotted in Figure 5.6. By comparing Figures 5.6 and 5.5 a, it can be recognized that the $w_{e,ini}$ values estimated by the COD method roughly correspond with the experimental results.

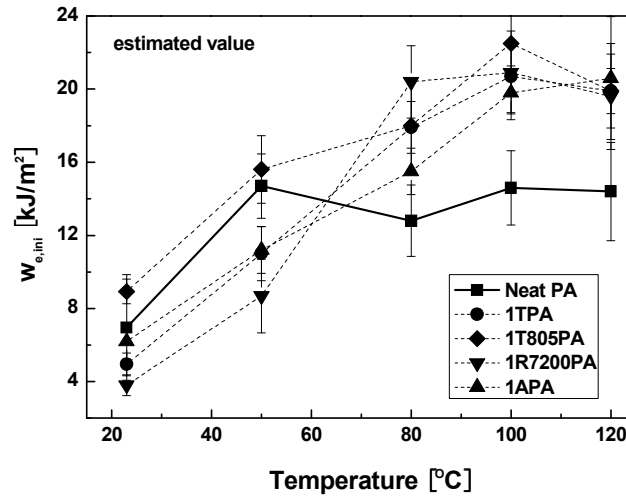


Figure 5.6: Temperature dependence of the estimated specific essential work of fracture ($w_{e,ini}$).

The temperature dependence of both $\bar{\delta}_{o,ini}$ and σ_{net} of the various nanocomposites is given in Figure 5.7. The general tendency in Figure 5.7 a shows that the addition of nanoparticles reduces σ_{net} values of the host matrix to a greater or lesser degree. The difference in σ_{net} values between the matrix and nanocomposites is much more obvious at room temperature, whereas it gradually diminishes with increasing temperature. However, the situation is different for crack tip blunting, $\bar{\delta}_{o,ini}$, as shown in Figure 5.7 b. The addition of nanoparticles increases the $\bar{\delta}_{o,ini}$ value at most test temperatures. The abnormally high $\bar{\delta}_{o,ini}$ of the neat matrix at 50 °C is again due to the influence of polymeric segment relaxation near T_g s, as discussed in an earlier section. In addition, it is easy to understand from equation (5.1) that after introduction of the nanoparticles, once the increase in $\bar{\delta}_{o,ini}$ outweighs the decrease in σ_{net} , the $w_{e,ini}$ value will increase, and vice versa. Therefore, the variation of $\bar{\delta}_{o,ini}$ and σ_{net} with temperature is important to our understanding of the toughening mechanisms of nanocomposites. It is also evident from Figure 5.7 that at room temperature both $\bar{\delta}_{o,ini}$ and σ_{net} dominate the final $w_{e,ini}$ value. However, at elevated temperatures, the influence of σ_{net} becomes much less. Thus the gradually increasing $\bar{\delta}_{o,ini}$ becomes the dominating factor affecting the $w_{e,ini}$ value.

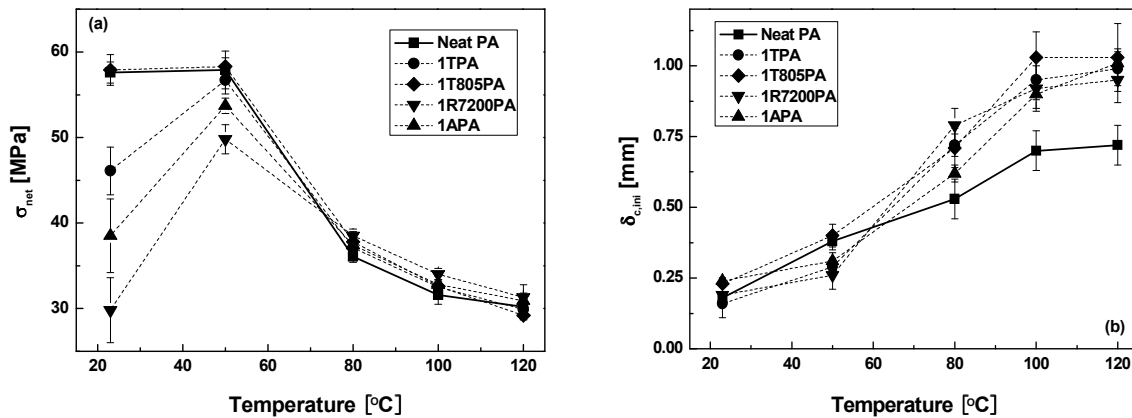


Figure 5.7: Temperature dependence of (a) σ_{net} (crack tip blunting) and (b) $\delta_{o,ini}$ (net section stress).

5.1.6 Fractography

SEM fractographs of the specimens studied offer much information as to the toughening mechanisms and may partially explain the variations of the $\delta_{o,ini}$ and σ_{net} values after the addition of nanoparticles. The fractographs of the neat PA66 and various nanocomposites measured at room temperature are illustrated in Figure 5.8. Numerous dimples can be found near crack tips for all specimens. The size of the dimples (ranging approximately from 20 to 100 μm) and their surface density are strongly dependent on the type of the nanoparticle. Our previous work [139] indicated that under load, nuclei of spherulites, matrix defects, nanoparticles and their aggregates could serve as stress concentrators in matrix, promoting formation of these dimples.

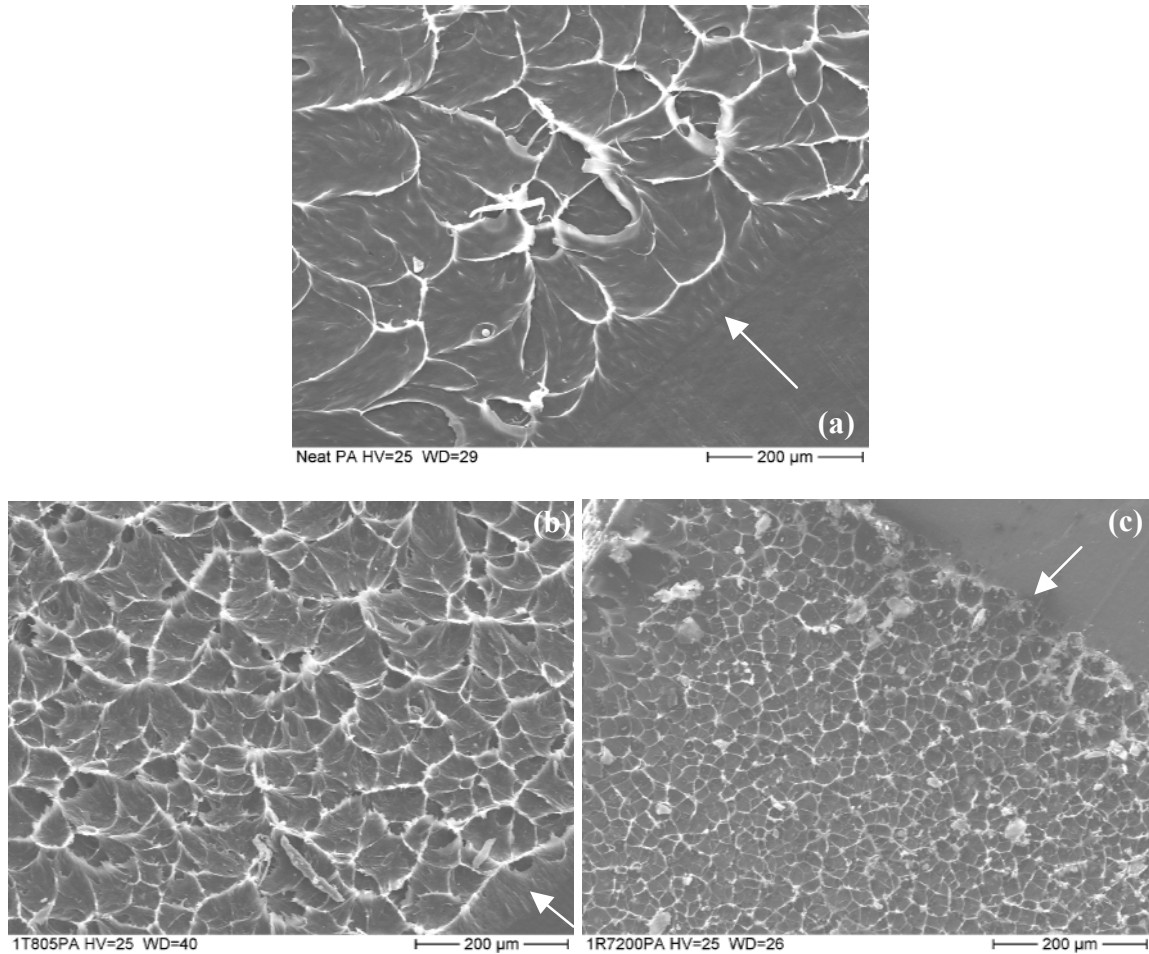


Figure 5.8: Typical SEM fractographs of DDENT samples at 23 °C: (a) neat PA, (b) 1T805PA and (c) 1R7200PA. The white arrows indicate pre-crack tips.

A higher resolution fractograph in Figure 5.9 b further shows that tiny structures of hyperbolic shape exist on the walls of these dimples of the nanocomposites (termed “sub-dimples”, indicated by black arrows). These structures are certainly correlated with stress concentrations of a single nanoparticle or smaller aggregates. In contrast, no such phenomena can be found for the neat matrix: the walls of its dimples are rather smooth, as shown in Figure 5.9 a. It is believed that formation of these dimples and sub-dimples in the nanocomposites is accompanied by a series of energy dissipative events, such as localized micro-deformation of the matrix, particle debonding, and cavitations. All these events may reduce the stress intensity or modify the stress state around the crack tip, contributing to increased blunting of the crack tip, $\delta_{o,ini}$. Therefore, a high dimple density might correspond directly to a high degree of crack tip blunting. The crack tip blunting effect of the nanocomposites is

generally higher than that of the neat matrix over most of testing temperature range (Table 5.2).

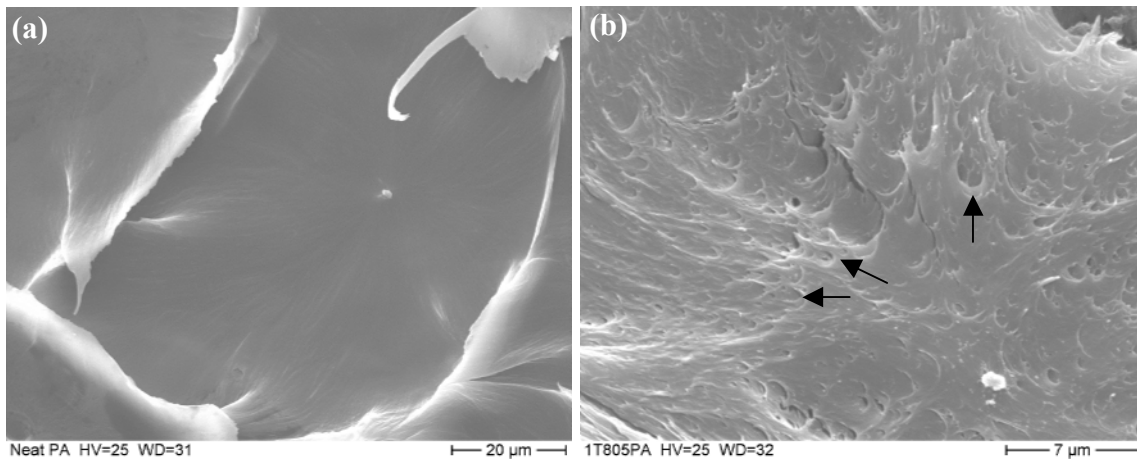
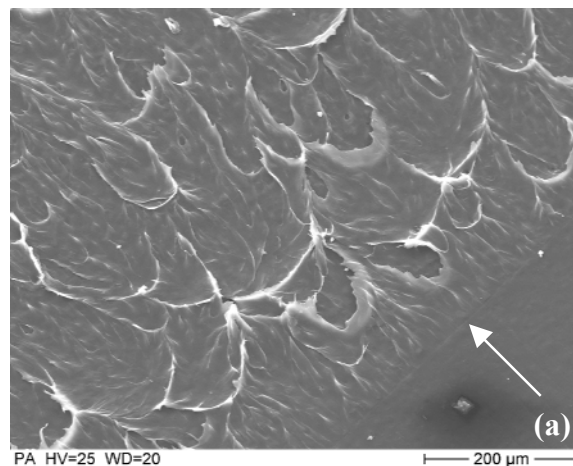


Figure 5.9: Close-up of dimples of DENT samples at 23 °C: (a) neat PA and (b) 1T805PA. The black arrows indicate some sub-dimples.

Such speculation is further proposed by the fractographs at elevated temperatures (50, 120 °C) as shown in Figures 5.10 and 5.11. Again, a high density of dimples is always accompanied by higher values of $\delta_{o,ini}$. It should be noted that at 120 °C the composites became relatively soft, thus the dimples were considerably stretched and oriented along the crack propagation direction (Figure 5.11).



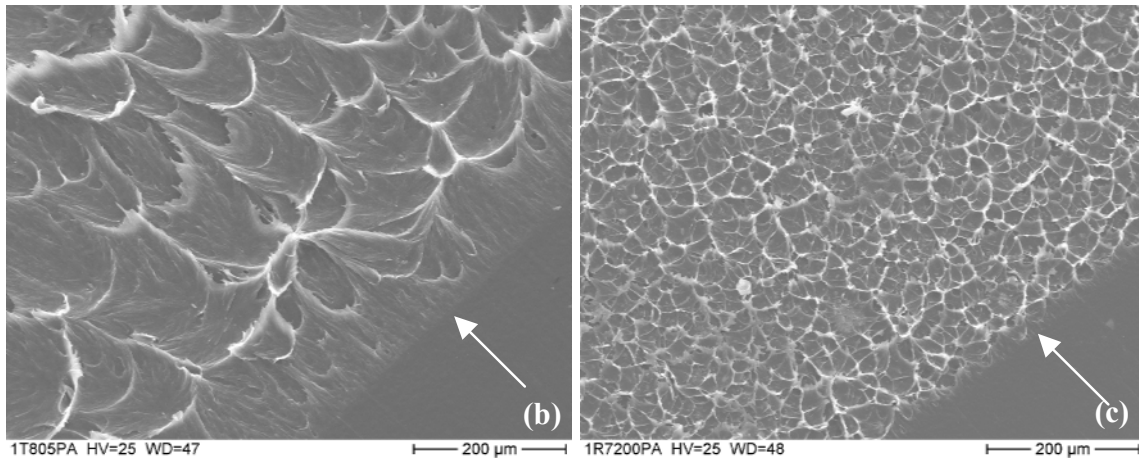


Figure 5.10: Typical SEM fractographs of DDENT samples at 50 °C: (a) neat PA, (b) 1T805PA and (c) 1R7200PA. The white arrows indicate pre-crack tips.

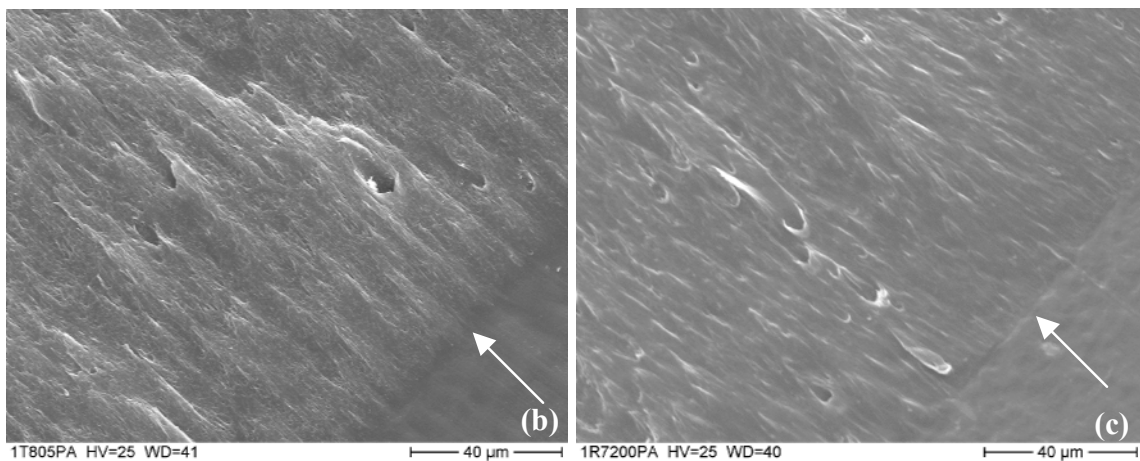
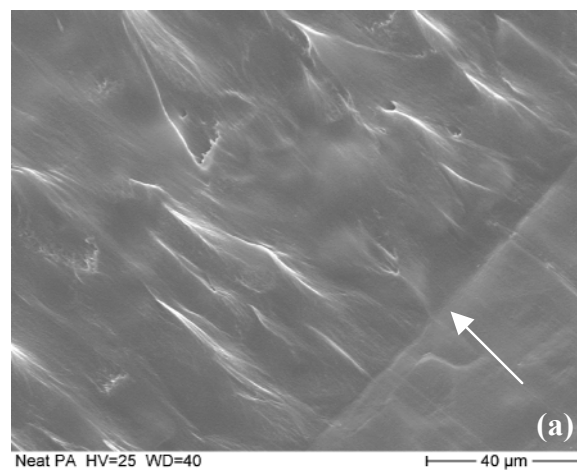


Figure 5.11: Typical SEM fractographs of DDENT samples at 120 °C: (a) neat PA, (b) 1T805PA and (c) 1R7200PA. The white arrows indicate pre-crack tips.

On the other hand, as discussed in section 5.1.5, the addition of nanoparticles can reduce the σ_{net} values, especially at room temperature. It is found that this reduction is usually associated with relatively poor dispersion of nanoparticles. For example, Figure 5.9 b shows nearly no aggregates on the fracture surface of 1T805PA. This effect is likely due to the lowest specific surface area of the nano-TiO₂ particles among all the nanoparticles, as well as the appropriate surface modifier used. Correspondingly, the σ_{net} values of 1T805PA change slightly from those of the neat matrix. In contrast, some larger aggregates can be observed on the fracture surfaces of the 1R7200PA composite, as shown in Figure 5.8 c. These larger aggregates may act as defects, triggering premature cracks, and finally decreasing the σ_{net} value. As a result, 1R7200PA presents the lowest σ_{net} at room temperature in comparison with the neat matrix. However, at elevated temperatures, the premature fracture cannot occur so easily and hence the influence of σ_{net} is minimized for all materials.

5.2 Polypropylene Filled with Nanoparticles and Nanotubes

5.2.1 Microstructure

SEM cryogenic fracture surfaces are used to examine the dispersion state of the nanoparticles and nanotubes. The representative micrographs are shown in Figure 5.12. For the 1KrPP (i.e., 300 nm TiO₂ filled PP sample), good particle dispersion is obtained. Some primary particles can be clearly observed in Figure 5.12 a. For the smaller nanoparticles (21 nm) or fibril-like nanotubes filled PP samples (including 1TPP, 1T805PP, 1MPP and 1LPP), there are still some small aggregates in the matrix, though homogeneous dispersion of the aggregates can be observed (Figure 5.12 b). High-resolution SEM images show that the size of most aggregates is in the range of 100 nm. Thus, it is thought the small aggregates cannot significantly adversely affect the mechanical properties of the resulting composites. This can be confirmed in the following paragraphs.

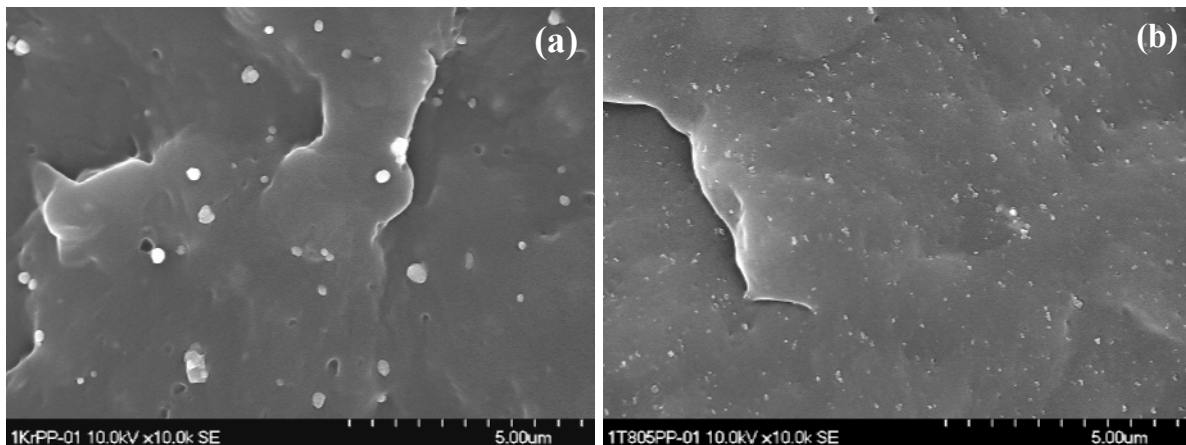


Figure 5.12: Representative SEM micrographs of PP-based nanocomposites: (a) 1KrPP and (b) 1T805PP.

5.2.2 Thermal Properties

Figure 5.13 presents DMTA curves of the PP-based nanocomposites. It can be seen that the loss factor of the PP matrix is not altered significantly after the addition of nanoparticles. T_g s of the filled PP composites are slightly decreased by c.a. 1 °C. The DSC results listed in Table 5.3 show that the small amount of nanoparticles has only

a little effect on crystallinity (X_c) and melting temperature (T_m). Such results agree with those obtained for PA66-based composites systems (cf. section 5.1.2). It is interesting to find from Table 5.3 that carbon nanotubes increase the crystallization temperature (T_c) by c.a. 13 °C, while little increase in T_c is obtained for spherical particle filled composites. Evidently, as compared to the spherical particles, nanotubes are the more effective nucleating agent, making the crystallization process easier when the melted PP cools.

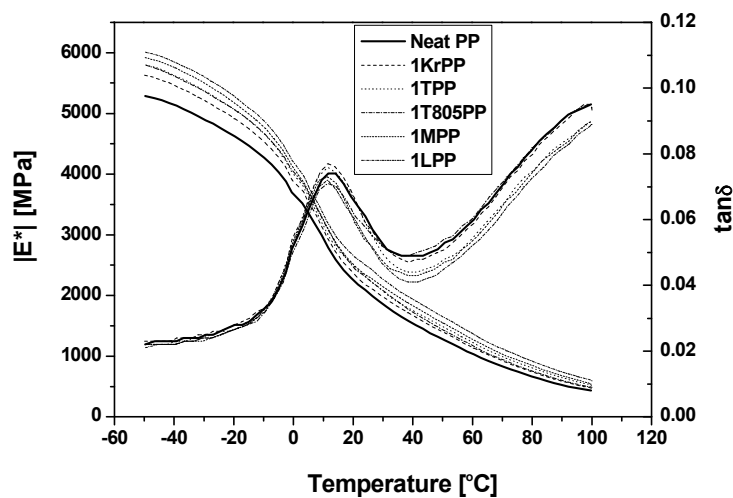


Figure 5.13: DMTA curves of PP-based nanocomposites.

Table 5.3: DSC and DMTA results of PP-based nanocomposites

Sample code	DSC			DMTA	
	X_c [%]	T_m [°C]	T_c [°C]	T_g [°C]	$\tan \delta_{max}$
Neat PP	42.1	169.01	113.17	12.85	0.074
1KrPP	41.26	169.47	113.89	11.7	0.077
1TPP	40.52	169.74	119.27	11.5	0.076
1T805PP	40.16	169.08	114.45	11.5	0.071
1MPP	45.96	169.47	126.05	11.5	0.073
1LPP	43.19	167.92	126.4	11.5	0.072

5.2.3 Tensile Properties

The static tensile properties of PP-based composites were measured at 23 and 50 °C, as shown in Figure 5.14. The addition of nanoparticles improves the Young's

modulus and tensile strength. Carbon nanotubes have the highest reinforcing efficiency at both testing temperatures, in comparison with spherical particles. This is ascribed to two reasons: on the one hand, nanotubes have much higher elastic modulus and tensile strength [26,28] than spherical particles (nano-TiO₂); on the other hand, the long aspect ratio of nanotubes promotes stress transfer from matrix to reinforcement, thus fully utilizing their high modulus and strength. It is also evident that the mechanical performance is very sensitive to the testing temperature. With a rise in temperature, the Young's modulus and tensile strength of both samples decrease considerably, a tendency of which coincides with that of the dynamic complex modulus of the PP-based composites, as shown in Figure 5.13.

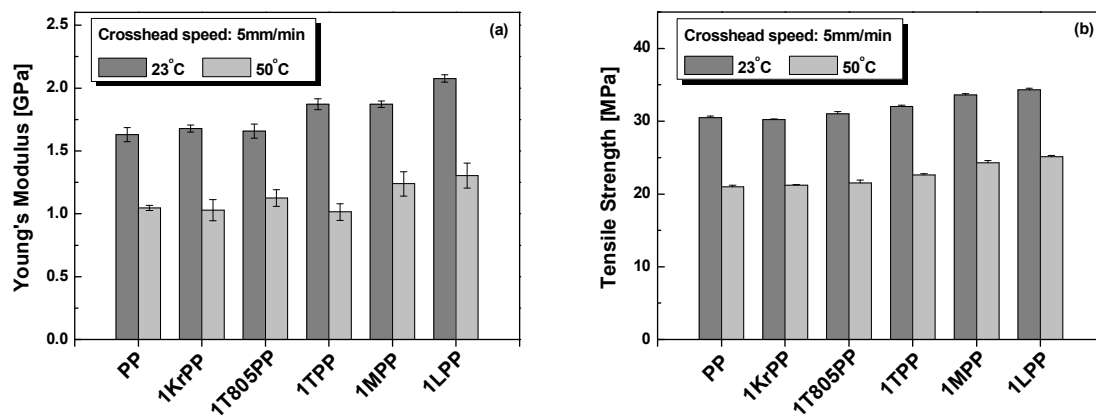


Figure 5.14: Tensile properties of PP-based nanocomposites tested at 23 and 50 °C: (a) Young's modulus and (b) tensile strength.

5.2.4 Essential Work of Fracture of Nanoparticle Filled PP Composites

5.2.4.1 Fracture Behaviours

The fracture behaviors of nanoparticle-filled PP composites were characterized by EWF approach using DDENT specimens. We do not show here the EWF results of nanotube-filled PP composites, because of the poor linear correlation coefficients and lower confidence. The EWF tests were performed at 23 °C with a strain rate of 5 mm/min. The loading direction is parallel with the mould filling direction (MFD) of the specimens.

The fracture behaviors of filled and unfilled PP samples were quite different. For the neat PP matrix, the expected fracture sequence was obtained (cf. Figure 5.15 a): at first, two plastic zones near each crack tip were formed due to the stress concentration; further, they grew and connected with each other in the vicinity of the maximum load, producing full yielding of the ligaments; thereafter the cracks started to propagate across the yielding regions until complete fracture occurred. A different process was observed for the nanoparticle-filled PP composites. Their corresponding fracture modes were: after full yielding of the ligaments, the cracks became too blunt to grow transverse to the loading direction; instead, the ligaments were stretched and torn along the loading direction up to final rupture. This process was somewhat similar to a tensile test on an unnotched specimen. All filled PP samples exhibited such fracture behaviors to a degree, most conspicuously the 1T805PP. Its $F-\delta$ curves are shown in Figure 5.15 b, and are characterised by a smooth necking plateau and high displacement at break. Clearly, due to the necking process, this kind of fracture invalidates the use of the EWF method. Moreover, it was found that increasing the strain rate reduces the displacement at break, but has little effect on the crack tip blunting of the filled PP samples. In fact, even at a strain rate of 50 mm/min, the filled PP samples also exhibit similar crack tip blunting followed by a degree of necking and final fast break (i.e., brittle break).

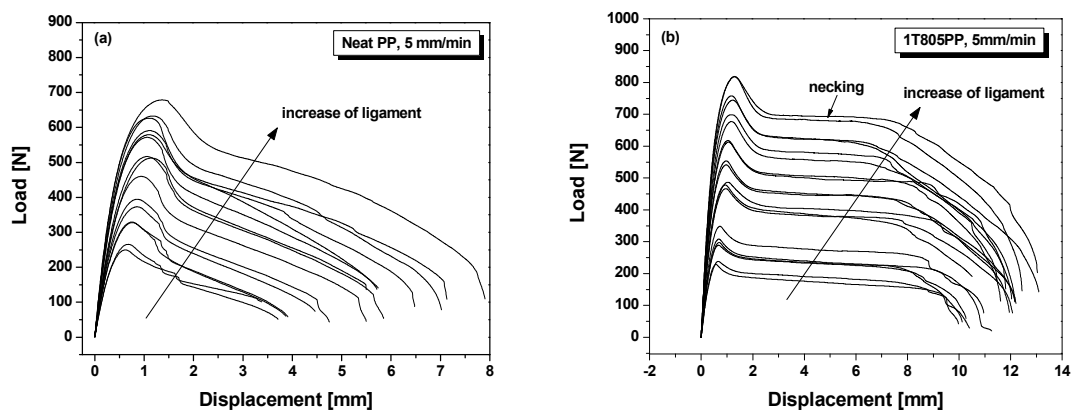


Figure 5.15: Comparison of load-displacement curves between filled and unfilled PP matrix: (a) Neat PP and (b) 1T805PP.

The difference of fracture modes between filled and unfilled PP (i.e., stable crack growth for the former vs. necking and tearing for the latter) is also apparent in Figure 5.16, the photomicrographs of broken DDENT specimens.

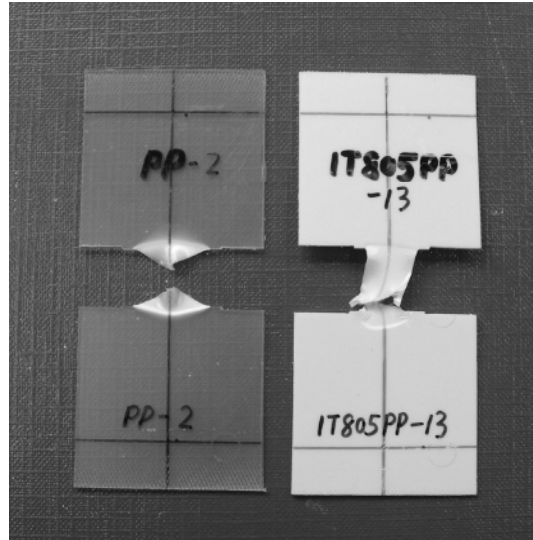


Figure 5.16: Light microscopy of fractured DDENT specimens.

Figure 5.17 shows the $w_{f,total}$ vs. l curves for particle-filled PP composites samples. Here, $w_{f,total}$ represents the specific total work of fracture. Larger scatter of data is evident for the nanocomposite samples ($R=0.76\sim 0.86$). This is because the tearing process causes random fracture in the ligaments, thus influencing the self-similarity of the $F-\delta$ curves, as shown in Figure 5.15 b. Based on the EWF concept, the specific essential and non-essential work of fracture (w_e and βw_p) were respectively derived from the intercepts and slopes of the related linear regression equations, as shown in Figure 5.17. The w_e value of neat PP is about 54 kJ/m^2 , which is higher than the values of $15\text{-}32 \text{ kJ/m}^2$ in the literature (for 1 mm PP plate). It is worth noting that DDENT specimens used in the literature were made by the compression-moulding method and hence the macromolecules were non-oriented in the specimens. However, the specimens in the present work were prepared by the injection-moulding method, and therefore a skin-core structure was formed along the thickness direction of specimens. Since the skin has higher load-carrying ability than a non-oriented structure, it should also enhance the fracture toughness of the material. From such analysis, the w_e value of 54 kJ/m^2 of neat PP seems to be normal. However, the w_e values of particle-filled PP samples seem too high (Figure

5.17), especially the value of 340 kJ/m^2 of 1T805PP. It is believed that the w_e values of the filled PP samples were greatly overestimated, which is attributed to the additional fracture energy consumed by the necking and tearing processes. The EWF parameters obtained here do not represent the intrinsic fracture parameters of the materials. Evidently, there is a limitation of the EWF method for characterizing very ductile materials.

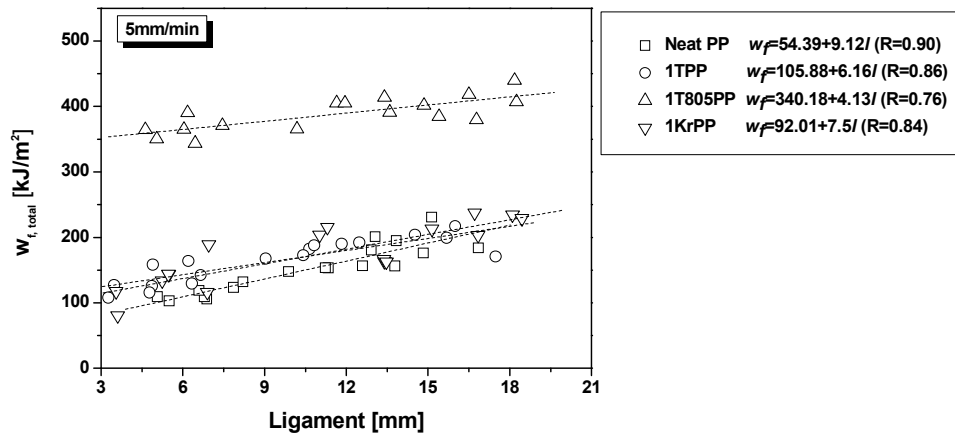


Figure 5.17: Curves of specific total work of fracture vs. ligament length of DDENT specimens for nanoparticle-filled PP composites, measured at $23 \text{ }^\circ\text{C}$ with tensile rate of 5 mm/min .

5.2.4.2 Fractography

The difference in fracture behaviors between neat PP and 1T805PP originates from their different intrinsic structures. Typical SEM fracture surfaces of DDENT specimens, as shown in Figure 5.18, allow us to better understand this point. It can be seen that all specimens have skin-core structures, generated by the injection-moulding process. However, the ratio of skin to core is higher for 1T805PP than for neat PP. The change of skin/core ratio should be related to the addition of nanoparticles (surface-modified nano- TiO_2), although the detailed mechanisms are still unclear. It is thought that the increased skin structure in the filled PP can restrain crack growth and simultaneously promote the necking process along the loading direction.

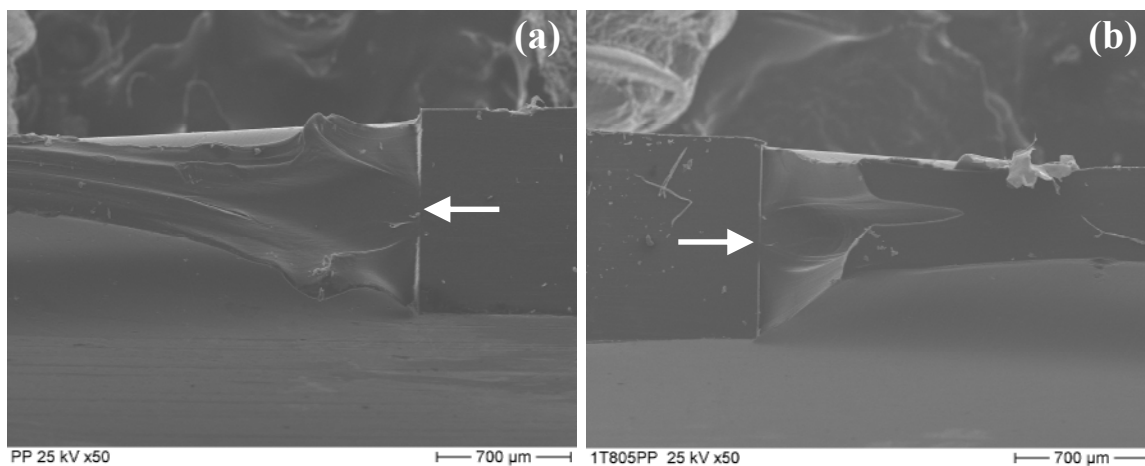


Figure 5.18: Typical SEM fractographs of DDENT samples: (a) neat PP and (b) 1T805PP. The white arrows indicate the direction of crack propagation.

5.2.5 Notched Impact Resistance of Nanotube Filled PP Composites

5.2.5.1 Temperature Dependent Impact Resistance

The fracture toughness of the carbon nanotube-filled PP composites is characterized in terms of notched Charpy impact approach in this section. The tests were carried out over a wide temperature range (-196, 23, 50 and 80 °C). It is known that impact resistance relies on specimen dimensions and is not an intrinsic material property; however, it is still significant to conduct a relative comparison of fracture toughness between filled and unfilled PP samples.

Figure 5.19 gives the impact force (and corresponding fracture energy)-test time curves for the materials studied. For clarity, only the curves of neat PP and 1LPP are plotted here. It can be seen that the impact behaviors are highly temperature dependent. At -196 and 23 °C, all materials perform in a brittle manner, which is characteristic of an abrupt breakage after reaching the peak value of impact load (Figure 5.19 a, b). Conversely, obvious crack propagation takes place at 50 and 80 °C, therefore the test time (or fracture deflection) is greatly prolonged (Figure 5.18 c, d). Actually, all specimens were incompletely broken at a temperature higher than 50 °C. Figure 5.20 shows that all materials perform brittle-to-ductile transitions (BDT) near 23 °C, which approximates to the T_g of PP (around 12 °C, measured by DMTA in Table 5.3). Obviously, when $T \geq T_g$, the increased mobility of macromolecular

segments helps to dissipate impact energy, and consequently enhances impact strength. On the other hand, carbon nanotubes provide some additional toughening effects, which also occur only when the test temperature is higher than T_g . As shown in Table 5.4, the impact strength of 1LPP is 1.04, 1.25, 2.52 and 2.67 times of that of neat PP at -196 , 23 , 50 and 80 °C, respectively. Additionally, longer nanotubes exhibit better a toughening effect than shorter ones.

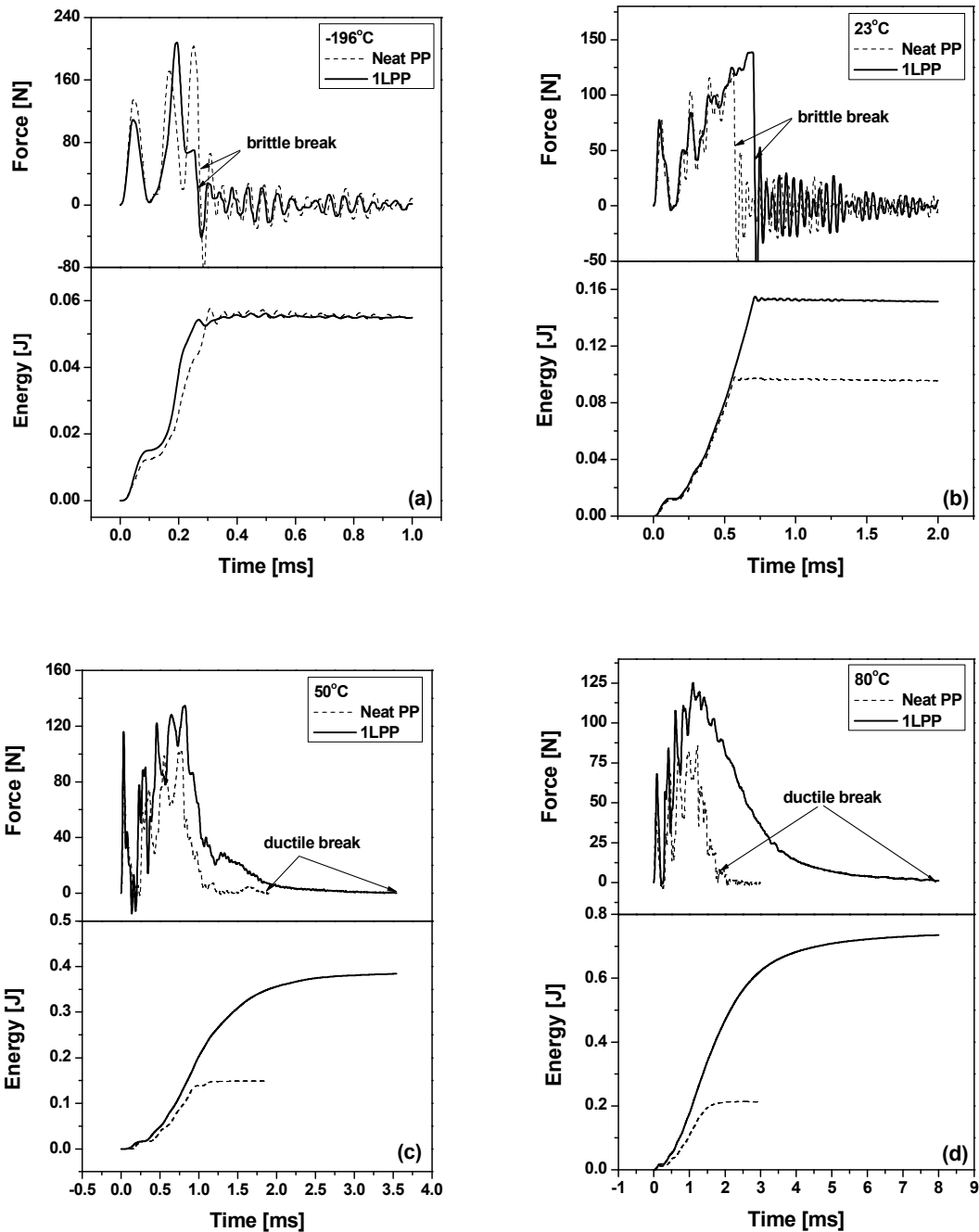


Figure 5.19: Impact force (energy)-test time curves for PP and 1LPP at various temperatures.

Table 5.4: Impact strength of multi-walled filled PP composites

Sample code	CNT volume content [%]	Test temperature [°C]	Impact strength [kJ/m ²]
Neat PP	0	-196	2.31±0.2
		23	3.57±0.08
		50	5.88±0.26
		80	9.52±0.51
1MPP	1	-196	2.47±0.12
		23	4.09±0.21
		50	11.19±0.46
		80	24.35±0.49
1LPP	1	-196	2.4±0.09
		23	4.47±0.13
		50	14.82±0.75
		80	25.41±1.73

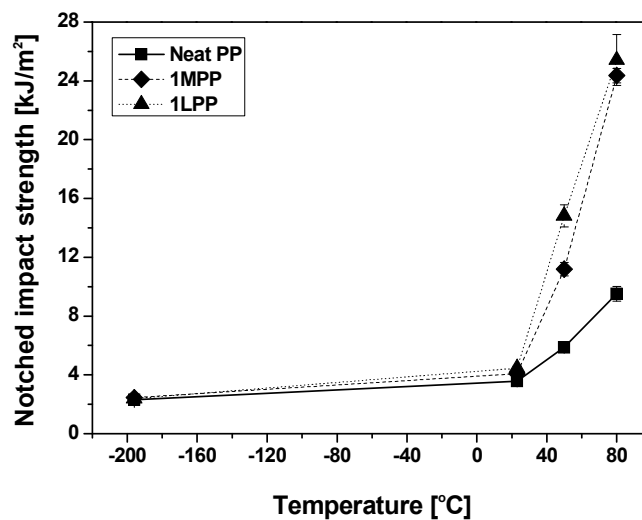


Figure 5.20: Temperature dependence of Charpy notched impact strength for PP and its composites.

Furthermore, it is obvious from Figure 5.19 that fracture energy is practically dominated by two factors, i.e. impact force and test time (or fracture deflection).

Analyzing these factors provides insight into the toughening mechanisms of nanotubes. Figure 5.21 gives the variations of the peak impact force, F_{max} , and the maximum fracture deflection, δ_{max} , with increasing temperature. It can be seen that the F_{max} is decreased almost linearly with rise in the temperature. For example, by increasing the temperature from -196 to 80 °C, the F_{max} is reduced by 58% and 40% for neat PP and 1LPP, respectively (Figure 5.21 a). For the nanocomposites, the relatively smaller reduction of F_{max} is probably due to the load-carrying ability of nanotubes. The δ_{max} , however, increases non-linearly with temperature. All materials present similar turning points at a temperature of 23 °C in δ_{max} -temperature curves (Figure 5.21 b). When the temperature changes from 23 to 80 °C, neat PP and 1LPP obtain the increases in δ_{max} by 3.1 and 10.2 times, respectively. From the above description, it becomes clear that, for the nanotube-filled composites, the resulting impact toughness lies in the combination of two factors, a relatively slightly reduced F_{max} and a much more increased δ_{max} . Obviously, the latter becomes the governing factor at higher test temperatures. Since the δ_{max} is directly related to deformation of the matrix, it can be concluded that at higher temperatures, the greater deformability of the nanotube-based composites is responsible for the major improvement in impact toughness. This conclusion is further supported by SEM observations, which are discussed below.

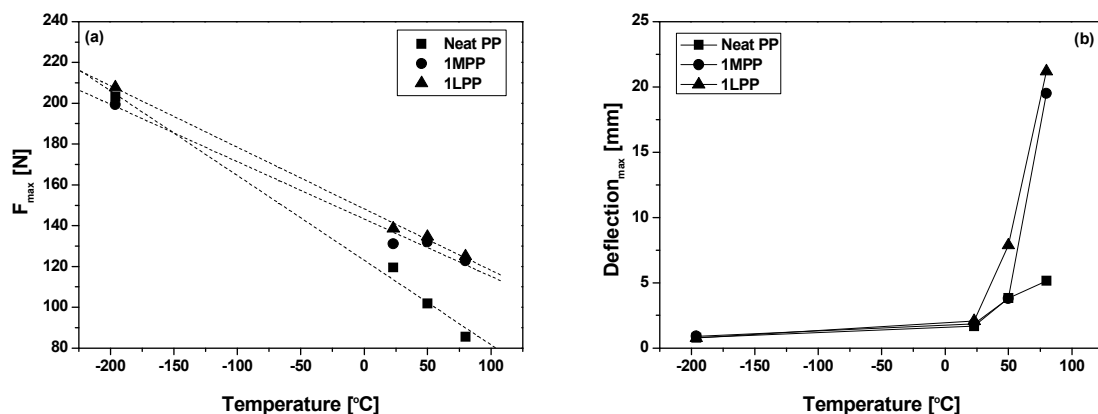
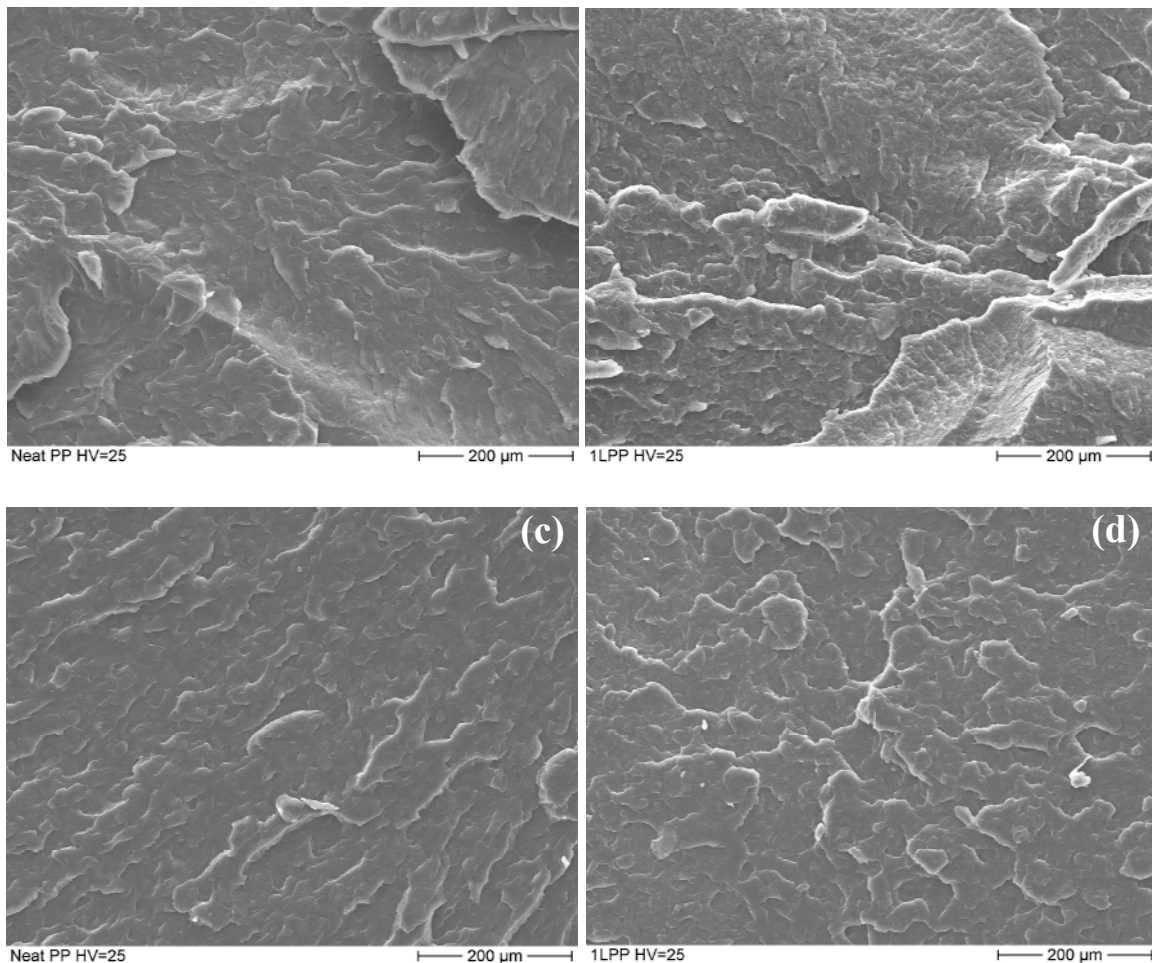


Figure 5.21: Temperature dependence of (a) maximum impact load and (b) maximum deflection of PP and its composites.

5.2.5.2 Fractography and Fracture Mechanisms

Typical SEM fracture surfaces taken from impact tests, as shown in Figure 5.22, can supply some useful information about the toughening mechanisms of nanotubes in microscale. No significant difference of fracture surfaces between neat PP and 1LPP is observed at -196 and 23 °C (Figures 5.22 a-d), while the difference becomes obvious at 80 °C (Figures 5.22 e,f). Compared to the neat PP, the 1LPP shows a relatively higher degree of plastic deformation, which is accompanied by much fracture energy dissipation. In addition, some aggregates of nanotubes can still be found in Figure 5.22 f. Evidently, it is not easy to completely break up these agglomerates by conventional mechanical mixing. It is evident that agglomerates adversely affect the impact resistance of the composites. In other words, there is great potential to enhance the polymer toughness with carbon nanotubes once a better dispersion state is achieved. An optimal compounding processing is still under investigation.



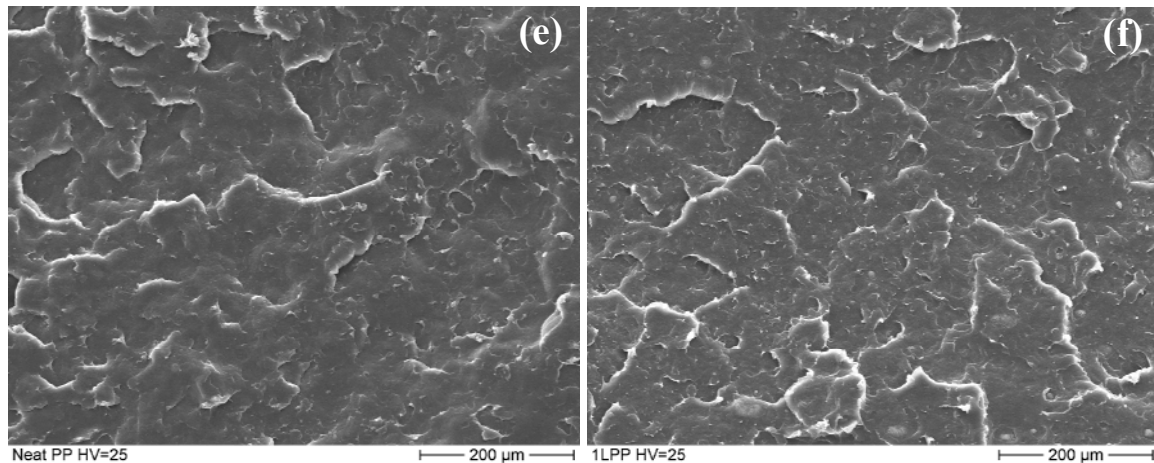


Figure 5.22: Typical lower-magnified SEM fractographs of the materials studied: (a) neat PP at $-196\text{ }^{\circ}\text{C}$, (b) 1LPP at $-196\text{ }^{\circ}\text{C}$, (c) neat PP at $23\text{ }^{\circ}\text{C}$, (d) 1LPP at $23\text{ }^{\circ}\text{C}$, (e) neat PP at $80\text{ }^{\circ}\text{C}$ and (f) 1LPP at $80\text{ }^{\circ}\text{C}$.

It is well understood [10] that in fiber-reinforced polymer composites, fibers can toughen polymer matrix through several energy-consuming events, such as fiber fracture, fiber pullout and fiber bridging. In the present work, similar features of carbon nanotubes were also observed. Figure 5.23 illustrates a high resolution SEM image of the cryogenic fractured surface of 1LPP, where nanotube bridging (A), fracture (B), and debonding/pullout (C) can be clearly recognized. Discrimination of nanotube fracture from nanotube pullout mainly relies on the length of the remaining nanotubes which protrude from the fracture surface in Figure 5.23. As is evident, a majority of the remaining nanotubes have the length of several hundred nanometers. This value seems to be close to the critical fracture length of nanotubes, ranging from several tens to several hundreds of nanometers, as reported by Wagner et al [140] in single nanotube fragmentation tests. Coleman et al [2] also found that if nanotubes were pulled out of matrices (chlorinated PP or PVA), the pullout length was roughly equal to a quarter of the total nanotube length. If a similar process occurred in our case, the length of most of the remaining nanotubes would be within a micrometer scale. Based on the above discussion, nanotube breakage is considered to be the dominant failure mode in the present systems. In addition, a rough estimation from Figure 5.23 indicates that nanotube breakage represents more than 80% of the total amount of nanotube failure.

Analogous to fiber-reinforced polymers, all these nanotube failure modes would contribute to the improvement in fracture toughness of polymer-nanotube composites [43]. However, it can be seen from Figure 5.20 that both longer and shorter nanotubes barely toughen the matrix at $-196\text{ }^{\circ}\text{C}$, despite the presence of all events A-C, whereas they significantly toughen the matrix at higher temperatures. Obviously, the toughening effect of nanotubes is temperature dependent. We may qualitatively explain this phenomenon by a balance of two competing processes: the toughening effect induced by the aforementioned energy-consuming events A-C and the embrittling effect caused by the nanotube aggregates. It is known that aggregates larger than a critical size can act as structural flaws that initiate a brittle response. At a temperature below T_g , the polymer segments are in a “frozen” state, and the polymer matrix has very limited deformability. With limited stress relaxation, the aggregates are apt to trigger brittle fracture and hence counteract the contributions of events A-C to fracture energy. On the other hand, with a rise in temperature ($T \geq T_g$), the embrittling effect of the aggregates tends to be ineffective because of the easier relaxation of polymer segments (in other words, the critical size of aggregates that trigger the brittle response becomes larger with increasing temperature). As a result of the decreased embrittling effect of aggregates, the influence of events A-C on fracture energy becomes notable. Based on this discussion, it could be inferred that appropriate matrix deformability is a precondition for the nanotube toughening effect. Such an assumption is also consistent with the results obtained by Shah et al [68]. In their case nanoclay greatly toughened semicrystalline and amorphous polymers through nanoclay orientation under applied stress field, if the polymer possessed sufficient mobility ($T > T_g$). However, if the mobility of the polymer was restricted ($T < T_g$), the nanoclay initiated crack formation and ultimately led to poor toughness.

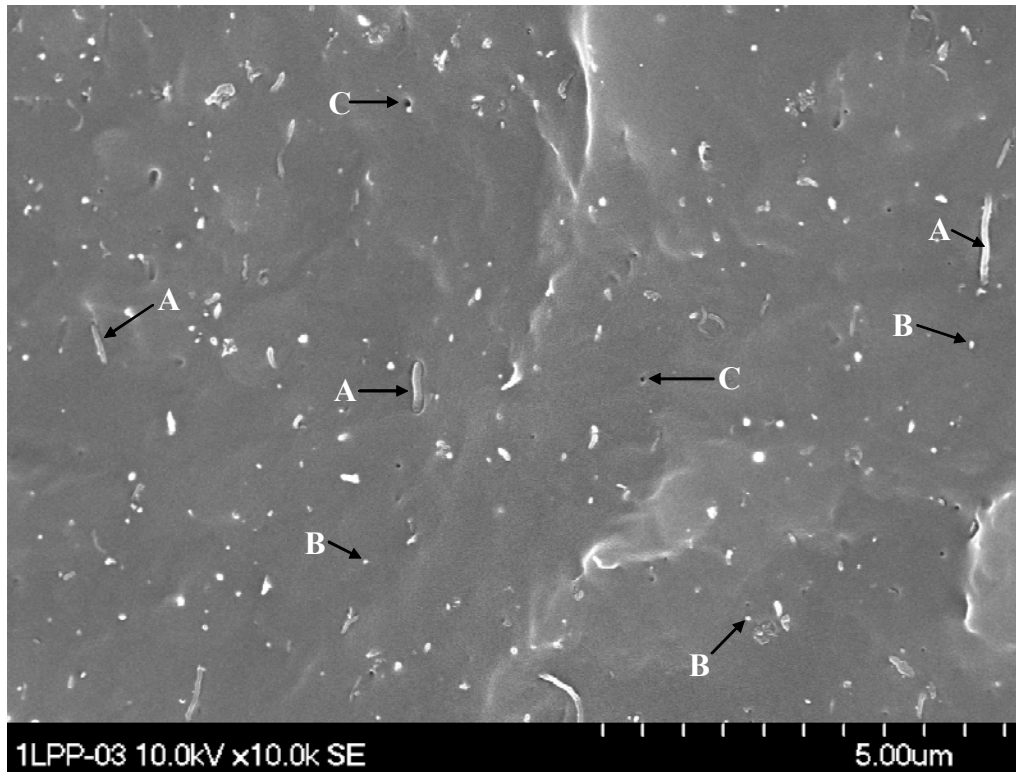


Figure 5.23: A highly magnified SEM fractograph of 1LPP.

On the other hand, the influence of spherulite size seems to be another possible toughening mechanism. It is observed from Figure 5.24 that the spherulites in the nanotube-based composites are much smaller than those in the neat PP. Larger spherulites are normally detrimental to polymer toughness. For a given crystallinity, a polymer with larger spherulites tends to be more brittle than one with a finely granular structure. This is because larger spherulites can result in a higher level of stress concentration, which induces premature fracture. Moreover, cracks propagate easily at the interfaces between larger spherulites [141,142]. Therefore, it is reasonable to consider that in the present work the tiny spherulites in the nanotube-based composites benefit the impact toughness of the PP matrix as well.

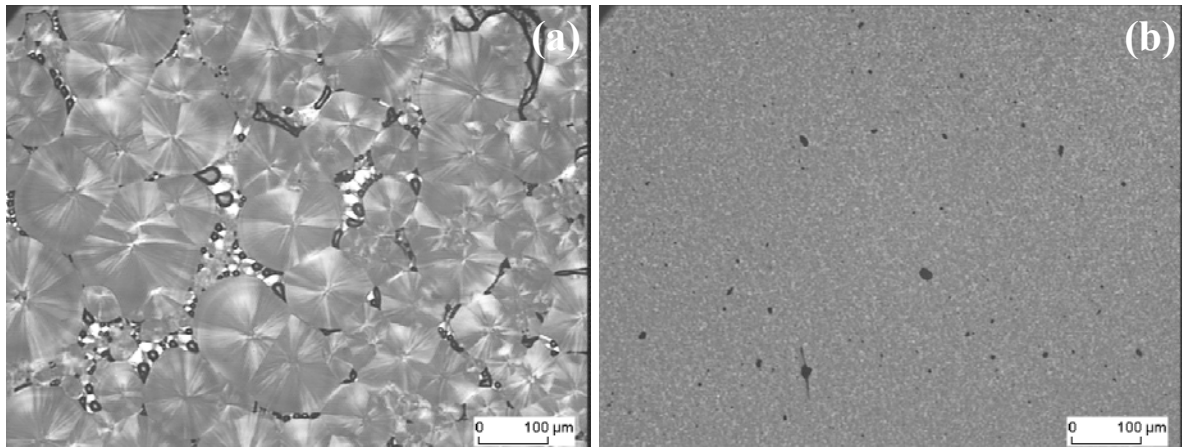


Figure 5.24: Typical polarized optical microscopy images of PP and its composites: (a) neat PP, (b) 1MPP.

6 Summary and Outlook

In the present work, various inorganic nanofillers were employed to upgrade various mechanical properties of polymer matrices. The nanofillers included SiO₂, TiO₂, Al₂O₃ and multi-walled carbon nanotubes (MWNT) of different lengths. Two types of epoxy resin (cycloaliphatic and bisphenol-F) as well as two types of thermoplastic polymer (polyamide 66 and isotactic polypropylene) served as the polymer matrices. Most attention was paid to fracture behaviors and the toughening effects of the nanofillers. Results and conclusions obtained during this work are summarized here. Finally, some suggestions for further study are also presented.

For in situ epoxy nanocomposite systems

- The *in situ* sol-gel technique was shown to be an effective method in fabrication of agglomerate-free nanocomposites with rather high filler content.
- Elastic modulus, micro-hardness and fracture toughness (characterized by K_{IC} and G_{IC}) of the nanocomposites were all enhanced with an increasing nanosilica volume content of up to c.a.14% (c.a. 23% by weight). The results confirmed that the homogeneously distributed nanoparticles were able to simultaneously improve the stiffness and toughness of epoxy matrix, which is of great importance to engineering applications. Moreover, the unnotched impact resistance of epoxy matrix was also improved at lower nanoparticle content. On the other hand, the addition of nanosilica had only slight influence on the ultimate tensile strength. In all epoxy systems used, the toughening effects of nanoparticles were more pronounced than other reinforcing effects, such as stiffening and strengthening.
- DMTA results suggested that the nanosilica particles in epoxy resins possessed considerable "effective volume fraction" in comparison with their actual volume fraction due to the presence of interphase. Moreover, AFM and high-resolution SEM observation also suggested that the nanosilica particles were coated with a polymer layer forming a core-shell structure. According to percolation theory, at the critical filler content, the interphase around nanoparticles may

interconnect and create a three-dimensional network throughout the matrix, which would dominate the performance of the nanocomposites. This could be confirmed by the relationship between interparticle distance and mechanical properties (Figures 4.10 and 4.22 a, b).

- On the basis of SEM fractograph observations, the toughening mechanisms of nanosilica-epoxy systems at plane-strain state mainly consisted of crack deflection, crack pinning/bowing and plastic deformation of the matrix.

For filled PA66 nanocomposites systems

- Addition of a very small amount of nanoparticles (1 vol.%) did not obviously alter the melting temperature, the crystallization temperature and the crystallinity of the base matrix, while it effectively increased the glass transition temperature of the matrix by about 10 °C, which suggested strong interactions between nanoparticles and the matrix.
- EWF parameters ($w_{e,ini}$ and $\beta_{ini}w_{p,ini}$) strongly depended on testing temperatures, and exhibited peak values at a certain temperature range. In general, at most testing temperatures the addition of nanoparticles resulted in positive toughening effects (i.e., increased $w_{e,ini}$) at the cost of reduction in the plastic deformation of matrix (i.e., decreased $\beta_{ini}w_{p,ini}$). The influence of the polymer relaxation around T_g s on fracture toughness should be taken into account for the materials studied.
- Based on COD analysis and SEM fractographs, two factors, crack tip blunting ($\delta_{o,ini}$) and net section stress (σ_{net}), were found to be related to the crack initiation fracture toughness ($w_{e,ini}$) of the nanocomposites. $\delta_{o,ini}$ was enhanced over most of the temperature range after the addition of various nanoparticles, probably due to the numerous dimples and sub-dimples induced by the nanoparticles, while σ_{net} depended highly on nanoparticle dispersion. Larger aggregates of nanoparticles significantly reduced the σ_{net} values (especially at room temperature); however, this trend diminished with increasing temperature.

For filled PP nanocomposites systems

- Relatively good dispersion of nanoparticles and MWNTs was achieved by using a conventional twin-screw extruder, though some smaller aggregates were still observed.
- A small amount of nanoparticles and MWNTs did not change the crystallinity and melting temperature of the PP matrix, while the MWNTs became effective nucleating agents and accelerated the crystallization process of the matrix.
- Addition of nanoparticles and MWNTs led to moderate increases in elastic modulus and tensile strength at different temperatures. The longer MWNTs exhibited the highest reinforcing effect, which was attributed to their greater aspect ratio and the corresponding higher efficiency of stress transfer from matrix to reinforcement.
- The addition of nanoparticles (especially for the surface-modified nano-TiO₂) may result in increased skin/core ratio in DDENT specimens during the injection-moulding process. Such structures can promote extreme crack blunting and subsequent necking along the tensile load direction, and thus terminate crack growth in DDENT specimens. Therefore, the EWF approach was not applicable to characterization of fracture behaviours of these nanoparticle-filled PP composites.
- The fracture toughness of MWNT-filled PP matrix over a wide range of testing temperatures was characterized by notched impact tests. The impact resistance of the PP matrix with and without nanotubes was highly temperature dependent. For all materials studied, brittle-to-ductile transitions occurred around T_g of matrix. Both shorter and longer nanotubes effectively toughened the PP matrix at a temperature above T_g , while almost no toughening effect was found at a temperatures below T_g . Two competing effects, the toughening effect of the nanotubes and the embrittling effect of aggregates, were suggested to explain this finding. Furthermore, the longer nanotubes exhibited relatively higher toughening efficiency in comparison with shorter ones over the same temperature range. On a macroscale, the enhanced toughness was ascribed to the higher load-carrying ability and larger deformability of the nanotube-based composites. Moreover, the latter factor became dominant at higher testing

temperatures. On the microscale, several failure modes of nanotubes may correspond to the consumption of fracture energy. They were bridging, debonding/pullout and breakage of nanotubes. Among these modes, nanotube breakage would be the main failure mode. In addition, the smaller size of spherulite induced by the nanotubes would also favour toughness.

Outlook

As continuation of the present work, the following issues should be taken into consideration:

- Firstly, the homogeneous dispersion of nanoparticles is still an unsolved issue. Aggregates of micron size are often found in nanocomposites when blending nanoparticles with polymers by conventional mixing machines (e.g. twin-screw extruder). This phenomenon is especially serious when attempting to prepare polymer composites with higher nanoparticle loading. Large aggregates can have a significantly adverse effect on the mechanical properties of polymers (tensile strength, impact resistance and fracture toughness). Unfortunately, so far there is no universal approach for completely breaking up the aggregates.
- Inorganic rigid particle toughening is a very complex phenomenon. Usually, several toughening mechanisms occur simultaneously in the particle-filled polymers, and each of which makes a certain contribution to the total fracture toughness of the material. For example, it was found that three toughening mechanisms (crack deflection, crack pinning/bowing and plastic deformation of matrix) seemed to be active in the epoxy-based nanocomposites. Further investigation is needed to develop a suitable model to describe the related toughening mechanisms and further predict the fracture toughness of nanocomposites at different nanoparticle loadings.
- Combination of inorganic rigid nanoparticles with other fillers (e.g., rubber particle, short fiber, thermoplastic polymer powder) in polymer matrix can dramatically enhance the fracture toughness and stiffness of the materials. This effect is generally attributed to the synergetic effects of the various components.

This phenomenon, which is interesting to both academia and industry, calls for further investigation.

8. Literature

- [1] Karger-Kocsis, J., Zhang, Z.: Structure-property relationship in nanoparticle/semicrystalline thermoplastic composites. In: Mechanical properties of polymers based on nanostructure and morphology, edited by Balta Calleja, J.F., Michler, G., CRC Press, New York, 2005, Chapter 13, pp. 547-596.
- [2] Coleman, J.N., Cadek, M., Blake, R., Nicolosi, V., Ryan, K.P., Belton, C., Fonseca, A., Nagy, J.B., Gunko, Y.K., Blau, W.J.: High-performance nanotube-reinforced plastics: understanding the mechanism of strength increase. *Advanced Functional Materials* 14 (2004) pp. 791-798.
- [3] Zhang, M.Q., Rong, M.Z., Friedrich, K.: Processing and properties of nonlayerd nanoparticle reinforced thermoplastic composites. In: Handbook of organic-inorganic hybrid materials and nanocomposites, edited by Nalwa, H.S. American Scientific Publishers, 2003, Chapter 3, pp. 141-146.
- [4] Petrovicova, E., Knight, R., Schadler, L.S., Twardowski, T.E.: Nylon 11/silica nanocomposite coatings applied by the HVOF process. II. Mechanical and barrier properties. *Journal of Applied Polymer Science* 78 (2000) pp. 2272-2289.
- [5] Zhang, M.Q., Rong, M.Z., Zheng, Y.X., Zeng, H.M. and Friedrich, K.: Improvement of tensile properties of nano-SiO₂/PP composites in relation to percolation mechanism. *Polymer* 42 (2001) pp. 3301-3304.
- [6] Kojima, Y., Usuki, A., Kawasumi, M., Okada, A., Fukushima, Y., Kurauchi, T. and Kamigaito, O.: Mechanical properties of nylon 6-clay hybrid. *Journal of Materials Research* 8 (1993) pp. 1185-1190.
- [7] Jiang, W., Liang, H.J., Jiang, B.Z.: Interparticle distance-temperature-strain rate equivalence for the brittle-tough transition in polymer blends. *Polymer* 39 (1998) pp. 4437-4442.
- [8] Chazeau, L., Gauthier, C., Vigier, G., Cavallé, J.Y.: Relationships between microstructural aspects and mechanical properties of polymer-based

- nanocomposites. In: Handbook of organic-inorganic hybrid materials and nanocomposites, edited by Nalwa, H.S. American Scientific Publishers, 2003, Chapter 2, pp. 63-111.
- [9] Garcés, M., Moll, D.J., Bicerano, J., Fibiger, R. and Mcleod, D.G.: Polymeric nanocomposites for automotive applications. *Advanced Materials* 12 (2000) pp. 1835-1839.
- [10] Thostenson, E.T., Li, C., Chou, T.W.: Nanocomposites in context. *Composites Science and Technology* 65 (2005) pp. 491-516.
- [11] Alexandre, M., Dubois, P.: Polymer-layered silicate nanocomposites: preparation, properties and use of a new class of materials. *Materials Science and Engineering* 28 (2000) pp. 1-63.
- [12] Ruan, W.H., Zhang, M.Q., Rong, M.Z.: Polypropylene composites filled with in-situ grafting polymerization modified nano-silica particles. *Journal of Materials Science* 39 (2004) pp. 3475-3478.
- [13] Wu, D.Z., Wang, X.D., Song, Y.Z., Jin, R.G.: Nanocomposites of poly(vinyl chloride) and nanometric calcium carbonate particles: Effects of chlorinated polyethylene on mechanical properties, morphology and rheology. *Journal of Applied Polymer Science* 92 (2004) pp. 2714-2723.
- [14] Xie, X.L., Liu, Q.X., Li, R.K.Y., Zhou, X.P., Zhang, Q.X., Yu, Z.Z. and Mai, Y.W.: Rheological and mechanical properties of PVC/CaCO₃ Nanocomposites prepared by in situ polymerization. *Polymer* 45 (2004) pp. 6665-6673.
- [15] Chan, C.M., Wu, J.S., Li, J.X., Cheung, Y.K.: Polypropylene/calcium carbonate nanocomposites. *Polymer* 43 (2002) pp. 2981-2992.
- [16] Evora, V.M.F., Shukla, A.: Fabrication, characterization and dynamic behavior of polyester/TiO₂ nanocomposites. *Material Science and Engineering A* 361 (2003) pp. 358-366.
- [17] Sumita, M., Tsukumo, T., Miyasaka, K., Ishikawa, K.: Tensile yield stress of polypropylene composites filled with ultrafine particles. *Journal of Materials Science* 18 (1983) pp. 1758-1764.

- [18] Sue, H.J., Gam, K.T., Bestaoui, N., Clearfield, A., Miyamoto, M., Miyatake, N.: Fracture behavior of α -zirconium phosphate-based epoxy nanocomposites. *Acta Materialia* 52 (2004) pp. 2239-2250.
- [19] Ash, B.J., Rogers, D.F., Wiegand, C.J., Schadler, L.S., Siegel, R.W., Benicewicz, B.C. and Apple, T.: Mechanical properties of Al_2O_3 /polymethylmethacrylate nanocomposites. *Polymer Composites* 23 (2002) pp. 1014-1025.
- [20] Zuiderduin, W.C.J., Westzaun, C., Huétink, J., Gaymans, R.J.: Toughening of polypropylene with calcium carbonate particles. *Polymer* 44 (2003) pp. 261-275.
- [21] Chen, L., Wang, S.C., Pisharath, S.: Fracture properties of nanoclay-filled polypropylene. *Journal of Applied Polymer Science* 88 (2003) pp. 3298-3305.
- [22] Bureau, M.N., Perrin-sarazin, F., Ton-That, M.T.: Polyolefin nanocomposites: essential work of fracture analysis. *Polymer Engineering and Science* 44 (2004) pp. 1142-1151.
- [23] Singh, R.P., Zhang, M., Chan, D.: Toughening of a brittle thermosetting polymer: effects of reinforcement particle size and volume fraction. *Journal of Materials Science* 37 (2002) pp. 781-788.
- [24] Iijima, S.: Helical microtubules of graphitic carbon. *Nature* 354 (1991) pp. 56-58.
- [25] Cooper, C.A., Ravich, D., Lips, D., Mayer, J., Wagner, H.D.: Distribution and alignment of carbon nanotubes and nanofibrils in a polymer matrix. *Composites Science and Technology* 62 (2002) pp. 1005-1112.
- [26] Treacy, M.M.J., Ebbesen, T.W., Gibson, J.M.: Exceptionally high Young's modulus observed for individual carbon nanotubes. *Nature* 381 (1996) pp. 678-680.
- [27] Lourie, O., Cox, D.M., Wagner, H.D.: Buckling and collapse of embedded carbon nanotubes. *Physics Review Letters* 81 (1998) pp. 1638-1641.

- [28] Yu, M.F., Lourie, O., Dyer, M.J., Moloni, K., Kelly, T.F., Ruoff, R.S.: Strength and breaking mechanism of multiwalled carbon nanotubes under tensile load. *Science* 287 (2000) pp. 637-640.
- [29] Liu, T.X, Phang, I.Y., Shen, L., Chow, S.Y., Zhang, W.D.: Morphology and mechanical properties of multiwalled carbon nanotubes reinforced nylon-6 composites. *Macromolecules* 37 (2004) pp. 7214-7222.
- [30] Liu, L., Wagner, H.D.: Rubbery and glassy epoxy resins reinforced with carbon nanotubes. *Composites Science and Technology* 65 (2005) pp. 1861-1868.
- [31] Lau, K. T., Hui, D.: Effectiveness of using carbon nanotubes as nano-reinforcements for advanced composite structures. *Carbon* 40 (2002) pp. 1605-1606.
- [32] Gorga, R.E., Cohen, R.E.: Toughness enhancement in poly(methyl methacrylate) by addition of oriented multiwall carbon nanotubes. *Journal of Polymer Science: Part B: Polymer Physics* 42 (2004) pp. 2690-2702.
- [33] Fidelus, J.D., Wiesel, E., Gojny, F.H., Schulte, K., Wagner, H.D.: Thermal-mechanical properties of randomly oriented carbon/epoxy nanocomposites. *Composites Part A: Applied Science and Manufacturing* 36 (2005) pp. 1555-1561.
- [34] Xu, L.R., Bhamidipati, V., Zhong, W.H., Li, J., Lukehart, C.M.: Mechanical properties characterization of a polymeric nanocomposite reinforced by graphitic nanofibers with reactive linkers. *Journal of Composite Materials* 38 (2004) pp. 1563-1582.
- [35] Fisher, F.T., Bradshaw, R.D., Brinson, L.C.: Effects of nanotube waviness on the modulus of nanotube-reinforced polymers. *Applied Physics Letters* 80 (2002) pp. 4647-4649.
- [36] Miyagawa, H., Drzal, L.T.: Thermo-physical and impact properties of epoxy nanocomposites reinforced by single-wall carbon nanotubes. *Polymer* 45 (2004) pp. 5163-5170.

- [37] Seo, M.K., Lee, J.R., Park S. J.: Crystallization kinetics and interfacial behaviors of polypropylene composites reinforced with multi-walled carbon nanotubes. *Material Science and Engineering A* 404 (2005) pp. 79-84.
- [38] Satapathy, B.K., Weidisch, R., Pötschke, P., Janke, A.: Crack toughness behavior of multiwalled carbon nanotube (MWNT)/polycarbonate nanocomposites. *Macromolecular Rapid Communications* 26 (2005) pp. 1246-1252.
- [39] Meincke, O., Kaempfer, D., Weickmann, H., Friedrich, C., Vathauer, M., Warth, H.: Mechanical properties and electrical conductivity of carbon-nanotube filled polyamide-6 and its blends with acrylonitrile/butadiene/styrene. *Polymer* 45 (2004) pp. 739-748.
- [40] Velasco-Santos, C., Martinez-Hernandez, A.L., Fisher, F.T., Ruoff, R., and Castano, V.M.: Improvement of thermal and mechanical properties of carbon nanotube composites through chemical functionalization. *Chemistry of Materials* 15 (2003) pp. 4470-4475.
- [41] Miyagawa, H., Drzal, L.T.: Thermo-physical and impact properties of epoxy nanocomposites reinforced by single-wall carbon nanotubes. *Polymer* 45 (2004) pp. 5163-5170.
- [42] Satapathy, B.K., Weidisch, R., Pötschke, P., Janke, A.: Crack toughness behavior of multiwalled carbon nanotube (MWNT)/polycarbonate nanocomposites. *Macromolecular Rapid Communications* 26 (2005) pp. 1246-1252.
- [43] Ajayan, P.M., Schadler, L.S., Giannaris, C., Rubio, A.: Single-walled carbon nanotube-polymer composites: strength and weakness. *Advanced Materials* 12 (2000) pp.750-753.
- [44] Qian, D., Dickey, E.C., Andrews, R., Rantell, T.: Load transfer and deformation mechanisms in carbon nanotube-polystyrene composites. *Applied Physics Letters* 76 (2000) pp. 2868-2870.
- [45] Suhr, J., Koratkar, N., Kerlinski, P., Ajayan, P.: Viscoelasticity in carbon nanotube composites. *Nature Materials* 4 (2005) pp. 134-137.

- [46] Chen, W., Tao, X.M., Xue, P., Cheng, X.Y.: Enhancement mechanical properties and morphological characterizations of poly(vinyl alcohol)-carbon nanotube composite films. *Applied Surface Science* 252 (2005) pp. 1404-1409.
- [47] Koratkar, N., Wei, B., Ajayan, P.M.: Carbon nanotube films for damping applications. *Advanced Materials* 14 (2002) pp. 997-1000.
- [48] Thostenson, E.T., Chou, T.W.: Aligned multi-walled carbon nanotube-reinforced composites: processing and mechanical characterization. *Journal of Physics D: Applied Physics* 35 (2002) pp. 77-80.
- [49] Haggemueller, R., Gommans, H.H., Rinzler, A.G., Fischer, J.E., Winey, K.I.: Aligned single-wall carbon nanotubes in composites by melt processing methods. *Chemical Physics Letters* 330 (2000) pp. 219-225.
- [50] Musto, P., Ragosta, G., Scarinzi, G., Mascia, L.: Toughness enhancement of polyimides by in situ generation of silica particles. *Polymer* 45 (2004) pp. 4265-4274.
- [51] Chen, Y.C., Zhou, S.X., Gu, G.X., Wu, L.M.: Microstructure and properties of polyester-based polyurethane/titania hybrid films prepared by sol-gel process. *Polymer* 47 (2006) pp. 1640-1648.
- [52] Dewimille, L., Bresson, B., Bokobza, L.: Synthesis, structure and morphology of poly(dimethylsiloxane) networks filled with in situ generated silica particles. *Polymer* 46 (2005) pp. 4135-4143.
- [53] Sreekala, M.S., Eger, C.: Property improvement of an epoxy resin by nanosilica particle reinforcement. In: *Polymer composites - from nano- to macro- scale*, edited by Friedrich K, Fakirov S, Zhang Z, Springer, 2005, Chapter 6, pp. 91-105.
- [54] Matejka, L., Dukh, O., Kolarik, J.: Reinforcement of crosslinked rubbery epoxies by in-situ formed silica. *Polymer* 41 (2000) pp. 1449-1459.
- [55] Andrews, R., Jacques, D., Minot, M., Rantell, T.: Fabrication of carbon multiwall nanotube/polymer composites by shear mixing. *Macromolecular Materials and Engineering* 287 (2002) pp. 395-403.

- [56] Cho, J.W., Paul, D.R.: Nylon 6 nanocomposites by melt compounding. *Polymer* 42 (2001) pp. 1083-1094.
- [57] Gatos, K.G.: Structure-property relationships in rubber/layered silicate nanocomposites. PhD Thesis (2005) pp. 19-25.
- [58] Rong, M.Z., Zhang, M.Q., Zheng, Y.X., Zeng, H.M., Walter, R., Friedrich, K.: Structure-property relationships of irradiation grafted nano-inorganic particle filled polypropylene composites. *Polymer* 42 (2001) pp. 167-183.
- [59] Rong, M.Z., Zhang, M.Q., Zheng, Y.X., Zeng, H.M., Friedrich, K.: Improvement of tensile properties of nano-SiO₂/PP composites in relation to percolation mechanism. *Polymer* 42 (2001) pp. 3301-3304.
- [60] Wang Z, Liang ZY, Wang B, Zhang C, Kramer L. Processing and property investigation of single-walled carbon nanotube (SWNT) buckypaper/epoxy resin matrix nanocomposites. *Composites: Part A* 35 (2004) pp.1225-1232.
- [61] Coleman J.N., Blau, W.J., Dalton, A.B., Munoz, E., Collins, S., Kim, B.G., Razal, J., Selvidge, M., Vieiro, G., Baughman, R.H.: Improving the mechanical properties of single-walled carbon nanotube sheets by intercalation of polymeric adhesives. *Applied Physics Letters* 82 (2003) pp.1682-1684.
- [62] Bartczak, Z., Argon, A.S., Cohen, R.E., Weinberg, M.: Toughness mechanism in semi-crystalline polymer blends: II. High-density polyethylene toughened with calcium carbonate filler particles. *Polymer* 40 (1999) pp. 2347-2365.
- [63] Wilbrink, M.W.L., Argon, A.S., Cohen, R.E., Weinberg, M.: Toughenability of nylon-6 with CaCO₃ filler particles: new findings and general principles. *Polymer* 42 (2001) pp. 10155-10180.
- [64] Thio, Y.S., Argon, A.S., Cohen, R.E., Weinberg, M.: Toughening of isotactic polypropylene with CaCO₃ particles. *Polymer* 43 (2002) pp. 3661-3674.
- [65] Friedrich, K., Karsch U.A.: Failure processes in particulate filled polypropylene. *Journal of Materials Science* 16 (1981) pp. 2167-2175.
- [66] Thio, Y.S., Argon, A.S., Cohen, R.E.: Role of interracial adhesion strength on toughening polypropylene with rigid particles. *Polymer* 45 (2004) pp. 3139-3147.

- [67] Lazzeri, A., Zabarjad, S.M., Pracella, M., Cavalier, K., Rosa, R.: Filler toughening of plastics. Part 1—The effect of surface interactions on physico-mechanical properties and rheological behavior of ultrafine CaCO₃/HDPE nanocomposites. *Polymer* 46 (2005) pp. 827-844.
- [68] Shah, D., Maiti, P., Jiang, D.D., Batt, C.A., Giannelis, E.P.: Effect of nanoparticle mobility on toughness of polymer nanocomposites. *Advanced Materials* 17 (2005) pp. 525-528.
- [69] Farber, K.T., Evans, A.G.: Crack deflection process-I Theory. *Acta Metallurgica* 31 (1983) pp. 565-576.
- [70] Farber, K.T., Evans, A.G.: Crack deflection process-II Experiment. *Acta Metallurgica* 31 (1983) pp. 577-584.
- [71] Lange, F.F.: The interaction of a crack front with a second-phase dispersion. *Philosophy Magazine* 22 (1970) pp. 983-992.
- [72] Green, D.J., Nicholson, P.S., Embury, J.D.: Fracture of a brittle particulate composite: Part 2 Theoretical aspects. *Journal of Materials Science* 14 (1979) pp. 1657-1661.
- [73] Moloney, A.C., Kausch, H.H., Stieger, H.R.: The fracture of particulate-filled epoxide resins. *Journal of Materials Science* 18 (1983) pp. 208-216.
- [74] Spanoudakis, J., Young, R.J.: Crack propagation in a glass particle-filled epoxy resin. *Journal of Materials Science* 19 (1984) pp. 487-496.
- [75] Cardwell, B.J., Yee, A.F.: Toughening of epoxies through thermoplastic crack bridging. *Journal of Materials Science* 33 (1998) pp. 5473-5484.
- [76] Azimi, H.R., Pearson, R.A., Hertzberg, R.W.: Fatigue of hybrid epoxy composites: epoxies containing rubber and hollow glass spheres. *Polymer Engineering and Science* 36 (1996) pp. 2352-2365.
- [77] Wang, K., Chen, L., Wu, J.S., Toh, M.L., He., C. and Yee, A.F.: Epoxy nanocomposites with highly exfoliated clay: Mechanical properties and fracture mechanisms. *Macromolecules* 38 (2005) pp. 788-800.
- [78] Williams, J.G.: Chapter 1 - K_c and G_c at slow speeds for polymers. *Fracture mechanics testing methods for polymer, adhesives and composites*,ESIS 28,

- edited by D.R. Moore, A. Pavan and J.G. Williams, Elsevier Sci. 2001, pp. 14-25.
- [79] Broberg, K.B.: Critical review of some theories in fracture mechanics. *International Journal of Fracture Mechanics* 4 (1968) pp. 11-18.
- [80] Broberg, K.B.: Discussion of initial and subsequent crack growth. *Engineering Fracture Mechanics* 5 (1973) pp. 1031-1035.
- [81] Broberg, K.B.: On stable crack growth. *Journal of Physics and Mechanics of Solids* 23 (1975) pp. 215-237.
- [82] Wu, J.S., Mai, Y.W.: The essential fracture work concept for toughness measurement of ductile polymers. *Polymer Engineering and Science* 36 (1996) pp. 2275-2288.
- [83] Hashemi, S.: Work of fracture of PBT/PC blend: effect of sample size, geometry and rate of testing. *Polymer Engineering and Science* 37 (1997) pp. 912-921.
- [84] Karger-Kocsis, J., Czigany, T., Moskala, E.J.: Thickness dependence of work of fracture parameters of an amorphous copolyester. *Polymer* 38 (1997) pp. 4587-4593.
- [85] Arkhirezeva, A., Hashemi, S., O'Brien, M.: Factors affecting work of fracture of uPVC film. *Journal of Material Science* 34 (1999) pp. 5961-5974.
- [86] Hashemi, S.: Determination of the fracture toughness of polybutylene terephthalate (PBT) film by the essential work method: effect of sample size and geometry. *Polymer Engineering and Science* 40 (2000) pp. 798-808.
- [87] Low, I.T.M. Mai, Y.W.: Rate and Temperature effects on crack blunting mechanisms in pure and modified epoxies. *Journal of Material Science* 24 (1989) pp. 1634-1644.
- [88] Karger-Kocsis, J., Czigany, T., Moskala, E.J.: Deformation rate dependence of the essential and non-essential work of fracture parameters in an amorphous copolyester. *Polymer* 39 (1998) pp. 3939-3944.

- [89] Hashemi, S., Williams, J.G.: Temperature dependence of essential and non-essential work of fracture parameters for polycarbonate film. *Plastics, Rubber and Composites* 29 (2000) pp. 294-302.
- [90] Arkhireyeva, A., Hashemi, S.: Combined effect of temperature and thickness on work of fracture parameters of unplasticized PVC film. *Polymer Engineering and Science* 42 (2002) pp. 504-518.
- [91] Arkhireyeva, A., Hashemi, S.: Effect of temperature on work of fracture parameters in poly(ether-ether ketone) (PEEK) film. *Engineering Fracture Mechanics* 71 (2004) pp. 789-804.
- [92] Poon, W.K.Y., Ching, E.C.Y., Cheng, C.Y., Li, R.K.Y.: Measurement of plane stress essential work of fracture (EWF) for polymer films: effects of gripping and notching methodology. *Polymer Testing* 20 (2001) pp. 395-401.
- [93] Yamakawa, R.S., Razzino, C.A., Correa, C.A., E.Hage Jr.: Influence of notching and molding conditions on determination of EWF parameters in polyamide 6. *Polymer Testing* 23 (2004) pp. 195-202.
- [94] Wu, J.S., Mai, Y.W., Cotterell, B.: Fracture toughness and fracture mechanisms of PBT/PC/IM blend: part I fracture properties. *Journal of Material Science* 28 (1993) pp. 3373-3384.
- [95] Maspoch, M.LI., Gámez-Pérez, J., Gordillo, A., Sánchez-Soto, M., Velasco, J.I.: Characterisation of injected EPBC plaques using the essential work of fracture (EWF) method. *Polymer* 43 (2002) pp. 4177-4183.
- [96] Tjong, S.C., Xu, S.A., Li, R.K.Y., Mai, Y.W.: Short glass fiber-reinforced polyamide 6,6 composites toughened with maleated SEBS. *Composites Science and Technology* 62 (2002) pp. 2017-2027.
- [97] Wong, S.C., Mai, Y.W.: Essential fracture work of short fiber reinforced polymer blends. *Polymer Engineering and Science* 39 (1999) pp. 356-364.
- [98] Sui, G.X., Wong, S.C., Yue, C.Y.: The effect of fiber inclusions in toughened plastics-part I: fracture characterization by essential fracture work. *Composites Science and Technology* 61 (2001) pp. 2481-2490.

- [99] Ching, E.C.Y., Poon, W.K.Y., Li, R.K.Y., Mai, Y.W.: Effect of strain rate on the fracture toughness of some ductile polymers using the essential work of fracture (EWF) approach. *Polymer Engineering and Science* 40 (2000) pp. 2558-2568.
- [100] Luna, P., Bernal, C., Cisilino, A., Frontini, P., Cotterell, B., Mai, Y.W.: The application of the essential work of fracture methodology to the plane strain fracture of ABS 3-point blend samples. *Polymer* 44 (2003) pp. 1145-1150.
- [101] Karger-Kocsis, J., Barany, T., Moskala, E.J.: Plane stress fracture toughness of physically aged plasticized PETG as assessed by the essential work of fracture (EWF) method. *Polymer* 44 (2003) pp. 5691-5699.
- [102] Karger-Kocsis, J., Moskala, E.J.: Molecular dependence of the essential and non-essential work of fracture of amorphous films of poly(ethylene-2,6-naphthalate) (PEN). *Polymer* 41 (2000) pp. 6301-6310.
- [103] Qiao, Y., Avlar, S., Chakravarthula, S.S.: Essential fracture work of nylon 6-silicate nanocomposites. *Journal of Applied Polymer Science* 95 (2005) pp. 815-819.
- [104] Clutton, E.: Fracture mechanics testing methods for polymer, adhesives and composites, ESIS 28, edited by D.R. Moore, A. Pavan and J.G. Williams, Elsevier Sci. 2001, pp.177-195.
- [105] Mouzakis, D.E., Karger-Kocsis, J.: Interrelation between energy partitioned work of fracture parameters and the crack tip opening displacement in amorphous polyester films. *Journal of Material Science Letters* 19 (2000) pp. 1615-1619.
- [106] Krumova, M., Klingshirm, C., Hauptert, F., Friedrich, K.: Microhardness studies on functionally graded polymer composites. *Composites Science and Technology* 61 (2001) pp. 557-563.
- [107] Dasari, A. Yu, Z.Z., Yang, M.S., Zhang, Q.X., Xie, X.L, Mai, Y.W.: Micro- and nano-scale deformation behaviour of nylon 66-based binary and ternary nanocomposites. *Composites Science and Technology* 66 (2006) pp. 3097-3114.

- [108] Norman, D.A., Robertson, R.E.: Rigid-particle toughening of glassy polymers. *Polymer* 44 (2003) pp. 2351-2362.
- [109] Matějka, L., Dukh, O., Kolařík, J.: Reinforcement of crosslinked rubbery epoxies by in-situ formed silica. *Polymer* 41 (2000) pp. 1449-1459.
- [110] Bagheri, R., Pearson, R.A.: Role of particle cavitation in rubber-toughened epoxies: 1. Microvoid toughening. *Polymer* 37 (1996) pp. 4529-4538.
- [111] Nichols, M.E., Robertson, R.E.: The toughness of epoxy-poly(butylene terephthalate) blends. *Journal of Materials Science* 29 (1994) pp. 5916-5926.
- [112] Hodgkin, J.H., Simon, G.P., Varley, R.J.: Thermoplastic toughening of epoxy resins: a critical review. *Polymer for Advanced Technologies* 9 (1998) pp. 3-10.
- [113] Abramoff, B., Convino, J.: Transmittance and mechanical properties of PMMA-fumed silica composites. *Journal of Applied Polymer Science* 46 (1992) pp. 1785-1791.
- [114] Landry, C.J. T., Coltrain, B.K., Landry, M.R.: Poly(vinyl acetate)/silica filled materials: material properties of in situ vs. fumed silica particles. *Macromolecules* 26 (1993) pp. 3702-3712.
- [115] Liu, Y.L., Hsu, C.Y., Wei, W.L., Jeng, R.J.: Preparation and thermal properties of epoxy-silica nanocomposites from nanoscale colloidal silica. *Polymer* 44 (2003) pp. 5159-5167.
- [116] <http://www accuratus.com/fused.html> (December 2005).
- [117] Ziegel, K.D., Romanow, A.: Modulus reinforcement in elastomer composites. I. Inorganic fillers. *Journal of Applied Polymer Science* 17 (1973) pp. 1119-1131.
- [118] Iisaka, K., Shibayama, K.: Mechanical α -dispersion and interaction in filled polystyrene and polymethylmethacrylate. *Journal of Applied Polymer Science* 22 (1978) pp. 3135-3143.
- [119] Sumita, M., Tsukihi, H., Miyasaka, K., Ishikawa, K.: Dynamic mechanical properties of polypropylene composites filled with ultrafine particles. *Journal of Applied Polymer Science* 29 (1984) pp. 1523-1530.

- [120] Lee, J., Yee, A.F.: Inorganic particle toughening I: micro-mechanical deformations in the fracture of glass bead filled epoxies. *Polymer* 42 (2001) pp. 577-588.
- [121] Odegard, G.M., Clancy, T.C., Gates, T.S.: Modelling of the mechanical properties of nanoparticle/polymer composites. *Polymer* 46 (2005) pp. 553-562.
- [122] Sánchez-Soto, M., Gordillo, A., MasPOCH, M.L.: Glass bead filled polystyrene composites: morphology and fracture. *Polymer Bulletin* 47 (2002) pp. 587-594.
- [123] Ragosta, G., Abbate, M., Musto, P., Scarinzi, G., Mascia, L.: Epoxy-silica particulate nanocomposites: Chemical interactions, reinforcement and fracture toughness. *Polymer* 46 (2005) pp. 10506-10516.
- [124] Becker, O., Varley, R., Simon, G.: Morphology, thermal relaxations and mechanical properties of layered silicate nanocomposites based upon high-functionality epoxy resins. *Polymer* 43 (2002) pp. 4365-4373.
- [125] Vassileva, E., Friedrich, K.: Epoxy/alumina nanoparticle composites. I. Dynamic mechanical behavior. *Journal of Applied Polymer Science* 89 (2003) pp. 3774-3785.
- [126] Perkins, W.G.: Polymer toughness and impact resistance. *Polymer Engineering and Science* 39 (1999) pp. 2445-2460.
- [127] Ou, Y.C., Yang, F., Yu, Z.Z.: A new conception on the toughness of nylon 6/silica nanocomposite prepared via in situ polymerisation. *Journal of Polymer Science: Part B* 36 (1998) pp. 789-795.
- [128] Yamini, S., Young, R.J.: Stability of crack propagation in epoxy resins. *Polymer* 18 (1977) pp. 1075-1080.
- [129] Spanoudakis, J., Young, R.J.: Crack propagation in a glass particle-filled epoxy resin. Part 1: Effect of particle volume fraction and size. *Journal of Materials Science* 19 (1984) pp. 473-486.
- [130] Ye, L., Yuan, C.T., Mai, Y.W.: Effects of rate and temperature on fracture behavior of TPX (poly-4-methyl-1-pentene) polymer. *Polymer Composites* 19 (1998) pp. 830-836.

- [131] Karger-Kocsis, J.: Stick-slip crack growth during instrumented high-speed impact of HDPE and HDPE/SELAR[®] discontinuous laminar microlayer composites. *Journal of Macromolecular Science-Physics B40* (3&4) (2001) pp. 343-353.
- [132] Kinloch, A.J., Williams, J.G.: Crack blunting mechanisms in polymers. *Journal of Materials Science* 15 (1980) pp. 987-996.
- [133] Mckilliam, G., Moltschaniwskyj, G., Horrigan, D.P.W.: Viscoelastic phenomena in the fracture of thermosetting resins. *Journal of Materials Science* 33 (1998) pp. 103-108.
- [134] Gryshchuk, O., Jost, N., Karger-Kocsis, J.: Toughening of vinyl-urethane hybrid resins through functionalized polymers. *Journal of Applied Polymer Science* 84 (2002) pp. 672-680.
- [135] Cantwell, W.J., Smith, J.W., Kausch, H.H.: Examination of the processes of deformation and fracture in a silica-filled epoxy resin. *Journal of Materials Science* 25 (1990) pp. 633-648.
- [136] Covavisaruch, J.S., Robertson, R.E., Filisko, F.E.: Basic longitudinal texture and fracturing process in thermoset polymers. *Journal of Materials Science* 27 (1992) pp. 990-1000.
- [137] Kohan, M.I., Hewel, M., Torre, D.: *Nylon plastics handbook*, edited by Kohan, M.I., Hanser/Gardner Publication, Inc., Cincinnati. 1995, pp. 414-434.
- [138] Kim, P., Schuh, T., Wittig, W.: CFRP-from motor sports into automotive series: challenges and opportunities facing the technology transfer. *Plastic in Automotive Engineering* (2004) pp. 45-49.
- [139] Yang, J.L., Zhang, Z., Zhang, H.: The essential work of fracture of polyamide 66 filled with TiO₂ nanoparticles. *Composites Science and Technology* 65 (2005) pp. 2374-2379.
- [140] Wagner, H.D., Lourie, O., Feldman, Y., Tenne, R.: Stress-induced fragmentation of multiwall carbon nanotubes in a polymer matrix. *Applied Physics Letters* 72 (1998) pp. 188-190.

- [141] Friedrich, K.: Analysis of crack propagation in isotactic polypropylene with different morphology. *Progress in Colloid and Polymer Science* 64 (1978) pp. 103-112.
- [142] Friedrich, K.: Strength and fracture of crystalline isotactic polypropylene and the effect of molecular and morphological parameters. *Progress in Colloid and Polymer Science* 66 (1979) pp. 299-309.

8 List of Publications

Refereed journal papers

1. Zhang, H., Zhang, Z., and Breidt, C.: Comparison of short carbon fiber surface treatment on epoxy composites: I. Enhancement of the mechanical properties, *Composites Science and Technology* 64 (2004) pp. 2021-2029.
2. Zhang, H., Zhang, Z.: Comparison of short carbon fiber surface treatment on epoxy composites: II. Enhancement of the wear resistance, *Composites Science and Technology* 64 (2004) pp. 2031-2038
3. Yang, J-L., Zhang, Z., Zhang, H.: The essential work of fracture of polyamide 66 filled with TiO₂ nanoparticles, *Composite Science and Technology* 65 (2005), pp. 2374-2379.
4. Chang, L., Zhang, Z., Zhang, H. and Schlarb, A.K.: On the sliding wear of nanoparticles filled polyamide 6,6, *Composites Science and Technology* 66 (2006), pp. 3188-3198.
5. Chang, L., Zhang, Z., Zhang, H. and Friedrich, K.: Effect of nanoparticles on the tribological behaviour of short carbon fibre reinforced poly(etherimide) composites, *Tribology International* 38 (2005), pp. 966-973.
6. Zhang, H., Zhang, Z., Yang, J-L., Friedrich, K.: Temperature dependence of crack initiation fracture toughness of various nanoparticles filled polyamide 66, *Polymer* 47 (2006), pp. 679-689.
7. Zhang, H., Zhang, Z., Friedrich, K.: Properties improvements of *in situ* epoxy nanocomposites with reduced interparticle distance at high nanosilica content, *Acta Materialia* 54 (2006) pp. 1833-1842.
8. Song, L., Zhang, H., Zhang, Z. and Xie, S.S.: Processing and mechanical performance of SWNT paper reinforced PEEK nanocomposites, *Composites Part A* 38 (2007) pp. 388-392.

9. Zhang, H., Zhang, Z., Friedrich, K.: Effect of fibre length on the wear resistance of short carbon fibre reinforced epoxy composites, *Composites Science and Technology* 67 (2007) pp. 222-230.

Conference/symposium proceedings

10. Chang, L., Zhang, Z., Zhang, H.: Enhancement of the tribological properties of fibre-reinforced polyamide 66 by TiO₂ nanoparticles, *IVW-Kolloquium 2004*, IVW-Schriftenreihe Band 48, 5.-6. Oktober 2004, pp. 183-188.
11. Zhang, H., Zhang, Z.: Mechanical and tribological properties of treated short carbon fiber/epoxy composites, *IVW-Kolloquium 2004*, IVW-Schriftenreihe Band 48, 5.-6. Oktober 2004, pp. 189-195.
12. Chang, L., Zhang, Z., Zhang, H.: Tribological properties of TiO₂ particle filled polyetherimide composites, *Europe/China Symposium on Reinforced Polymers*, June 29-July 2, 2004, the Ecole des Mines in Nancy, France, CD-ROM.
13. Zhang, H., Zhang, Z.: Influence of fiber length on the sliding performance of short carbon fiber reinforced epoxy, *Europe/China Symposium on Reinforced Polymers*, June 29-July 2, 2004, the Ecole des Mines in Nancy, France, CD-ROM.
14. Yang, J-L., Zhang, Z., Zhang, H.: The fracture work of polyamide 6,6 filled with TiO₂ nanoparticles, *Europe/China Symposium on Reinforced Polymers*, June 29-July 2, 2004, the Ecole des Mines in Nancy, France, CD-ROM.
15. Chang, L., Zhang, Z., Zhang, H.: The enhancement of the tribological properties of fibre-reinforced polyamide 6,6 by TiO₂ nanoparticles, *11th European Conference on Composite Materials (ECCM 11)*, May 31- June 3, 2004, Rhodes, Greece, CD-ROM.
16. Yang, J-L., Zhang, Z., Zhang, H.: The work-of-fracture of TiO₂ nanoparticle filled polyamide 6,6: *International Symposium on Engineering Plastics (EP'2004)*, Lanzhou, China, August 15-20, 2004

17. Yang, J-L., Zhang, Z., Zhang, H., Friedrich, K.: Fatigue crack propagation of inorganic nanoparticle filled polyamide 6,6, 11th International Conference on Fracture, Turin, Italy, March 20-25, 2005.
18. Chang, L., Zhang, Z., Zhang, H.: Enhancement of nano-TiO₂ particle filled high temperature resistant polymers, 2005 China International Conference on Nanoscience and Technology (ChinaNano2005), June 9 - 11, 2005 Beijing, China.
19. Zhang, H., Zhang, Z., Friedrich, K.: Mechanical and thermal properties of *in situ* SiO₂/epoxy nanocomposites, 2005 China International Conference on Nanoscience and Technology (ChinaNano2005), June 9 - 11, 2005 Beijing, China.